Title
Sterile Neutrinos and Primordial Black Holes as Dark Matter Candidates

Author
Lu, Philip

Publication Date
2021

Peer reviewed|Thesis/dissertation

UNIVERSITY OF CALIFORNIA

Los Angeles

Sterile Neutrinos and Primordial Black Holes as Dark Matter Candidates

A dissertation submitted in partial satisfaction

of the requirements for the degree

Doctor of Philosophy in Department of Physics and Astronomy

by

Philip Lu

2021

ABSTRACT OF THE DISSERTATION

Sterile Neutrinos and Primordial Black Holes as Dark Matter Candidates

by

Philip Lu
University of California, Los Angeles, 2021
Professor Graciela Gelmini, Chair

We focus on two dark matter candidates: sterile neutrinos and primordial black holes (PBH). We explore the effects of non-standard pre-Big Bang Nucleosynthesis (pre-BBN) cosmologies, such scalar-tensor and kination cosmologies, on the abundance of sterile neutrinos over a large range of masses. In particular, sterile neutrinos of keV-scale mass represent a viable warm dark matter candidate whose decay can generate the putative 3.5 keV X-ray signal observed in galaxy and galaxy clusters. eV-scale sterile neutrinos can be the source of various accelerator/beam neutrino oscillation anomalies. Two production mechanisms are considered here, a collisional non-resonant Dodelson-Widrow (DW) mechanism and a resonant Shi-Fuller (SF) conversion (which requires a large lepton asymmetry). The DW mechanism is a freeze-in process, and the final abundance of sterile neutrinos using this production method is inversely proportional to the Hubble expansion rate. We find that in one of the scalar tensor models we consider, the sterile neutrino parameters necessary to generate the tentative 3.5 keV signal would be within reach of the TRISTAN upgrade to the ongoing KATRIN experiment as well as the planned upgrades to the HUNTER experiment, however the contribution to the dark matter density would be very small. In another scalar tensor model, sterile neutrinos could both generate the X-ray signal and comprise much of dark matter. In our study of resonant production, we find that the parameter space in which coherent and adiabatic resonant production can occur shifts with changing pre-BBN cosmology. We find that for a broad range of parameters (mass, mixing angle, lepton asymmetry), resonance can occur in the LSND/MiniBooNE and DANS/NEOSS experiments' preferred regions for at least one of the non-standard cosmologies we consider. With respect to PBH as dark matter candidates, we derive a new type of cosmology-independent bound. We consider the heating of the surrounding interstellar medium gas by dynamical friction and from the formation of accretion disks around intermediate mass $10 - 10^5 M_\odot$ PBH. By estimating the cooling rate and assuming thermal equilibrium, we derive a new constraint. Light PBH with mass $10^{15} - 10^{17}$ g emit significant Hawking radiation and are constrained by the same cooling argument. We extend this analysis to PBH with extreme spin, which results in stronger bounds compared to non-spinning PBH.

The dissertation of Philip Lu is approved.

Matthew Malkan

Terry Tomboulis

Alexander Kusenko

Graciela Gelmini, Committee Chair

University of California, Los Angeles

2021

For my parents, Wei and Sappho

TABLE OF CONTENTS

LIST OF FIGURES

LIST OF TABLES

ACKNOWLEDGMENTS

I would like to thank my advisor, Graciela Gelmini, for guiding me through my PhD and for putting up with my attitude, and for taking me on after a rough three years. I am grateful for all the work Volodymyr Takhistov put in to make sure these projects progressed and got published, for his advice and ideas, and for the help and encouragement throughout the postdoctoral application process. Alexander Kusenko has been generally helpful throughout my PhD, and I appreciate his collaboration, letter of recommendation, and suggestions. I am also beholden to Yoshiyuki Inoue for being my recommender and collaborator. Thanks to the rest of my committee, Roberto Peccei, Terry Tomboulis, and Matthew Malkan for devoting their time to my candidacy exam and thesis defense. I am indebted to Michael Bloxham for not failing me in freshman physics and giving me a second chance. I wish to thank my roommate Warren Nadvornick who taught me the lessons he learned from his own painstaking thesis process. Lastly, the staff of the Physics and Astronomy department, especially Stephanie Krilov and Frank Nevarez, have been very efficient and supportive throughout my time here.

VITA

2015	B.S. Physics and Applied Mathematics, University of California, Berkeley.
2016	M.S. Physics, University of California, Los Angeles.

PUBLICATIONS

6. *Gas Heating from Spinning and Non-Spinning Primordial Black Holes*, R. Laha, P. Lu, V. Takhistov, arXiv:2009.11837. Submitted to Phys. B Letters.

5. *Constraining Primodial Black Holes with Dwarf Galaxy Heating*, P. Lu, V. Takhistov, G. Gelmini, K. Hayashi, Y. Inoue, A. Kusenko, arXiv:2007.02213. Submitted to ApJ Letters.

4. *Note on Thermalization of Non-resonantly Produced Sterile Neutrinos*, G. Gelmini, P. Lu, V. Takhistov, JCAP **10** (2020) A01, arXiv:2006.09553.

3. *Cosmological Dependence of Resonantly Produced Sterile Neutrinos*, G. Gelmini, P. Lu, V. Takhistov, JCAP **06** (2020) 008, arXiv:1911.03398.

2. *Cosmological Dependence of Non-resonantly Produced Sterile Neutrinos*, G. Gelmini, P. Lu, V. Takhistov, JCAP **12** (2019) 047, arXiv:1909.13328.

1. *Visible Sterile Neutrinos as the Earliest Probes of Cosmology*, G. Gelmini, P. Lu, V. Takhistov, Phys. Lett. B **800** 135113, arXiv:1909.04168.

CHAPTER 1

Introduction

Since dark matter (DM) was conjectured by Zwicky in 1933 from application of the virial theorem to observations of the Coma Cluster (and by others around that time with similar arguments), the evidence for its existence has steadily grown. In the 1970s, precise measurements of the stellar rotation curve of the Andromeda galaxy [44] presented the first nearly incontrovertible proof of missing non-luminous gravitational mass. In the intervening fifty years, spectacular demonstrations have shown DM to exist beyond a shadow of a doubt. Notable examples include the displacement of the center of mass from the baryonic center in the Bullet cluster collision [45], baryon acoustic oscillations and other effects in the cosmic microwave background (CMB) spectrum [46], and the perceived flatness of the Universe from distance measurements of Supernova 1A [47, 48]. From the Planck 2018 results derived from the CMB, the DM abundance is $\Omega_{\mathrm{DM}} \approx 0.26$ of the critical density [46], with the other components baryonic matter and dark energy making up the remainder.

Dark matter remains one of the most visible problems in physics, and its elusiveness has sparked numerous dedicated searches for DM candidates. Let us mention a few examples. The most advanced particle physics experiments such as those at the Large Hadron Collider at CERN are well situated to search for DM candidates from new physics such as supersymmetry. They has been instrumental in narrowing the parameter space of Weakly Interacting Massive Particles and other GeV to 100 TeV-scale particles [49, 50]. Besides accelerators, direct and indirect searches for Weakly Interacting Massive Particles are ongoing. The largest direct DM detection experiments use liquid noble gases for their high density and easy scale-ability [51, 52, 53]. In these experiments, large vats of xenon or argon are placed underground to shield from cosmic rays and are monitored closely for signs of DM recoils (i.e. [54, 55]). Gas [56] and crystal experiments [57, 58] have are used. Reactor neutrino experiments take advantage of the large quantities of (anti-)neutrinos produced as a byproduct of fission to carry out precision oscillation measurements. In addition to exploring the active neutrino mixing angles and mass hierarchy, these experiments are also sensitive to sterile neutrinos [59, 60]. Dedicated beam neutrino experiments allow for longer baseline oscillation measurements and higher energies. Examples include MicroBooNE [61] and the planned DUNE [62] experiments. Naturally occurring astrophysical phenomena can be used to explore higher energies, longer distances and timescales than available in Earth-bound laboratories. A significant amount of information can be gleaned from astronomical observations. Structure formation data (i.e. from Lyman-α forests, dwarf galaxies, matter and CMB power spectra) can effectively limit the allowed density of hot and warm DM. Hot DM is relativistic and warm DM is mildly non-relativistic when the temperature of the Universe is about a keV. Some DM candidates annihilate or decay in the present Universe, producing high-energy X-rays, gamma rays, and other particles such as neutrinos. Searches have been conducted for DM annihilation signals from the Galactic center [63] and Milky Way satellites [64]. The tentative 3.5 keV X-ray signal [5, 4], first reported in observations of stacked galaxy clusters, has a possible origin in the decay of a 7 keV sterile neutrino into an active neutrino and a photon. This brief list covers a small portion of the numerous experiments and observations worldwide devoted to the search for DM.

In this thesis, we focus primarily on two DM candidates: sterile neutrinos and primordial black holes. The results were published in Refs. [65, 66, 67, 68] and Refs. [69, 43] respectively.

In the standard model of elementary particles, there are three active neutrinos ν_α, characterized by their flavors $\alpha = e, \mu, \tau$, coupled to the W and Z weak gauge bosons. These neutrinos are massless within the standard model, however, neutrino oscillation experiments [70] show that they are massive. This motivates the study of massive sterile neutrinos, which can explain the small but non-zero active neutrino masses through a "seesaw" mechanism. We consider here sterile neutrinos coupled to the standard model particles only through a mixing with an active neutrino. They can then be produced through non-resonant or resonant oscillation processes, depending on the lepton asymmetry present in the early Universe.

Our earliest probe of the evolution of the Universe comes from the cosmological remnants of Big Bang Nucleosynthesis (BBN). This probe shows that at a temperature of 5 MeV and below, the Universe should be radiation-dominated [71, 72, 73, 74, 75, 76]. Thus, before this epoch, the standard assumption that the universe was radiation dominated with only standard model particles present is yet untested. There are theoretically motivated alternatives to this standard cosmology, e.g. based on moduli decay, quintessence and extra dimensions, which violate these assumptions. These models are of high interest to the study eV- and keV-mass scale sterile neutrinos, whose production often peaks at temperatures > 10 MeV. We consider the properties of sterile neutrinos produced in these non-standard pre-BBN cosmologies.

Primordial black holes (PBH) are important as the only viable non-particle DM candidate, and can form in a variety of ways [77, 78, 79, 80, 81, 82, 83, 84, 85, 86, 87, 88, 28, 89, 90, 91, 92, 93, 94, 95, 96, 34, 97, 98, 99, 100]. There exists a mass window between $M = 10^{17}$-10^{23} g where there are currently no reliable upper bounds on the DM fraction in PBH and PBH can make up all of DM (see Fig. 1.1 for current constraints on the PBH DM density fraction). Even as a subdominant component of DM, intermediate mass PBH with masses ~ 10-$10^5 M_\odot$ can seed the formation of super-massive black holes [101, 102, 103] and are also possible sources of recent LIGO detections of black hole mergers with $> 50 M_\odot$ progenitors. PBH traveling through the interstellar medium would form accretion disks that can be a source of high energy X-rays and cosmic rays. Light PBH with masses $\lesssim 10^{17}$ g can emit significant Hawking radiation, and were the original motivation for considering such radiation [104]. These emissions can be used both to search for and to constrain the DM fraction of PBH.

In Ch. 2, we parameterize a set of non-standard cosmologies and apply them to the production of sterile neutrinos. In the case of non-resonant (DW) production, the general effect is simple for non-standard cosmologies in which only the expansion rate is modified with respect to the standard assumption. Non-standard cosmologies with higher pre-BBN expansion rate (ST1, Kin) result in a lower sterile neutrino abundance, whereas those with lower expansion rate (ST2) result in an increased abundance, always with respect to the

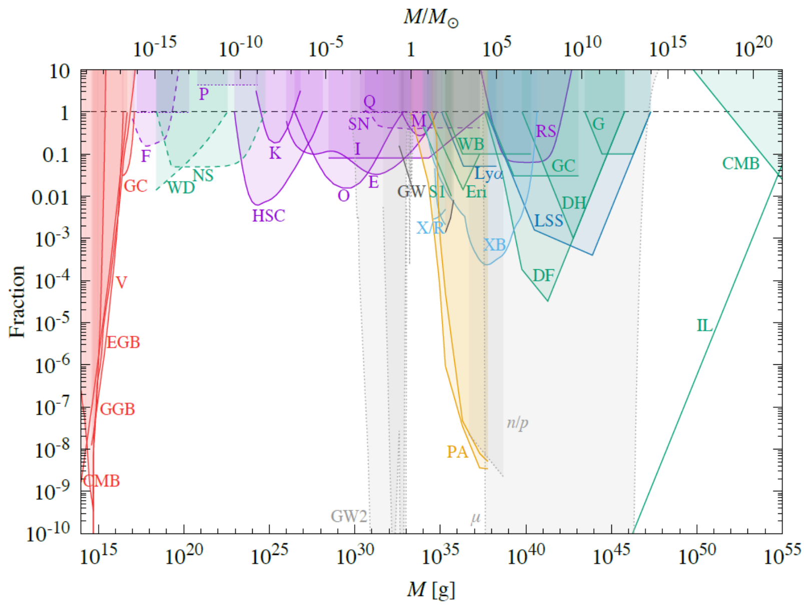

Figure 1.1: Reproduced from Ref. [1]. Many of the currently relevant bounds on PBH fraction are shown, not including two derived in this thesis (see Figs. 3.3 and 3.6). Constraints shown with dashed lines (F, WD, NS) are not reliable and those shown with dotted lines rely on extra assumptions. Thus there exists a mass window between 10^{17} g and 10^{23} g where PBH can make up all of DM.

standard cosmology. Note that non-resonant production is a freeze-in process, in which the initial abundance is zero, and for freeze-out processes, in which the population is initially thermalized, the inverse relations between abundance and expansion rate hold true. We also considered a low-reheating temperature model (LRT), in which the Universe reheats to a temperature of only 5 MeV after inflation. This reheating temperature is much lower than the temperature at which production would be maximal for keV-mass scale neutrinos, about $\sim$ 100 MeV, and thus production is greatly hindered. In Figs. 2.3 and 2.4, we show the line in the mixing angle ($\sin^2 2\theta$) - mass (m_s) parameter space where sterile neutrinos would comprise all of DM, plotted against most of the relevant bounds and experimental regions of interest. Focusing on keV-mass scale neutrinos and the proposed 3.5 keV X-ray signal, we see that in the ST1 cosmology, the parameters of mixing angle/mass necessary to generate the X-rays is detectable by the upcoming TRISTAN and HUNTER experiments. On the other end, in the ST2 cosmology, the full DM abundance line is close to the parameters of the 3.5 X-ray signal. Therefore, sterile neutrinos could be the dominant component of DM and produce the X-ray signal in this particular cosmology. Moreover, the putative signal regions of LSND/MiniBOONE and DANSS/NEOS in the eV-mass scale are entirely free of cosmological limits in ST1 and partially free in LRT.

We also consider coherent and adiabatic resonant (Shi-Fuller) production, which uses level-crossing to efficiently convert active to sterile neutrinos in the presence of a large lepton asymmetry. We compute, for our parameterization of non-standard cosmologies outlined in Section 2.2, the two conditions for resonance. Adiabaticity, requiring many oscillations over resonance, and coherence, the condition that the neutrino does not scatter over the course of resonance, together guarantee this level-crossing to proceed uninhibited. In Figs. 2.6 to 2.9 we show the regions in the mixing angle-mass parameter space where this type of production can occur. Resonant production is most relevant for eV-mass scale neutrinos. For resonant production, the present-day abundance is fixed by the initial lepton asymmetry, and we show results for four different lepton asymmetries, $\mathcal{L} = 10^{-2}, 10^{-3}, 10^{-4}, 10^{-5}$. The effect of non-standard cosmologies on resonant production is not to change the abundance, but rather to move the regions of parameter space where resonance can occur. Figs. 2.6 to 2.9 show that for a wide range of lepton asymmetries, masses, and mixing angles, resonant production can occur in at least one of the cosmologies. Most importantly, many of these coherent and adiabatic regions cover the eV-mass scale neutrino anomalies observed by LSND, MiniBOONE, DANSS, and NEOS. Chapter 2 is based on materials published in Refs. [65, 66, 67, 68].

In Ch. 3, we consider the heating of the interstellar medium by PBH. Primordial black holes traveling through the interstellar medium would accrete gas and dust, forming either a thick or thin disk. For intermediate mass black holes, $10 - 10^5 M_\odot$, the associated photon emission, possible outflows, and dynamical friction can significantly heat the gas. We model these processes using analytical and semi-analytical approximations. Using the parameters of the dwarf galaxy Leo T, we provide a competitive bound on the PBH fraction from $\sim 1 M_\odot$ to $10^7 M_\odot$ by requiring the gas in Leo T to be in thermal equilibrium. This new cosmology-independent bound reinforces existing bounds in the same mass range which rely on different assumptions. Light PBH with masses $\sim 10^{15}$ g to 10^{17} g have lifetimes longer than the age of the Universe and can generate considerable quantities of high energy electrons and photons through Hawking evaporation. Using the same cooling argument as for intermediate mass PBH, we find for non-spinning PBH bounds that are more conservative than previously published. However, for light PBH with large spins which were not studied previously, we find stronger constraints for the DM fraction. Bounds on the PBH fraction derived in this manner are cosmology independent, and unlike CMB bounds, cannot be avoided by forming the PBH after recombination. Chapter 3 is based on materials published in Refs. [69] and [43].

CHAPTER 2

Sterile Neutrinos in Non-standard pre-BBN Cosmologies

2.1 Introduction

The theory of active neutrino oscillations has been extensively tested by experimental measurements of neutrino production in the Sun [105, 106, 107, 108, 109, 110], in nuclear reactors [111, 112, 113, 114], at accelerators [115, 116, 117, 118, 119] and in the atmosphere [120, 70]. While the data has been generally consistent with the three-flavor paradigm, several experiments reported anomalies that could be consistently explained by introducing one or more additional sterile neutrinos into the theory with a mass of $m_s = \mathcal{O}(\text{eV})$. In particular, the short-baseline experiments[1] LSND [121] and MiniBooNE [122] reported excesses of $\bar{\nu}_e$ within $\bar{\nu}_\mu$ beams, and MiniBooNE also found an excess in ν_e appearance [20]. A deficit of ν_e flux from radioactive calibration sources has been observed in gallium experiments[2] [124, 125]. Furthermore, an under-abundance of $\bar{\nu}_e$ has been reported in reactor neutrino experiments[3] [128]. Additionally, combined fits [129, 23, 130] to recent reactor neutrino results by the DANSS [21] and NEOS [22] experiments are consistent with an interpretation based on a sterile neutrino with a mass of $m_s = \mathcal{O}(\text{eV})$ and mixing with a ν_e active neutrino. Reactor neutrino data from the Daya Bay [6], Bugey-3 [7] and PROSPECT [8] experiments constrain these sterile neutrinos and the PTOLEMY [24] and KATRIN [18]

[1] In short-baseline experiment the detectors are located at less than 1 km away from the source.

[2] Recent re-evaluations of gallium cross-sections indicate a weaker sterile neutrino preference [123].

[3] This anomaly has weakened in light of Daya Bay's reactor fuel cycle measurements [126] and observations of spectral distortions not predicted by flux calculations [127].

experiments will be able to test all or part of this parameter space.

Sterile neutrinos with mass of $\mathcal{O}$(keV) and a spectrum close to thermal constitute a viable Warm DM (WDM) candidate (see e.g. Ref. [131]). The mass and mixing of sterile neutrinos that make up all or most of the DM is subject to astrophysical constraints, such as those imposed by Lyman-α forest and X-ray observations. If the keV-mass sterile neutrinos are produced from sterile-active oscillations in the early Universe, these limits disfavor them as the sole DM component (see e.g Ref [132]). These bounds are drastically weakened if sterile neutrinos constitute a sub-dominant DM component (see e.g. Ref. [133]). It has been suggested that the 3.5 keV X-ray emission line observed in 2014 [4, 5] could be produced in the decay of $m_s = 7$ keV sterile neutrinos. The KATRIN laboratory experiment with its proposed TRISTAN upgrade [17], as well as the upcoming HUNTER experiment and its upgrades [19], will test sterile neutrinos in the keV-scale mass range.

If produced in a supernova explosion, sterile neutrinos with mass larger than keV could carry away a sizable fraction of the emitted energy. Asymmetric emission of the sterile neutrinos due to the presence of a strong magnetic field could explain the observed large velocities of pulsars [134]. These effects are independent of the relic abundance of sterile neutrinos and the fraction of the DM they constitute.

Sterile neutrinos without additional interactions beyond the SM that couple to the SM particles only through mixing with active neutrinos, as we assume here, are produced in the early Universe through active-sterile flavor oscillations and collisional processes. For simplicity we assume a ν_s that mixes with only one of the ν_α, which for our figures is ν_e, with a mixing of $\sin\theta$. In the absence of a large lepton asymmetry the oscillations are non-resonant, and the resulting relic number density was first obtained by Dodelson and Widrow [135]. In the standard cosmology this mechanism results in a Fermi-Dirac momentum distribution of sterile neutrinos, with a reduced magnitude with respect to active neutrinos. In the presence of a significant lepton asymmetry in active neutrinos, sterile neutrinos are instead produced via resonant oscillations, as pointed out by Shi and Fuller [136]. Then, the resulting sterile neutrinos have a colder momentum distribution (i.e. with a lower average momentum) that is different from a Fermi-Dirac spectrum. This mechanism was studied in its generality in

Refs. [137] and [138]. In non-minimal particle models, sterile neutrino production could also proceed via other mechanisms, such as decays of additional heavy scalars [139].

In this work we revisit the effects of different pre-BBN cosmologies on sterile neutrinos with mass 10^{-2} eV $< m_s <$ 1 MeV, produced via both non-resonant and resonant active-sterile oscillations. Several related studies have been previously carried out [2, 140, 141]. We update the older constraints of Ref. [2], extend the results of Ref. [140] – pointing out the significance of upcoming laboratory experiments, and extend the analysis of Ref. [141] on keV-mass neutrinos down to 0.01 eV masses.

In addition, we also consider production of sterile neutrinos via resonant active-sterile oscillations, an often considered production mechanism that requires a significant lepton asymmetry in active neutrinos (this is the Shi-Fuller mechanism [136], see also Ref. [137, 138]). In this case, sterile neutrinos are produced with a colder momentum distribution (i.e. with a lower average momentum) that is different from a Fermi-Dirac spectrum, even in the standard cosmology. In particular, we study the effect of different cosmologies on resonantly produced sterile neutrinos with mass 10^{-2} eV $< m_s <$ 1 MeV. Since the production rate is usually not fast enough for sterile neutrinos to equilibrate, the final relic abundance and spectrum are fixed by freeze-in.

In cosmological models in which entropy is conserved, the non-resonant sterile neutrino production depends crucially on the magnitude and temperature dependence of the Hubble expansion rate H. If in the non-standard cosmological phase H is larger than in the standard cosmology, the production of sterile neutrinos during this phase is suppressed. Notably, a particular scalar-tensor model , which was not discussed in the previous study of Ref. [140], allows for a lower expansion rate compared to the standard cosmology and the production is enhanced. We assess the effects of these considerations on the possibility of detecting a sterile neutrino in laboratory experiments. For comparison, we also reconsider low reheating temperature models [2], in which entropy is produced and the radiation bath is subdominant during the non-standard phase. Hence, the dominant non-resonant sterile neutrino production in this scenario occurs during the late standard cosmological phase.

For resonant sterile neutrino production, we will analyze several example cosmological models in which entropy is conserved, characterized by the magnitude and temperature dependence of the Hubble expansion rate H in the non-standard cosmological phase. If H is larger than it would be in the standard cosmology, the resonant production of sterile neutrinos during this phase is suppressed with respect to standard production, and if H is lower, the production is enhanced. If the production is fully resonant, which requires adiabaticity and coherence at the resonance, the relic sterile neutrino number density depends only on the lepton number and not on the expansion rate. However, the mass-mixing regions where this type of production occurs move to smaller (larger) mixing angles for smaller (larger) H values with respect to what it would be in the standard cosmology.

This chapter uses materials published in Refs. [65, 66, 67, 68].

2.2 Non-standard Cosmologies

The expansion rate of the Universe, the Hubble parameter $H = (\dot{a}/a)$ – where a is the cosmological scale factor of the Universe, is determined by the Friedmann equation. In the standard cosmological model [142] the Universe was radiation dominated before BBN, and the highest temperature T of the radiation bath achieved in this epoch is much higher than the temperature $T \simeq 0.8$ MeV at which BBN starts. In the standard cosmology H is

$$H_{\rm Std} = \sqrt{\frac{8\pi G\rho(T)}{3}} = \left(\frac{T^2}{M_{\rm Pl}}\right)\sqrt{\frac{8\pi^3 g_*(T)}{90}}\ . \tag{2.1}$$

Here $\rho(T) = (\pi^2/30)g_*(T)T^4$ is the total energy density, $M_{\rm Pl} = 1.22 \times 10^{19}$ GeV is the Planck mass and $g_*(T)$ is the number of degrees of freedom contributing to the energy density at temperature T. Assuming that only SM particles are present for T higher than the QCD phase transition at $T \simeq 200$ MeV, we have $g_* = 80$ and it is approximately constant (it reaches $g_* = 100$ at $T \simeq 100$ GeV). Close to the QCD phase transition, the value of g_* decreases steeply with decrement of T, and we take a characteristic value of $g_* \simeq 30$ until T decreases to $T = 20$ MeV. Between this temperature and $T = 1$ MeV, when electrons and positrons become non-relativistic and annihilate, $g_* = 10.75$ (see e.g. Refs. [143, 144, 145]).

Unless otherwise stated, for simplicity we use $g_* = 30$ in our figures.

2.2.1 Non-standard pre-BBN cosmologies

The requirement of a successful BBN, which also insures that the subsequent history of the Universe develops as usual, imposes that the Universe is radiation dominated for temperatures $T \lesssim 5$ MeV [71, 72, 73, 74, 75, 76]. However, a non-standard cosmological evolution is allowed at higher temperatures.

Any new additional contribution to the energy density in matter or radiation, or equivalently to the geometry sector of Einstein's equations, results in modification of the Hubble expansion rate through the Friedmann equation. Except for the low reheating temperature model (see below), we consider non-standard cosmologies in which the entropy in matter and radiation is conserved (and hence, the relation between the scale factor of the Universe a and the temperature T follows $a \sim T^{-1}$), but the Hubble expansion H as a function of T is non-standard. In all cosmologies of this type that we will consider H can be given by a simple parameterization [146]

$$H = \eta \left(\frac{T}{T_{\rm tr}}\right)^{\beta} H_{\rm Std} \ , \tag{2.2}$$

where $T_{\rm tr}$ is a reference temperature, which we identify with the temperature at which before BBN the cosmology transitions to the standard cosmology, η and β are real parameters and η is positive.

To preserve BBN, we require that $H_{\rm Std}$ is recovered in Eq. (2.2) at $T < T_{\rm tr} = 5$ MeV. Various phenomenological studies of non-standard cosmologies have been carried out [147, 146, 148, 149, 150], which can be generally classified by the value of the β parameter: $\beta > 2$ for ultra-fast expansion, e.g. when the Universe is dominated by a field with an exponential potential [151] (as in the ekpyrotic scenario [152]), $\beta = 2$ in the Randall-Sundrum type II brane cosmology [153] (see discussion in Ref. [154]), $\beta = 1$ or larger was considered in "fast-expanding" models in which there is an additional energy density component from a non-interacting component [151], $\beta = 1$ in kination models [155, 156, 149, 157, 158, 154], $\beta = 0$ in cosmologies with an overall boost of the Hubble expansion rate, e.g. with a large number of additional relativistic degrees of freedom within the thermal plasma [146], $\beta = -0.8$ can occur in variants of the scalar-tensor cosmology [146, 159] and $\beta = 2/n - 2$ describes $f(R)$ gravity[4], with $f(R) = R + const. \times R^n$ [161].

We will provide expressions in terms of η and β for all the relevant equations in our study, but we will focus our discussion on two often considered modified cosmologies, kination (K) and scalar-tensor (ST) models.

2.2.2 Kination (K)

In the kination phase [155, 156, 149, 157, 158], the kinetic energy of a scalar field ϕ dominates over its potential energy and all other contributions to the total energy density ρ_{tot}. Hence, it also governs the expansion rate in the early Universe. Cosmologies with phases governed by such "fast-rolling" scalar fields can arise in models of quintessence.

During the kination period $\rho_{tot} \simeq \rho_\phi \simeq \dot{\phi}^2/2 \sim a^{-6}$, where ρ_ϕ is the energy density of the scalar ϕ, the associated expansion rate of the Universe during the kination phase is $H_{\rm K} \sim \sqrt{\rho_{tot}} \sim T^3$. The ratio of ϕ-to-photon energy density at $T \simeq 1$ MeV, $\eta_\phi = \rho_\phi/\rho_\gamma$, fixes the contribution of the ϕ kinetic energy to the total energy density at higher temperatures. Hence, one has $H_{\rm K} \simeq \sqrt{\eta_\phi}(T/1\,\text{MeV})H_{\rm Std}$. The value of η_ϕ can be determined by assuming a rapid transition from the kination phase to the radiation dominated phase at the transition temperature T_{tr}, so that $H_{\rm K}(T_{tr}) = H_{\rm Std}(T_{tr})$. With this approximation the expansion rate of the Universe during the kination phase is

$$H_{\rm K} = \left(\frac{T^3}{M_{\rm Pl} T_{\rm tr}}\right)\sqrt{\frac{8\pi^3 g_*}{90}} = \left(\frac{T}{T_{\rm tr}}\right) H_{\rm Std} \quad , \tag{2.3}$$

which in Eq. (2.2) corresponds to $\eta = 1$ and $\beta = 1$.

2.2.3 Scalar-tensor (ST1 and ST2)

Scalar-tensor models of gravity [162, 159] have one or more scalar fields coupled through the metric tensor to the matter sector. These extra fields affect the expansion rate of the

[4]For $n = 2$ this reduces to the Starobinsky model [160].

Universe when the temperature of the thermal bath is higher than the transition temperature T_{tr}, at which a fast transition is assumed to occur before BBN, so that the theory becomes indistinguishable from General Relativity at $T < T_{tr}$. Such scalar-tensor modified cosmologies can appear in models of extra dimensions (e.g. [163]). Depending on the details of the scenario, the respective early Universe expansion rate $H_{\rm ST}$ can be either larger [159] or slightly smaller [164] than the expansion rate within the standard cosmology $H_{\rm Std}$.

As benchmarks, we consider two scalar-tensor models that are extreme in terms of the magnitude of the expansion rate they predict, which we call ST1 and ST2 and assume $T_{\rm tr} = 5$ MeV. In the ST1 model from Ref. [159] the expansion rate is enhanced compared to the standard cosmology, described by

$$H_{\rm ST1} = 7.4\times 10^5 \left(\frac{T_{\rm tr}^{0.8}\ T^{1.2}}{M_{\rm Pl}}\right)\sqrt{\frac{8\pi^3 g_*}{90}} = 7.4\times 10^5 \left(\frac{T}{T_{\rm tr}}\right)^{-0.8} H_{\rm Std}\ , \tag{2.4}$$

which in Eq. (2.2) corresponds to $\eta = 7.4\times 10^5$ and $\beta = -0.8$.

In Ref. [164] it was shown that contributions of an additional "hidden" matter sector beyond the visible sector can result in a reduced expansion rate, compared to the standard cosmology. We choose for ST2 a model of this type with the lowest expansion rate found in Ref. [164], $(H_{\rm ST}/H_{\rm Std})^2 = 10^{-3}$, and for which we choose $\beta = 0$ (given the variations in the behavior of H close to $T_{\rm tr}$ of the numerical solutions shown in Fig. 4 of Ref. [164]). Thus

$$H_{\rm ST2} = 3.2\times 10^{-2}\left(\frac{1}{M_{\rm Pl}}\right)T^2\sqrt{\frac{8\pi^3 g_*}{90}} = 0.03\ H_{\rm Std}\ , \tag{2.5}$$

which in Eq. (2.2) corresponds to $\eta = 0.03$ and $\beta = 0$.

Expansion rates in between $H_{\rm ST1}$ and $H_{\rm ST2}$ can also appear within scalar-tensor models and our analysis can be readily applied to them.

Fig. 2.1 shows the expansion rate of the Universe H as a function of the temperature T of the radiation bath for the Std, $H_{\rm Std}$ (black), K, $H_{\rm K}$ (red), ST1, $H_{\rm ST1}$ (green), and ST2, $H_{\rm ST2}$ (blue), cosmologies assuming a fast transition at $T_{tr} = 5$ MeV and that for $T < T_{tr}$ the cosmology is standard.

We note that since we impose that non-standard cosmologies transition to the standard cosmology before the onset of BBN, restrictions arising from consistency with current astro-

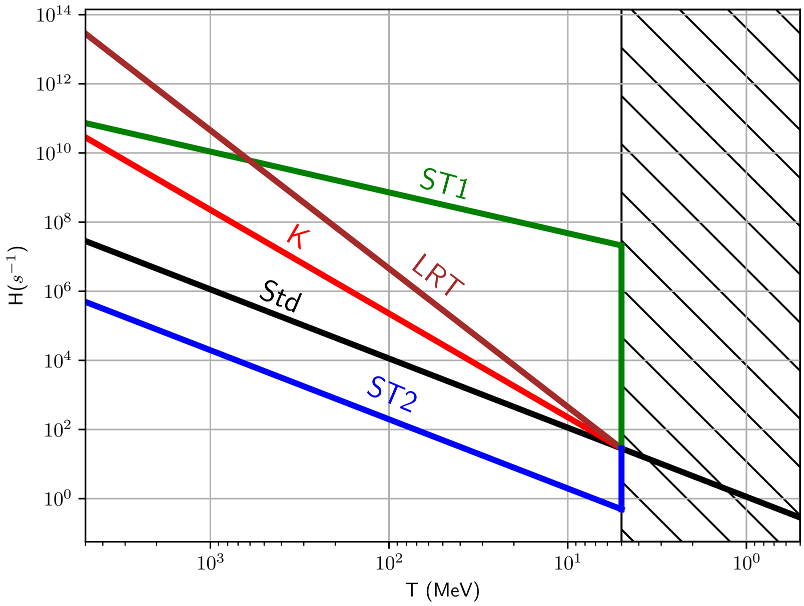

Figure 2.1: Expansion rate of the Universe H as a function of the temperature T of the radiation bath for the Std (black), K (red), ST1 (green) and ST2 (blue) and LRT (brown) cosmologies. At $T_{tr} = 5$ MeV, the upper boundary of the hatched region, all the non-standard cosmologies transition to the standard cosmology. For simplicity, we assume the transition to be sharp in the ST1 and ST2, cosmologies.

physical observations (e.g. signals from neutron star binary mergers [165]) do not affect our considerations.

2.2.4 Low reheating temperature (LRT)

The phenomenological parametrization of Eq. (2.2) does not capture the whole modification to cosmology in models in which the entropy in radiation and matter is not conserved and consequently the temperature T dependence on the scale factor a is different than the usual $T \sim 1/a$. One of these is the low reheating temperature (LRT) model.

In the LRT model a scalar field ϕ oscillates coherently around its true minimum and dominates the energy density of the Universe. Decays of ϕ produce a radiation bath that thermalizes to a temperature T and becomes dominant at the reheating temperature $T_{\rm RH}$. Subsequently, the radiation dominates the energy density of the Universe for $T < T_{\rm RH}$ (see e.g. Refs. [166, 167]). Such field ϕ could be the inflaton itself or a modulus field producing a late episode of entropy production (see e.g. Ref. [168, 169, 170, 171, 172, 173]). Other alternative possibilities include Q-ball decays (e.g. [174]).

In Fig. 2.1, we show the expansion rate for LRT with $T_{\rm RH} = T_{\rm tr} = 5$ MeV in brown. The LRT scenario may drastically alter the DM relic abundance (see e.g. [2, 167, 166, 175, 176] and discussion in Ref. [147]). The non-resonant production of sterile neutrinos in LRT models was considered in Refs. [2, 176], with the assumption that it predominantly occurs during the standard cosmological phase, when $T < T_{\rm RH}$, since the thermal bath is subdominant before reheating. This approximation was validated by considering also the production during the non-standard phase in Ref. [175]. Because the non-resonant production rate is far from its maximum for $T < T_{\rm RH}$, the relic abundance of sterile neutrinos is suppressed in these models. In this study we reconsider the production of sterile neutrinos in LRT model with $T_{\rm RH} = T_{\rm tr} = 5$ MeV [2, 175] and update the observational and experimental bounds on them.

2.3 Non-resonant Production

In the absence of a significant primordial lepton asymmetry, the production of sterile neutrinos happens via non-resonant flavor oscillations between the active neutrinos ν_α of the SM and the sterile neutrino ν_s. This is called the Dodelson-Widrow mechanism (DW) [135] because they derived the analytic solution for the relic number density of sterile neutrinos produced in this manner[5] (see also earlier work [178, 179]). Interactions of active neutrinos with the surrounding plasma during the oscillations act as measurements and cause the collapse of the wave function into one of the oscillating states, which with some probability results in a sterile neutrino. The production rate is usually not fast enough for sterile neutrinos to equilibrate and the process is a freeze-in of the final abundance.

2.3.1 Boltzmann equation

Assuming that only two neutrinos mix, ν_s and one active neutrino ν_α (which we assume to be ν_e in our figures), the time evolution of the phase-space density distribution function of sterile neutrinos $f_{\nu_s}(p,t)$ with respect to the density function of active neutrinos $f_{\nu_\alpha}(p,t)$ is given by the following Boltzmann equation [142, 137]

$$\begin{aligned}\frac{d}{dt}f_{\nu_s}(p,t) &= \frac{\partial}{\partial t}f_{\nu_s}(p,t) - Hp\frac{\partial}{\partial p}f_{\nu_s}(p,t) \\ &= \Gamma(p,t)\Big[f_{\nu_\alpha}(1-f_{\nu_s}) - f_{\nu_s}(1-f_{\nu_\alpha})\Big] \; . \end{aligned} \tag{2.6}$$

Here H is the expansion rate of the Universe, p is the magnitude of the neutrino momentum and $\Gamma(p,t)$ is the conversion rate of active to sterile neutrinos. The active neutrinos are assumed to have a Fermi-Dirac distribution

$$f_{\nu_\alpha} = (e^{\epsilon-\xi}+1)^{-1} \; , \tag{2.7}$$

where $E = p$ because all neutrinos we are interested in are relativistic during the production, $\epsilon = p/T$ is the T-scaled dimensionless momentum, and $\xi = \mu_{\nu_\alpha}/T$ is the T-scaled dimensionless chemical potential with μ_{ν_α} being the chemical potential of active ν_α. In the

[5] The original Dodelson-Widrow results were subsequently corrected by a factor of 2 [177, 137].

DW mechanism μ_{ν_α} is negligible and so we take $\xi = 0$. Since $f_{\nu_s} \ll 1$, we can ignore Pauli blocking, i.e. $(1 - f_{\nu_s}) = 1$, and while $f_{\nu_s} \ll f_{\nu_\alpha}$ we can also neglect the second term on the right hand side of Eq. (2.6). Changing variables, Eq. (2.6) can be further recast into a more convenient form [140, 137]

$$-HT\left(\frac{\partial f_{\nu_s}(E,T)}{\partial T}\right)_{E/T=\epsilon} \simeq \Gamma(E,T) f_{\nu_\alpha}(E,T) \ , \tag{2.8}$$

where the derivative on the left-hand side is computed at constant ϵ.

The conversion rate Γ is the total interaction rate $\Gamma_\alpha = d_\alpha G_F^2 \epsilon T^5$ of the active neutrinos with the surrounding plasma weighted by the average active-sterile oscillation probability $\langle P_m \rangle$ in matter (see Eq. (6.5) and (6.5) of Ref. [137])

$$\Gamma \ = \ \frac{1}{2}\langle P_m(\nu_\alpha \to \nu_s)\rangle \Gamma_\alpha \ \simeq \ \frac{1}{4}\sin^2(2\theta_m) d_\alpha G_F^2 \epsilon T^5 \ . \tag{2.9}$$

In this equation θ_m is the active-sterile mixing angle in matter and d_α is a flavor-dependent parameter, $d_\alpha = 1.27$ for ν_e and $d_\alpha = 0.92$ for ν_μ, ν_τ. Taking into account contributions from the thermal potential V_T and the density potential V_D (that is proportional to the lepton number), the matter mixing angle is given by [137]

$$\sin^2(2\theta_m) = \frac{\sin^2(2\theta)}{\sin^2(2\theta) + \left[\cos(2\theta) - 2\epsilon T(V_D + V_T)/m_s^2\right]^2} \ . \tag{2.10}$$

Here, the quantum damping term in the denominator has been omitted, because it is always negligible for the cases we consider.

For DW production, the density potential V_D is assumed to be negligible. The thermal potential V_T is given by

$$V_T = -B\epsilon T^5 \ , \tag{2.11}$$

where the prefactor B depends on the active neutrino flavor (indicated in parenthesis in the following equation) and on the temperature range (indicated to the right),

$$B = \begin{cases} 10.88 \times 10^{-9}\ \text{GeV}^{-4}\ (e); & 3.02 \times 10^{-9}\ \text{GeV}^{-4}\ (\mu,\tau); \qquad\qquad T \lesssim 20\ \text{MeV} \\ 10.88 \times 10^{-9}\ \text{GeV}^{-4}\ (e,\mu); & 3.02 \times 10^{-9}\ \text{GeV}^{-4}\ (\tau); \qquad 20\ \text{MeV} \lesssim T \lesssim 180\ \text{MeV} \\ 10.88 \times 10^{-9}\ \text{GeV}^{-4}\ (e,\mu,\tau); & \qquad\qquad\qquad\qquad\qquad T \gtrsim 180\ \text{MeV} \end{cases} \tag{2.12}$$

Since the sterile neutrino production rate $(\partial f_{\nu_s}/\partial T)_\epsilon$ is inversely proportional to the expansion rate H (see Eq. (2.8)), high values of $\eta > 1$ in Eq. (2.2) result in suppressed sterile neutrino production, for fixed m_s and $\sin^2(2\theta)$. Hence, non-standard cosmological models with large $\eta \gg 1$ are less constrained by cosmological and astrophysical upper limits on the relic density, and thus larger active-sterile mixing angles become allowed by these limits. The enlarged open parameter space for the K and ST1 (and also LRT) models places visible sterile neutrinos with $m_s \simeq$ keV within closer reach of laboratory experiments such as KATRIN [17] and HUNTER [19]. The effect of ST1 is particularly pronounced and there are no astrophysical or cosmological limits on visible ν_s with $m_s \simeq$ eV, which are tested in reactor and accelerator experiments. On the other hand, the ST2 model of Eq. (2.5) with $\eta < 1$ can produce all of the DM at a smaller mixing angle for a given mass than in the standard cosmological scenario.

2.3.2 Temperature of maximum non-resonant production

The sterile neutrino conversion rate Γ, given in Eq. (2.9) and Eq. (2.10), is suppressed at high temperatures by the thermal potential V_T, so that $\Gamma \sim T^{-7}$. At low temperatures, where V_T is negligible, it is suppressed by the decreasing interaction rate, so that $\Gamma \sim T^5$. Where both regimes cross, for cosmologies with $\beta < 2$, the production rate $(\partial f_s/\partial T)_\epsilon$ has a narrow peak as shown in Fig. 2.2.

The temperature at which the production rate is maximum, $T_{\rm max}$, depends on $H(T)$, but it does not significantly change for the particular cosmologies we consider (see Fig. 2.2). This can be seen in Eq. (4.1) where $T_{\rm max}$ is given as a function of β and ϵ, for $\beta \leq 2$. In the standard cosmology the production is maximal when the V_T term is about 0.2 of the mass term (i.e. the square bracket in the denominator of Eq. (2.10) at $T_{\rm max}$ is $[1 - (2\epsilon/m_s^2)T_{\rm max}V_T(T_{\rm max})] = [1 + 0.2]$) and is very similar in the other cosmologies.

For the standard cosmology ($\beta = 0$),

$$T_{\rm max}^{\rm Std} = 145\ \text{MeV} \left(\frac{m_s}{\text{keV}}\right)^{\frac{1}{3}} \epsilon^{-\frac{1}{3}} \left(\frac{B}{10.88 \times 10^{-9}\ \text{GeV}^{-4}}\right)^{-\frac{1}{6}} . \tag{2.13}$$

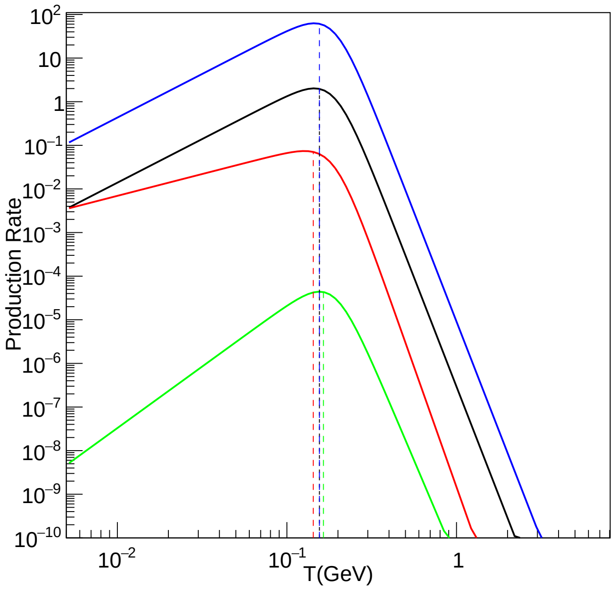

Figure 2.2: Sterile neutrino non-resonant production rate $(\partial f_{\nu_s}(E,T)/\partial T)_\epsilon$ in Eq. (2.8) as function of the temperature T for $\epsilon = 1$ and $m_s = 1$ keV in the Std (black), K (red), ST1 (green) and ST2 (blue) cosmologies, clearly showing their inverse proportionality with the magnitude of the expansion rate H and also minor differences in shape and width due to the different values of the β parameter. The value of $T_{\rm max}$ in each case is indicated by a vertical dashed line of the color of the corresponding cosmology.

For ST1 ($\beta = -0.8$) $T_{\rm max}$ is very similar

$$T_{\rm max}^{\rm ST1} = 156 \text{ MeV} \left(\frac{m_s}{\rm keV}\right)^{\frac{1}{3}} \epsilon^{-\frac{1}{3}} \left(\frac{B}{10.88 \times 10^{-9} \text{ GeV}^{-4}}\right)^{-\frac{1}{6}} \; . \tag{2.14}$$

Since for ST1 the maximum temperature has an inverse scaling dependence on the momentum via ϵ (because β is negative for this model, see Eq. (4.1)), states with lower momentum will be produced earlier, at higher temperatures.

We note that the usual definition of $T_{\rm max}$, as given by Dodelson and Widrow [135], does not depend on ϵ, because it is computed using the production rate integrated over momenta. It coincides with the definition of $T_{\rm max}$ given here for $\epsilon \simeq 1.3$.

$T_{\rm max}^{\rm K}$ and $T_{\rm max}^{\rm ST2}$ for K and ST2 are given in Appendix 4.1.1. They are also very similar.

For non-standard cosmologies with $\beta \geq 2$, the sterile production rate $(\partial f_s/\partial T)_\epsilon$ is continuously increasing with decreasing T, as can be seen in Eq. (4.1) for $\beta = 2$.

2.3.3 Sterile neutrino momentum distribution functions

For the DW production mechanism, a closed-form expression for the momentum distribution function in a non-standard cosmology characterized by H in Eq. (2.2) can be found from Eq. (2.8),

$$f_{\nu_s}(\epsilon) = \int_0^\infty \frac{A' T^{2-\beta}}{(1 + B' T^6)^2} f_{\nu_\alpha} dT = A' \, B'^{(-\frac{1}{2}+\frac{\beta}{6})} \pi \left(\frac{3+\beta}{36}\right) \sec\left(\frac{\beta \pi}{6}\right) f_{\nu_\alpha}(\epsilon) \; , \tag{2.15}$$

where A' and B' are

$$A' = \eta^{-1} \sqrt{\frac{90}{8 g_* \pi^3}} M_{\rm Pl} \Gamma \; , \qquad\qquad B' = \frac{2B\epsilon^2}{m_s^2} \; . \tag{2.16}$$

Replacing in Eq. (2.15) the expressions for A' and B' from Eq. (2.16) and Γ from Eq. (2.9), we obtain the distribution function for generic η and β given in Eq. (4.4) in the Appendix 4.1.2. In the Std cosmology ($\eta = 1, \beta = 0$)

$$f_{\nu_s}^{\rm Std}(\epsilon) = 1.04 \times 10^{-5} \left(\frac{\sin^2(2\theta)}{10^{-10}}\right) \left(\frac{m_s}{\rm keV}\right) \left(\frac{g_*}{30}\right)^{-\frac{1}{2}} \left(\frac{d_\alpha}{1.27}\right) \left(\frac{B}{10.88 \times 10^{-9} {\rm GeV}^{-4}}\right)^{-\frac{1}{2}} f_{\nu_\alpha}(\epsilon) \; . \tag{2.17}$$

For the ST1 cosmology ($\eta = 7.45 \times 10^5$, $\beta = -0.8$), the magnitude of the distribution is much smaller than in the Std cosmology,

$$f_{\nu_s}^{\mathrm{ST1}}(\epsilon) \ = 2.2 \times 10^{-10} \times \epsilon^{-0.27} \left(\frac{\sin^2(2\theta)}{10^{-10}}\right) \left(\frac{m_s}{\mathrm{keV}}\right)^{1.27} \left(\frac{T_{\mathrm{tr}}}{5\ \mathrm{MeV}}\right)^{-0.82} \left(\frac{g_*}{30}\right)^{-\frac{1}{2}} \left(\frac{d_\alpha}{1.27}\right) \left(\frac{B}{10.88 \times 10^{-9}\ \mathrm{GeV}^{-4}}\right)^{-0.64} f_{\nu_\alpha}(\epsilon)\ . \tag{2.18}$$

The distribution functions for the K, ST2 and LRT cosmologies are given in the Appendix 4.1.2.

We can clearly see from Eqs. (2.15) and (2.16), and further in Eq. (4.4)), that cosmologies with larger expansion rates (i.e. larger η) require higher mixing angles to produce the same relic density, and vice-versa. For cosmologies with $\beta \neq 0$, there is an extra momentum dependence that makes the distribution warmer (i.e. favors larger ϵ values) for $\beta > 0$ or colder (favors smaller ϵ values) for $\beta < 0$ than the standard Fermi-Dirac.

2.3.4 Sterile neutrino number densities

The number density n_{ν_α} of active neutrinos is obtained by integration over momentum of the distribution function of Eq. (2.7)

$$n_{\nu_\alpha}(T_{\nu_\alpha}) = \left(\frac{3\zeta(3)}{2\pi^2}\right) T_{\nu_\alpha}^3, \tag{2.19}$$

where for photon temperatures $T > 1$ MeV, the temperature of the neutrino background is $T_{\nu_\alpha} = T$, and for $T < 1$ MeV, $T_{\nu_\alpha} = (4/11)T$. The number density n_{ν_s} of sterile neutrinos can be obtained in a similar manner

$$n_{\nu_s}(T_{\nu_s}) = 2\int_0^\infty \frac{d^3p}{(2\pi)^3} f_{\nu_s}(p) = \frac{T_{\nu_s}^3}{\pi^2}\int_0^\infty d\epsilon\ \epsilon^2 f_{\nu_s}(\epsilon) = T_{\nu_s}^3 C F_{2+\frac{\beta}{3}}(0)\ , \tag{2.20}$$

considering that active neutrinos have a Fermi-Dirac distribution, as given in Eq. (2.7), with $\xi = 0$ (since for non-resonant production the chemical potential of active neutrinos is negligible) and T_{ν_s} being the temperature of the sterile neutrino background. Here, $C = f_{\nu_s}(\epsilon)\left(\pi^2 \epsilon^{\beta/3} f_{\nu_\alpha}(\epsilon)\right)^{-1}$ is a constant (notice that in Eq. (4.4) f_{ν_s} depends on ϵ only through the product $\epsilon^{\beta/3} f_{\nu_\alpha}(\epsilon)$) and

$$F_k(\xi) = \int_0^\infty dx \frac{x^k}{e^{x-\xi}+1}\ , \tag{2.21}$$

is the relativistic Fermi integral. The relic sterile neutrino number density as function of η and β is given in Eq. (4.10).

The term $\beta/3$ in the definition of the index $k = 2 + \beta/3$ comes from the $\epsilon^{\beta/3}$ dependence of f_{ν_s} in Eq. (4.4) (for LRT, the index is instead $k = 3$ because of the ϵ^1 dependence of $f_{\nu_s}^{\rm LRT}$ in Eq. (4.7)).

The ratio of sterile and active neutrino number densities at the same temperature can be easily stated in terms of the ratio of momentum distributions. For the parametrization of H in Eq. (2.2), this ratio is given in Eq. (4.8).

In the standard cosmology, for which $n_{\nu_s}(T)/n_{\nu_a}(T) = f_{\nu_s}(\epsilon)/f_{\nu_\alpha}(\epsilon)$, the relic sterile neutrino number density is

$$\begin{aligned} n_{\nu_s}^{\rm Std}(T_{\nu_s}) \ &= 1.04 \times 10^{-5} \left(\frac{\sin^2 2\theta}{10^{-10}}\right)\left(\frac{m_s}{\rm keV}\right)\left(\frac{T_{\nu_s}}{T_{\nu_\alpha}}\right)^3\left(\frac{g_*}{30}\right)^{-\frac{1}{2}} \\ &\times \left(\frac{d_\alpha}{1.27}\right)\left(\frac{B}{10.88 \times 10^{-9}{\rm GeV}^{-4}}\right)^{-\frac{1}{2}} n_{\nu_\alpha}(T_{\nu_\alpha}) \ . \end{aligned} \tag{2.22}$$

Thus, the present number density is

$$\begin{aligned} n_{\nu_s}^{\rm Std} \ &= 4.2 \times 10^{-4}{\rm cm}^{-3} \left(\frac{\sin^2 2\theta}{10^{-10}}\right)\left(\frac{m_s}{\rm keV}\right)\left(\frac{T_{\nu,0}}{1.95\ {\rm K}}\right)^3 \\ &\times \left(\frac{g_*}{30}\right)^{-\frac{3}{2}}\left(\frac{d_\alpha}{1.27}\right)\left(\frac{B}{10.88 \times 10^{-9}\ {\rm GeV}^{-4}}\right)^{-\frac{1}{2}} \ , \end{aligned} \tag{2.23}$$

where $T_{\nu,0} = 1.95$ K $= 0.17$ meV is the present temperature of the active relic neutrino background.

In the ST1 model, $n_{\nu_s}(T)/n_{\nu_a}(T) = 0.77\ \epsilon^{0.27}(f_{\nu_s}(\epsilon)/f_{\nu_\alpha}(\epsilon))$, and the number density is significantly reduced for the same mass and mixing angle,

$$\begin{aligned} n_{\nu_s}^{\rm ST1}(T_{\nu_\alpha}) \ &= 1.71 \times 10^{-10} \left(\frac{\sin^2 2\theta}{10^{-10}}\right)\left(\frac{m_s}{\rm keV}\right)^{1.27}\left(\frac{T_{\rm tr}}{5\ {\rm MeV}}\right)^{-0.82}\left(\frac{T_{\nu_s}}{T_{\nu_\alpha}}\right)^3 \\ &\times \left(\frac{g_*}{30}\right)^{-\frac{1}{2}}\left(\frac{d_\alpha}{1.27}\right)\left(\frac{B}{10.88 \times 10^{-9}\ {\rm GeV}^{-4}}\right)^{-0.64} n_{\nu_\alpha}(T_{\nu_\alpha}) \ , \end{aligned} \tag{2.24}$$

with the present number density being

$$\begin{aligned} n_{\nu_s}^{\rm ST1} &= 6.89 \times 10^{-9}\ {\rm cm}^{-3} \left(\frac{\sin^2 2\theta}{10^{-10}}\right)\left(\frac{m_s}{\rm keV}\right)^{1.27}\left(\frac{T_{\rm tr}}{5\ {\rm MeV}}\right)^{-0.82}\left(\frac{T_{\nu,0}}{1.95\ {\rm K}}\right)^3 \\ &\times \left(\frac{g_*}{30}\right)^{-\frac{3}{2}}\left(\frac{d_\alpha}{1.27}\right)\left(\frac{B}{10.88 \times 10^{-9}\ {\rm GeV}^{-4}}\right)^{-0.64} \ . \end{aligned} \tag{2.25}$$

Here, g_* is the number of relativistic degrees of freedom when sterile neutrinos are produced, which we take to be $g_*(T_{\rm max})$. Thus, at present, the ratio of temperatures of the sterile and active neutrinos is $(T_{\nu_s,0}/T_{\nu,0}) = (10.75/g_*)^{1/3}$.

The present number densities for the K and ST2 and also LRT cosmologies are given in the Appendix 4.1.3.

2.3.5 Relativistic energy density

The energy density of relativistic active neutrinos is given by (Eq. (2.7))

$$\rho_{\nu_\alpha} = 2\int_0^\infty \frac{d^3p}{(2\pi)^3}\, p\, f_{\nu_\alpha}(p) = \frac{T^4}{\pi^2}\int_0^\infty d\epsilon\, \epsilon^3 f_{\nu_\alpha}(\epsilon) = \frac{T^4}{\pi^2}F_3(0)\ , \tag{2.26}$$

where the Fermi integral $F_k(\xi)$ is defined in Eq. (2.21). Similarly, the energy density of relativistic sterile neutrinos is

$$\rho_{\nu_s} = 2\int_0^\infty \frac{d^3p}{(2\pi)^3}\, p\, f_{\nu_s}(p) = \frac{T^4}{\pi^2}\int_0^\infty d\epsilon\, \epsilon^3 f_{\nu_s}(\epsilon) = T^4 C F_{3+\frac{\beta}{3}}(0)\ . \tag{2.27}$$

To obtain the last equality we used the momentum distributions for the models with H given in Eq. (2.2). The resulting energy density in terms of the parameters η and β is given in Eq. (4.19).

For the LRT model, the index in the function F_k in this equation is not $k = 3 + \beta/3$ but instead $k = 4$ because of the ϵ dependence of $f_{\nu_s}^{\rm LRT}$ in Eq. (4.7).

The ratio of sterile and active neutrino relic densities at the same temperature T can be easily stated in terms of the ratio of momentum distributions. This ratio is given in terms of η and β in Eq. (4.17).

In the Std cosmology, $\rho_{\nu_s}(T)/\rho_{\nu_a}(T) = n_{\nu_s}(T)/n_{\nu_a}(T) = f_{\nu_s}(\epsilon)/f_{\nu_\alpha}(\epsilon)$, and the energy density of non-resonantly produced relativistic sterile neutrinos with temperature T_{ν_s} is

$$\begin{aligned}\rho_{\nu_s}^{\rm Std}(T_{\nu_s}) &= 1.04\times10^{-5}\ \left(\frac{\sin^2 2\theta}{10^{-10}}\right)\left(\frac{m_s}{\rm keV}\right)\left(\frac{T_{\nu_s}}{T_{\nu_\alpha}}\right)^4\left(\frac{g_*}{30}\right)^{-\frac{1}{2}} \\ &\times\left(\frac{d_\alpha}{1.27}\right)\left(\frac{B}{10.88\times10^{-9}\ {\rm GeV}^{-4}}\right)^{-\frac{1}{2}}\rho_{\nu_\alpha}(T_{\nu_\alpha})\ ,\end{aligned} \tag{2.28}$$

or,

$$\rho^{\rm Std}_{\nu_s}(T_{\nu_s}) = 7.79\times 10^{26}\ \frac{\rm MeV}{\rm cm^3}\left(\frac{\sin^2 2\theta}{10^{-10}}\right)\left(\frac{m_s}{\rm keV}\right)\left(\frac{T_{\nu_s}}{1\ \rm MeV}\right)^4\left(\frac{g_*}{30}\right)^{-\frac{1}{2}}$$
$$\times\left(\frac{d_\alpha}{1.27}\right)\left(\frac{B}{10.88\times 10^{-9}\ \rm GeV^{-4}}\right)^{-\frac{1}{2}}\ . \tag{2.29}$$

For ST1 instead, $\rho_{\nu_s}(T)/\rho_{\nu_a}(T) = 0.92(n_{\nu_s}(T)/n_{\nu_a}(T))$ and the density is much smaller

$$\rho^{\rm ST1}_{\nu_s}(T_{\nu_s})\ = 1.56\times 10^{-10}\ \left(\frac{\sin^2 2\theta}{10^{-10}}\right)\left(\frac{m_s}{\rm keV}\right)^{1.27}\left(\frac{T_{\rm tr}}{5\ \rm MeV}\right)^{-0.82}\left(\frac{T_{\nu_s}}{T_{\nu_\alpha}}\right)^4\left(\frac{g_*}{30}\right)^{-\frac{1}{2}}$$
$$\times\left(\frac{d_\alpha}{1.27}\right)\left(\frac{B}{10.88\times 10^{-9}\ \rm GeV^{-4}}\right)^{-0.64}\ \rho_{\nu_\alpha}(T_{\nu_\alpha})\ , \tag{2.30}$$

or,

$$\rho^{\rm ST1}_{\nu_s}(T_{\nu_s}) = 1.17\times 10^{22}\ \frac{\rm MeV}{\rm cm^3}\left(\frac{\sin^2 2\theta}{10^{-10}}\right)\left(\frac{m_s}{\rm keV}\right)^{1.27}\left(\frac{T_{\rm tr}}{5\ \rm MeV}\right)^{-0.82}\left(\frac{T_{\nu_s}}{1\ \rm MeV}\right)^4\left(\frac{g_*}{30}\right)^{-\frac{1}{2}}$$
$$\times\left(\frac{d_\alpha}{1.27}\right)\left(\frac{B}{10.88\times 10^{-9}\ \rm GeV^{-4}}\right)^{-0.64}\ . \tag{2.31}$$

The relativistic energy density $\rho^{\rm K}_{\nu_s}$, $\rho^{\rm ST2}_{\nu_s}$ and $\rho^{\rm LRT}_{\nu_s}$ for the K, ST2 and LRT cosmologies are given in Appendix 4.1.4.

These expressions apply after the bulk of the sterile neutrinos has been produced and while they are relativistic: $m_s < T < T_{\rm max}$ (or for $m_s < T < T_{\rm RH}$ in LRT models).

The average T-scaled dimensionless sterile neutrino momentum $\langle\epsilon\rangle$ in the different cosmologies is given in terms of the parameters η and β in Eq. (2.2) for $T_{\rm tr} = 5$ MeV is

$$\langle\epsilon\rangle = \frac{\rho_{\nu_s}(T)}{T\ n_{\nu_s}(T)} = \frac{F_{3+\beta/3}(0)}{F_{2+\beta/3}(0)} = \begin{cases} 3.15, & \text{Std} \\ 3.47, & \text{K} \\ 2.89, & \text{ST1} \\ 3.15, & \text{ST2} \end{cases} \tag{2.32}$$

where $F_k(\xi)$ is given in Eq. (2.21) as before. For the LTR model with $T_{\rm RH} = 5$ MeV

$$\langle\epsilon\rangle = \frac{\rho_{\nu_s}(T)}{T\ n_{\nu_s}(T)} = \frac{F_4(0)}{F_3(0)} = \qquad 4.11, \quad \text{LRT} \tag{2.33}$$

2.3.6 Present fraction of the DM in non-resonantly produced sterile neutrinos

The present sterile neutrino relic density must not exceed the DM density, i.e. $\Omega_{\nu_s} = \rho_{\nu_s}/\rho_{\rm crit} \leq \Omega_{\rm DM} = \rho_{\rm DM}/\rho_{\rm crit}$, where $\Omega_{DM} h^2 = 0.1186 \simeq 0.12$, $\rho_{\rm crit} = 1.054 \times 10^{-5} h^2$ GeV/cm^3 is the critical density of the Universe and $h = 0.678$ [9]. Hence, the fraction of the DM consisting of sterile neutrinos $f_{s,\rm DM} = \rho_{\nu_s}/\rho_{\rm DM}$ must be $f_{s,\rm DM} \leq 1$.

At present, all the sterile neutrinos we consider (i.e. all neutrinos with $m_s > 10^{-2}$ eV), are non-relativistic, thus $\rho_{\nu_s,0} = m_s n_{\nu_s,0}$. Hence, the present fraction of the DM in sterile neutrinos is $f_{s,\rm DM} = (n_{\nu_s,0}\ m_s/\rho_{\rm DM})$. This fraction is given as a function of the η and β parameters in Eq. (4.25). In the Std cosmology this fraction is

$$\begin{aligned} f^{\rm Std}_{s,\rm DM} = \left(\frac{n_{\nu_s,0}\, m_s}{\rho_{\rm DM}}\right)^{\rm Std} &= \\ = 2.79 \times 10^{-4} &\left(\frac{\sin^2(2\theta)}{10^{-10}}\right) \left(\frac{m_s}{\rm keV}\right)^2 \left(\frac{T_{\nu,0}}{1.95\ \rm K}\right)^3 \\ \times &\left(\frac{g_*}{30}\right)^{-\frac{3}{2}} \left(\frac{d_\alpha}{1.27}\right) \left(\frac{\Omega_{\rm DM} h^2}{0.12}\right) \left(\frac{B}{10.88 \times 10^{-9}\ \rm GeV^{-4}}\right)^{-\frac{1}{2}} \end{aligned} \tag{2.34}$$

and in the ST1 cosmology is instead

$$\begin{aligned} f^{\rm ST1}_{s,\rm DM} = \left(\frac{n_{\nu_s,0}\, m_s}{\rho_{\rm DM}}\right)^{\rm ST1} &= \\ = 4.60 \times 10^{-9} &\left(\frac{\sin^2(2\theta)}{10^{-10}}\right) \left(\frac{m_s}{\rm keV}\right)^{2.27} \left(\frac{T_{\rm tr}}{5\ \rm MeV}\right)^{-0.82} \left(\frac{T_{\nu,0}}{1.95\ \rm K}\right)^3 \\ \times &\left(\frac{g_*}{30}\right)^{-\frac{3}{2}} \left(\frac{d_\alpha}{1.27}\right) \left(\frac{\Omega_{\rm DM} h^2}{0.12}\right) \left(\frac{B}{10.88 \times 10^{-9}\ \rm GeV^{-4}}\right)^{-0.64} . \end{aligned} \tag{2.35}$$

The present sterile neutrino fraction of the DM for K, ST2 and also the LRT cosmologies are given in Appendix 4.1.5.

The condition $f_{s,\rm DM} = 1$ defines the mixing we call $\sin^2(2\theta)_{\rm DW,lim}$ as a function of m_s. In the log-log scales used in our figures, this is a straight line on which sterile neutrinos account for the entirety of the DM. As a function of η and β, $\sin^2(2\theta)_{\rm DW,lim}(m_s)$ is given in Eq. (4.29).

In the Std cosmology

$$\sin^2(2\theta)^{\rm STD}_{\rm DW,lim} = 3.58\times10^{-7}\left(\frac{m_s}{\rm keV}\right)^{-2}\left(\frac{T_{\nu,0}}{1.95\ {\rm K}}\right)^{-3}\left(\frac{g_*}{30}\right)^{\frac{3}{2}}\left(\frac{d_\alpha}{1.27}\right)^{-1} \times\left(\frac{\Omega_{\rm DM}h^2}{0.12}\right)^{-1}\left(\frac{B}{10.88\times10^{-9}\ {\rm GeV}^{-4}}\right)^{\frac{1}{2}} \tag{2.36}$$

and in the ST1 cosmology

$$\sin^2(2\theta)^{\rm ST1}_{\rm DW,lim} = 2.19\times10^{-2}\left(\frac{m_s}{\rm keV}\right)^{-2.27}\left(\frac{T_{\rm tr}}{5\ {\rm MeV}}\right)^{0.82}\left(\frac{T_{\nu,0}}{1.95\ {\rm K}}\right)^{-3}\left(\frac{g_*}{30}\right)^{\frac{3}{2}} \times\left(\frac{d_\alpha}{1.27}\right)^{-1}\left(\frac{\Omega_{\rm DM}h^2}{0.12}\right)^{-1}\left(\frac{B}{10.88\times10^{-9}\ {\rm GeV}^{-4}}\right)^{0.64}. \tag{2.37}$$

In Appendix 4.1.6 this function is given for the K and ST2 cosmologies, and also for the LRT (see Eq. (4.32)).

In Figs. 2.3 and 2.4, the fractions $f_{s,\rm DM} = 1$ is indicated with a solid black lines and $f_{s,\rm DM} = 10^{-1}, 10^{-2}, 10^{-3}$ are indicated with dotted black lines.

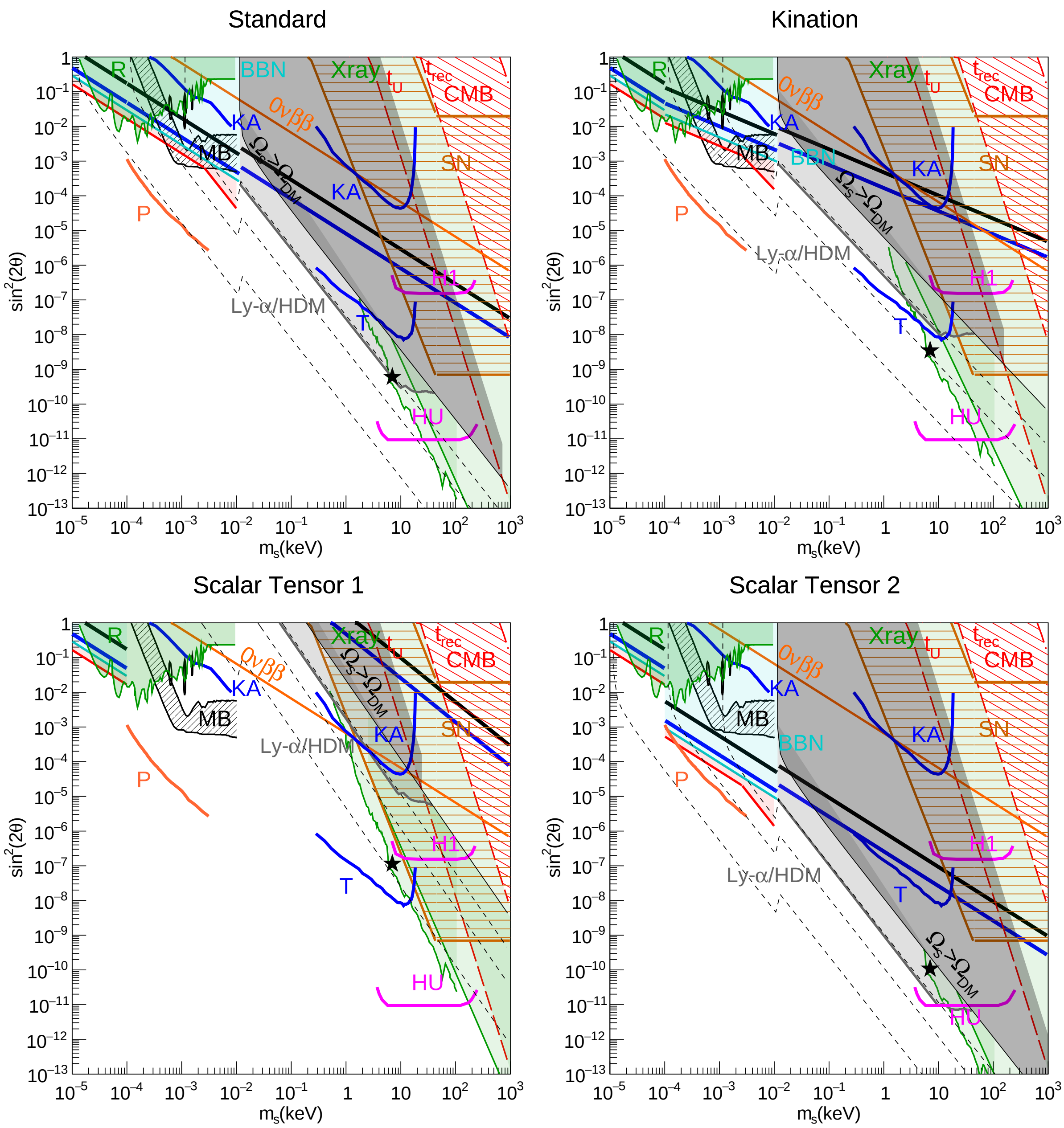

Figure 2.3: Present relic abundance, limits and regions of interest for standard, kination and scalar-tensor cosmologies taking thermalization into account (see section 2.4). See caption in Fig. 2.4.

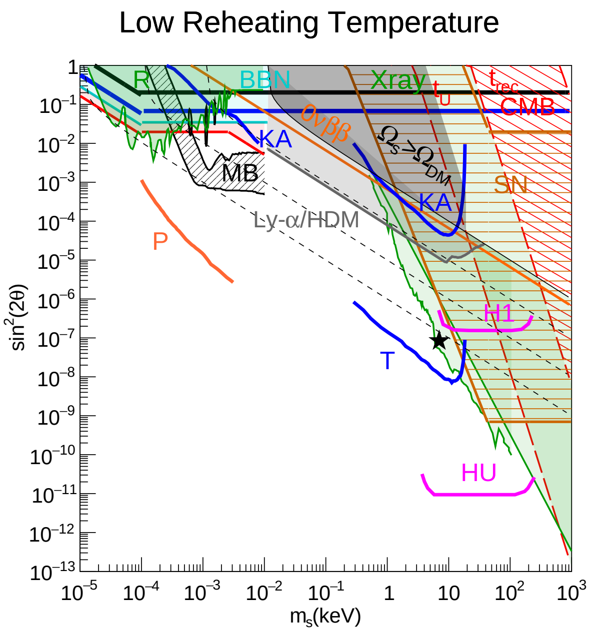

Figure 2.4: Present relic abundance, limits and regions of interest in the mass-mixing space of a ν_s mixed with ν_e, for LRT cosmology with $T_{\mathrm{RH}} = 5$ MeV [2], taking thermalization into account (see section 2.4). Shown are the fraction of the DM in ν_s of 1 (black solid line) and 10^{-1}, 10^{-2} and 10^{-3} (black dotted lines), the forbidden region $\Omega_s/\Omega_{\mathrm{DM}} > 1$ (diagonally hatched in black), lifetimes $\tau = t_U$, t_{rec} and t_{th} (see text) of Majorana ν_s (straight long dashed red lines), the region (SN) disfavored by supernovae [3] (horizontally hatched in brown), the location of the 3.5 keV X-ray signal [4, 5] for each cosmology (black star). The regions rejected by reactor neutrino (R) experiments (Daya Bay [6], Bugey-3 [7] and PROSPECT [8]) shown in green, limits on N_{eff} during BBN [9] (BBN) in cyan, Lyman-alpha limits [10] (Ly-α/HDM) in gray, X-ray limits [11, 12, 13] including DEBRA [14] (Xray) in green, $0\nu\beta\beta$ decays [15] ($0\nu\beta\beta$) in orange and CMB spectrum distortions [16] (CMB) diagonally hatched in red. Current/future sensitivity of KATRIN (KA) in the keV [17] and eV [18] mass range, its TRISTAN upgrade in 1 yr (T) and in 3 yr (T2) [17] shown by blue solid lines. Magenta solid lines show the reach of the phases 1A (H1A) and 1B (H1B) of HUNTER, and its upgrade (HU) [19]. The 4-σ band of compatibility with LSND and MiniBooNE results (MB) in Fig. 4 of [20] is shown densely hatched in black. The three black vertical elliptical contours are the regions allowed at 3-σ by DANSS [21] and NEOS [22] data in Fig. 4 of [23]). Orange solid lines show the reach of PTOLEMY for 10 mg-yr (P) and 100 g-yr (P2) exposures (from Figs. 6 and 7 of [24]).

2.4 Thermalization

In the previous sections, we have considered the cosmological dependence of non-resonantly produced sterile neutrinos. We discussed there the sensitivity of sterile neutrino production to cosmologies that differ from the standard radiation dominated cosmology (STD) before Big Bang Nucleosynthesis (BBN), specifically before the temperature of the Universe was 5 MeV. The lower limit on the highest temperature of the radiation-dominated epoch in which BBN happened is close to 5 Mev [180, 72, 71, 73, 74, 75, 76]. Thus, the cosmological evolution in the Universe before the temperature of the Universe was about 5 MeV is unknown and could differ from the STD. Alternative cosmologies can often appear in motivated theories. As examples, we have considered two distinct Scalar-Tensor models (ST1 [159] and ST2 [164]), Kination (K) [155, 156, 149, 157, 158] as well as Low Reheating Temperature (LRT) scenario [2] (see also e.g. [166, 167, 176, 175, 71, 141, 72, 180]), besides the STD cosmology (see section 2.2 for a detailed description of the different models). We discussed how the resulting limits and regions of interest in the mass-mixing $(m_s, \sin^2 2\theta)$ plane are affected for a sterile neutrino of mass m_s that is assumed to have a mixing $\sin\theta$ only with the active electron neutrino.

In the preceding sections, we presented a simplified treatment of sterile neutrino production for the parameter region where mixing angles are very large. There, the momentum $\vec{p}$ distribution $f_{\nu_s}(E,T)$ of sterile neutrinos of energy $E = |\vec{p}|$, which are relativistic at the production temperature T, is not much smaller than the distribution of active neutrinos $f_{\nu_\alpha}(E,T)$. In part of this region sterile neutrinos can thermalize in the Early Universe, so that $f_{\nu_s}(E,T) = f_{\nu_\alpha}(E,T)$. When thermalized, sterile neutrinos have the same number density of one active neutrino species, i.e. during BBN and later $\Delta N_{\rm eff} = 1$ (or close to 1, depending on entropy dilution), a value that is forbidden by present cosmological limits. While neutrino thermalization has been extensively studied with numerical methods (e.g. [72, 181]), in this addendum we analyze these effects analytically.

We show, always using analytic expressions as in our previous studies, that the regions allowed by all sterile neutrino bounds are not affected by the present considerations.

2.4.1 Approaching Thermalization

In our analysis of section 2.3, we assumed $f_{\nu_s} \ll f_{\nu_\alpha}$ and thus neglected the second term on the right hand side of the Boltzmann equation

$$\left(\frac{\partial f_{\nu_s}(E,T)}{\partial T}\right)_{\epsilon=E/T} = -\frac{\Gamma_s(E,T)}{HT}[f_{\nu_\alpha}(E,T) - f_{\nu_s}(E,T)] \ . \tag{2.38}$$

where $\epsilon = E/T = |\vec{p}|/T$ is the T-scaled dimensionless momentum and the derivative on the left hand side is computed at constant ϵ. Here H is the expansion rate of the Universe, which for $T > T_{\rm tr}$ we parameterize as $H = \eta(T/T_{\rm tr})^\beta H_{\rm STD}$ (see section 2.2 for definitions). We also consider a LRT model with reheating temperature $T_{\rm RH} = T_{\rm tr}$. $\Gamma_s(E,T)$ in Eq. (2.38) is the conversion rate of active to sterile neutrinos,

$$\Gamma \ = \ \frac{1}{2}\langle P_m(\nu_\alpha \to \nu_s)\rangle\Gamma_\alpha \ \simeq \ \frac{1}{4}\sin^2(2\theta_m) d_\alpha G_F^2 \epsilon T^5 \ . \tag{2.39}$$

where $d_\alpha = 1.27$ for ν_e and G_F is the Fermi constant. In the absence of a large lepton asymmetry, the matter mixing angle is

$$\sin^2(2\theta_m) = \frac{\sin^2(2\theta)}{\sin^2(2\theta) + \Big[\cos(2\theta) - 2\epsilon T V_T/m_s^2\Big]^2} \ , \tag{2.40}$$

where for ν_e the thermal potential is $V_T = -10.88 \times 10^{-9}$ GeV^{-4}.

If $f_{\nu_s} \ll f_{\nu_\alpha}$, f_{ν_s} can be neglected on the right hand side of Eq. (2.38), which amounts to neglecting the inverse oscillation process $\nu_s \to \nu_\alpha$. This is a good approximation for most of the large parameter space we studied with our analytic methods, 0.01 eV $< m_s <$ 1 MeV and $10^{-13} < \sin^2 2\theta < 1$. However, this approximation fails for very large mixing angles, for which sterile neutrinos thermalize, thus $f_{\nu_s} = f_{\nu_\alpha}$ and the right hand side of Eq. (2.38) vanishes.

The "linear" equation Eq. (2.38) without f_{ν_s} in the right hand side, can be analytically solved for f_{ν_s}, to obtain what we call now $f_{\nu_s-\rm lin}$ (see section 2.3 for a detailed discussion) for all the cosmologies we consider,

$$\begin{aligned}
f^{\rm STD}_{\nu_s-{\rm lin}}(\epsilon) &= 1.04\times 10^{-5}\left(\frac{\sin^2(2\theta)}{10^{-10}}\right)\left(\frac{m_s}{\rm keV}\right)\left(\frac{g_*}{30}\right)^{-\frac{1}{2}}\left(\frac{d_\alpha}{1.27}\right) f_{\nu_\alpha}(\epsilon)\ ,\\
f^{\rm K}_{\nu_s-{\rm lin}}(\epsilon) &= 4.2\times 10^{-7}\epsilon^{\frac{1}{3}}\left(\frac{\sin^2(2\theta)}{10^{-10}}\right)\left(\frac{m_s}{\rm keV}\right)^{\frac{2}{3}}\left(\frac{g_*}{30}\right)^{-\frac{1}{2}}\left(\frac{d_\alpha}{1.27}\right) f_{\nu_\alpha}(\epsilon)\ ,\\
f^{\rm ST1}_{\nu_s-{\rm lin}}(\epsilon) &= 2.2\times 10^{-10}\epsilon^{-0.27}\left(\frac{\sin^2(2\theta)}{10^{-10}}\right)\left(\frac{m_s}{\rm keV}\right)^{1.27}\left(\frac{g_*}{30}\right)^{-\frac{1}{2}}\left(\frac{d_\alpha}{1.27}\right) f_{\nu_\alpha}(\epsilon)\ ,\\
f^{\rm ST2}_{\nu_s-{\rm lin}}(\epsilon) &= 3.25\times 10^{-4}\left(\frac{\sin^2(2\theta)}{10^{-10}}\right)\left(\frac{m_s}{\rm keV}\right)\left(\frac{g_*}{30}\right)^{-\frac{1}{2}}\left(\frac{d_\alpha}{1.27}\right) f_{\nu_\alpha}(\epsilon)\\
f^{\rm LRT}_{\nu_s-{\rm lin}} &= 3.6\times 10^{-10}\,\epsilon\left(\frac{\sin^2(2\theta)}{10^{-10}}\right)\left(\frac{d_\alpha}{1.13}\right) f_{\nu_\alpha}(\epsilon)\ .
\end{aligned} \tag{2.41}$$

Integrating these distributions over momentum yields the corresponding “linear" number densities $n_{\nu_s-{\rm lin}}$. Requiring the present sterile neutrino energy density not to exceed the present DM density $m_s n_{\nu_s-{\rm lin}}/\rho_c < \rho_{DM}/\rho_c = \Omega_{DM}$, where ρ_c is the critical density, yields the “old" mixing angle limits found in section 2.3 (in the linear approximation),

$$\begin{aligned}
\sin^2(2\theta)^{\rm STD}_{\rm old} &= 3.58\times 10^{-7}\left(\frac{m_s}{\rm keV}\right)^{-2}\left(\frac{g_*}{30}\right)^{\frac{3}{2}}\left(\frac{d_\alpha}{1.27}\right)^{-1}\left(\frac{\Omega_{\rm DM}h^2}{0.12}\right)^{-1}\ ,\\
\sin^2(2\theta)^{\rm K}_{\rm old} &= 6.26\times 10^{-6}\left(\frac{m_s}{\rm keV}\right)^{-\frac{5}{3}}\left(\frac{g_*}{30}\right)^{\frac{3}{2}}\left(\frac{d_\alpha}{1.27}\right)^{-1}\left(\frac{\Omega_{\rm DM}h^2}{0.12}\right)^{-1}\ ,\\
\sin^2(2\theta)^{\rm ST1}_{\rm old} &= 2.19\times 10^{-2}\left(\frac{m_s}{\rm keV}\right)^{-2.27}\left(\frac{g_*}{30}\right)^{\frac{3}{2}}\left(\frac{d_\alpha}{1.27}\right)^{-1}\left(\frac{\Omega_{\rm DM}h^2}{0.12}\right)^{-1}\ ,\\
\sin^2(2\theta)^{\rm ST2}_{\rm old} &= 1.15\times 10^{-8}\left(\frac{m_s}{\rm keV}\right)^{-2}\left(\frac{g_*}{30}\right)^{\frac{3}{2}}\left(\frac{d_\alpha}{1.27}\right)^{-1}\left(\frac{\Omega_{\rm DM}h^2}{0.12}\right)^{-1}\ ,\\
\sin^2(2\theta)^{\rm LRT}_{\rm old} &= 1\times 10^{-3}\left(\frac{m_s}{\rm keV}\right)^{-1}\left(\frac{d_\alpha}{1.13}\right)^{-1}\left(\frac{\Omega_{\rm DM}h^2}{0.12}\right)^{-1}\ .
\end{aligned} \tag{2.42}$$

The way in which f_{ν_s} approaches f_{ν_α} with increasing mixing angle is quantified by the solution to Eq. (2.38) which we call “non-linear" $f_{\nu_s-{\rm nl}}$ [140],

$$f_{\nu_s-{\rm nl}}(\epsilon,T) = \left(1-e^{-K(\epsilon,T)}\right) f_{\nu_\alpha} = \left[1-\exp\left(-\frac{f_{\nu_s-{\rm lin}}(\epsilon,T)}{f_{\nu_\alpha}(\epsilon)}\right)\right] f_{\nu_\alpha}(\epsilon)\ . \tag{2.43}$$

Here, $K(\epsilon,T)$ is

$$K(\epsilon,T) = \int_T^\infty dT\,\left(\frac{\Gamma_s(\epsilon,T)}{HT}\right)_\epsilon = \frac{f_{\nu_s-{\rm lin}}(\epsilon,T)}{f_{\nu_\alpha}(\epsilon)}\ , \tag{2.44}$$

for all the cosmologies we consider except LRT, for which the upper limit of integration is $T_{\rm RH}$ (see below). Notice that the integral in Eq. (2.44) is performed while keeping ϵ constant.

We assume that there are no sterile neutrinos present before non-resonant production takes place. Eq. (2.43) can be easily verified to be the solution to Eq. (2.38) by substitution. Our previous solution is readily recovered Eq. (2.43) as $f_{\nu_s-\mathrm{lin}}$ becomes much smaller than f_{ν_α} and we then keep only the first non-trivial term in the exponential.

Eq. (2.44) corresponds to Eq. (2.15), except there we approximated the lower limit of integration with $T = 0$. This is justified as the temperatures of interest in Eq. (2.43), the lower limits of integration in Eq. (2.44), are much lower than the temperature T_{max} at which the sterile neutrino production rate $(\partial f_{\nu_s}/\partial T)_\epsilon$ (neglecting f_{ν_s} in the right hand side of Eq. (2.38)) has a sharp maximum. For the STD cosmology, T_{max} is

$$T_{\mathrm{max}}^{\mathrm{STD}} = 145\ \mathrm{MeV}\left(\frac{m_s}{\mathrm{keV}}\right)^{\frac{1}{3}}\epsilon^{-\frac{1}{3}}\ , \tag{2.45}$$

and it is similar in the K, ST1 and ST2 cosmologies (see Eqs. (2.13), (2.14), (4.2) and (4.3)). This is a good approximation for the STD, ST1, ST2 and K cosmologies. In the LRT model, all of the sterile neutrino production is assumed to occur only during the late standard cosmology phase, at $T < T_{\mathrm{RH}}$ below the reheating temperature. Thus, the upper limit of integration in Eq. (2.44) becomes T_{RH}. As the maximum of the production happens very close to T_{RH}, the lower limit of integration can again be taken to be $T = 0$. This is the reason why the $f_{\nu_s-\mathrm{lin}}$ in Eq. (2.41) are function of ϵ only (and not T). Therefore, from Eq. (2.43) we see that $f_{\nu_s-\mathrm{nl}}$ are also functions only of ϵ.

Notice that $f_{\nu_s-\mathrm{nl}}$ in Eq. (2.43) approaches the active neutrino distribution as the linear solution $f_{\nu_s-\mathrm{lin}}$ grows larger than f_{ν_α}. This $f_{\nu_s-\mathrm{lin}}$ is a non-physical solution of the Boltzmann equation due to not taking into account f_{ν_s} on the right hand side.

As we will now show, the function $f_{\nu_s-\mathrm{nl}}$ departs significantly from the linear solution $f_{\nu_s-\mathrm{lin}}$ for mixing angles that are forbidden by the DM density condition $\Omega_s < \Omega_{\mathrm{DM}}$ and by the upper limit $N_{\mathrm{eff}} < 3.4$ on the effective number of relativistic active neutrino species present during BBN. As these regions are already forbidden, the resulting limits are unaffected by thermalization considerations.

In order to derive all limits that depend on the sterile neutrino number density n_{ν_s}, one needs to integrate $f_{\nu_s-\mathrm{nl}}$ over momenta to obtain n_{ν_s}. Following our previous notation we will denote the integration result as "non-linear" number density $n_{\nu_s-\mathrm{nl}}$, and the number densities we presented before in section 2.3 as "linear" $n_{\nu_s-\mathrm{lin}}$. The integration needs to be performed numerically, unless the ratio $(f_{\nu_s-\mathrm{lin}}/f_{\nu_\alpha})$ is a constant independent of ϵ. This is the case for the STD and ST2 cosmologies, where

$$\left(\frac{n_{\nu_s-\mathrm{lin}}}{n_{\nu_\alpha}}\right) = \left(\frac{f_{\nu_s-\mathrm{lin}}}{f_{\nu_\alpha}}\right) \tag{2.46}$$

and we can obtain the exact solution for $n_{\nu_s-\mathrm{nl}}$,

$$\left(\frac{n_{\nu_s-\mathrm{nl}}}{n_{\nu_\alpha}}\right) = 1 - e^{-(n_{\nu_s-\mathrm{lin}}/n_{\nu_\alpha})} \ . \tag{2.47}$$

Following our previous analysis, we will proceed with an analytic treatment. We are going to find approximate analytic solutions for $n_{\nu_s-\mathrm{nl}}$ for the other cosmologies we consider in which Eq. (2.46) does not hold, because the ratio $(f_{\nu_s-\mathrm{lin}}/f_{\nu_\alpha})$ depends on ϵ. The exact solution would require integration over momentum of an exponential function of ϵ. Since the dependence of the $(f_{\nu_s-\mathrm{lin}}/f_{\nu_\alpha})$ ratio on ϵ is weak, our approximation is justified.

With the DM abundance $\Omega_{\mathrm{DM}}h^2 = 0.12$, a fully thermalized sterile neutrino, with the relic number density of an active neutrino species, would constitute all of the DM if its mass is $m_s = 11.5$ eV. Thus, the DM limit $\Omega_s < \Omega_{\mathrm{DM}}$ does not restrict sterile neutrinos with $m_s < 11.5$ eV, since the number density of sterile neutrinos is at most equal to that of one active neutrino species. Above and close to $m_s = 11.5$ eV, taking into account the non-linear solution $f_{\nu_s-\mathrm{nl}}$ modifies the DM density limit with respect to the results of section 2.3.

In order to find an approximate analytic solution for $n_{\nu_s-\mathrm{nl}}$, let us start by defining a pre-factor C such that Eq. (4.10) for the sterile neutrino relic number density is

$$n_{\nu_s-\mathrm{lin}} = C \sin^2 2\theta \tag{2.48}$$

(i.e. C includes all the factors independent of the active-sterile mixing angle). Then the non-linear solution n_{ν_s-nl} for the number density satisfies

$$\rho_{\mathrm{DM}} = \frac{m_s \; n_{\nu_s-nl}}{\Omega_s/\Omega_{\mathrm{DM}}} = 11.5 \text{ eV } n_{\nu_\alpha} \ . \tag{2.49}$$

We denoted the DM density limit obtained using $n_{\nu_s-\mathrm{lin}}$, as in section 2.3, as $(\sin^2 2\theta)_{\mathrm{old}}$ that is a function of m_s given in Eq. (2.42). Thus, we can now state Eq. (4.25) for the DM fraction in sterile neutrinos for the K and ST2 cosmologies (or specifically Eqs. (4.26) and (4.27)) and Eq. (4.28) for the same fraction for the LRT model, setting these fractions to 1, as

$$1 = \frac{n_{\nu_s-\text{lin}} m_s}{\rho_{\text{DM}}\ (\Omega_s/\Omega_{\text{DM}})} = \frac{C(\sin^2 2\theta)_{\text{old}} m_s}{\rho_{\text{DM}}\ (\Omega_s/\Omega_{\text{DM}})}\ . \tag{2.50}$$

Using Eqs. (2.48), (2.49) and (2.50) we can relate n_{ν_s-nl} with the old DM limit $(\sin^2 2\theta)_{\text{old}}$,

$$\frac{C(\sin^2 2\theta)_{\text{old}}}{n_{\nu_\alpha}} = \frac{(\Omega_s/\Omega_{\text{DM}})\ \rho_{\text{DM}}}{m_s n_{\nu_\alpha}} = \frac{(\Omega_s/\Omega_{\text{DM}})\ 11.5\ \text{eV}}{m_s} = \frac{n_{\nu_s-nl}}{n_{\nu_\alpha}}\ . \tag{2.51}$$

This allows to define $(\sin^2 2\theta)_{\text{new}}$ such that the ratio $(n_{\nu_s-\text{nl}}/n_{\nu_\alpha})$ in Eq. (2.47) satisfies Eq. (2.51) when $(\sin^2 2\theta)_{\text{new}}$ is used in $n_{\nu_s-\text{lin}}$ in the exponent in the same equation, so that $(n_{\nu_s-\text{nl}}/n_{\nu_\alpha}) = (\Omega_s/\Omega_{\text{DM}})\ 11.5\ \text{eV}/m_s$. Hence,

$$\frac{(\Omega_s/\Omega_{\text{DM}})\ 11.5\ \text{eV}}{m_s} = 1 - \exp\left(-\frac{C(\sin^2 2\theta)_{\text{new}}}{n_{\nu_\alpha}}\right)\ . \tag{2.52}$$

Replacing here n_{ν_α} by $C(\sin^2 2\theta)_{\text{old}} m_s/(\Omega_s/\Omega_{\text{DM}})\ 11.5$ eV using Eq. (2.51), Eq. (2.52) can be rearranged to give the new mixing angle for the DM density limit (plotted in the figures) in terms of the old mixing angle (see Eqs. (4.29) to (4.32))

$$(\sin^2 2\theta)_{\text{new}} = (\sin^2 2\theta)_{\text{old}}\ \frac{m_s}{(\Omega_s/\Omega_{\text{DM}})\ 11.5\ \text{eV}}\ \ln\left[\frac{m_s}{m_s - (\Omega_s/\Omega_{\text{DM}})\ 11.5\ \text{eV}}\right]\ . \tag{2.53}$$

Taking $(\Omega_s/\Omega_{\text{DM}}) = 1$ this is the boundary of the dark gray regions where $\Omega_s > \Omega_{\text{DM}}$ shown in Fig. 2.4 and Fig. 2.3. Except in a region close to or below $m_s = 11.5$ eV, which is rejected by the (cyan) N_{eff} BBN limit, the present DM density limits are the same as those from section 2.3. Thus the allowed regions have not changed.

2.4.2 Thermalization limits

The production of sterile neutrinos saturates when they thermalize, when $f_{\nu_s} = f_{\nu_\alpha}$, and thus the right hand side of the Boltzmann equation Eq. (2.38) is equal to zero. In Fig. 2.3, the region of thermalization where $\Gamma/H|_{T_{\max}} \geq 1$ is demarcated with a solid blue line at its lower boundary. When the maximum production rate $\Gamma(T_{\max})$ stays roughly equal to or larger than the Hubble parameter for a significant period of time, a substantial amount of sterile neutrinos are produced and the population is nearly or fully thermalized.

To compute the production rates and momentum distributions we use as the characteristic momentum $\epsilon = \langle\epsilon\rangle$. $\langle\epsilon\rangle$ is the average value of E/T for each cosmology (see Eqs. (2.32) and (2.33))

$$\langle\epsilon\rangle = \begin{cases} 3.15, & \text{STD} \\ 3.47, & \text{K} \\ 2.89, & \text{ST1} \\ 3.15, & \text{ST2} \\ 4.11, & \text{LRT} \end{cases} \tag{2.54}$$

In contrast to section 2.3, except for LRT we use two values of the effective number of degrees of freedom contributing to the radiation density in H, $g_* = 10.75$ for $m_s < 11.5$ eV and $g_* = 30$ for $m_s > 11.5$ eV. This choice allows to better approximate the evolution of g_* with temperature [143, 144, 145]. We have chosen $m_s = 11.5$ eV as the mass where g_* changes, because for this mass $T_{\rm max} \simeq 20$ MeV and this is the temperature above which g_* starts increasing from its value of 10.75. In section (2.3) we had adopted for simplicity $g_* = 30$ throughout the entire mass range, except for the $N_{\rm eff}$ BBN limit, which is particularly relevant for light sterile neutrinos, and the LRT cosmology, for which we used 10.75. Here we instead adopt $g_* = 10.75$ for all our calculations with $m_s < 11.5$ eV as this value is more appropriate to the sterile neutrino production and thermalization at the eV scale, specifically in the regions where possible LSND, MiniBooNE, DANSS and NEOS sterile neutrino detection signals have been suggested. Our choice of using two distinct values of g_* results in an artificial discontinuity[6] at $m_s = 11.5$ eV in all the limits in Fig. 2.3. In the LRT cosmology, production happens only at $T < 5$ MeV, for which $g_* = 10.75$, for all sterile neutrinos. Thus there are no discontinuities at $m_s = 11.5$ eV in the BBN $N_{\rm eff}$ and thermalization (cyan, blue and black) limits in Fig. 2.4.

Notice that all cosmologies go into the standard cosmology, thus all limits become those standard, when $T_{\rm max} < T_{\rm tr} = 5$ MeV, i.e. for $m_s < 0.1$ eV. Given our approximations of considering a sharp transition of all cosmologies into the standard one at $T_{\rm tr}$, and assuming

[6]Had we instead considered the true value of g_* that is a continuous function of temperature, such discontinuity would be absent.

the sterile neutrino production happens at $T_{\max}$, this results in a discontinuity at $m_s \simeq 0.1$ eV in the limits in in Fig. 2.4 and 2.3, which had not been included in section 2.3 (as it affects a very small portion of the whole mass range we considered). In a more careful treatment, the limits would smoothly transition from the non-standard to the standard ones.

Solving for $\sin^2 2\theta$ from the condition $\Gamma/H|_{T_{\max}} = 1$ we obtain the following thermalization limits (the solid thick blue lines in Fig. 2.3),

$$\text{for STD:} \qquad (\sin^2 2\theta)_{\rm th} = 4.86 \times 10^{-3} \left(\frac{d_\alpha}{1.27}\right)^{-1} \left(\frac{m_s}{\rm eV}\right)^{-1} \left(\frac{g_*}{10.75}\right)^{\frac{1}{2}} , \tag{2.55}$$

$$\text{for K:} \qquad (\sin^2 2\theta)_{\rm th} = 1.52 \times 10^{-2} \epsilon^{-\frac{1}{3}} \left(\frac{d_\alpha}{1.27}\right)^{-1} \left(\frac{m_s}{\rm eV}\right)^{-\frac{2}{3}} \left(\frac{g_*}{10.75}\right)^{\frac{1}{2}} , \tag{2.56}$$

$$\text{for ST1:} \qquad (\sin^2 2\theta)_{\rm th} = 1.38 \times 10^{3} \epsilon^{0.27} \left(\frac{d_\alpha}{1.27}\right)^{-1} \left(\frac{m_s}{\rm eV}\right)^{-1.27} \left(\frac{g_*}{10.75}\right)^{\frac{1}{2}} , \tag{2.57}$$

$$\text{and for ST2:} \qquad (\sin^2 2\theta)_{\rm th} = 1.56 \times 10^{-4} \left(\frac{d_\alpha}{1.27}\right)^{-1} \left(\frac{m_s}{\rm eV}\right)^{-1} \left(\frac{g_*}{10.75}\right)^{\frac{1}{2}} . \tag{2.58}$$

We have confirmed that these limits (derived from $\Gamma/H|_{T_{\max}} = 1$) practically coincide with those corresponding to $f_{\nu_s-\rm lin} = f_{\nu_\alpha}$ for the mentioned cosmologies, which we thus do not display separately in Fig. 2.3.

For the LRT model, considering that the maximum production rate is at $T_{\rm RH} = 5$ MeV, we could be tempted to use $\Gamma/H|_{T_{\rm RH}} = 1$ as the condition for thermalization. However, when employing this condition throughout the whole range of integration in T, from 0 to $T_{\rm RH}$, to obtain $K(\epsilon, T)$, the integrand is smaller than 1. Thus, this is not a good condition of thermalization for this model. Since the thermalization condition based on Γ/H coincides with the condition $f_{\nu_s-\rm lin} = f_{\nu_\alpha}$ in all the other models we consider, we thus adopt $f_{\nu_s-\rm lin} = f_{\nu_\alpha}$ as the condition for thermalization in the LRT model. This condition translates into

$$(\sin^2 2\theta)_{\rm th} = 2.78 \times 10^{-1}\, \epsilon^{-1} , \tag{2.59}$$

which is shown with the thick blue line in Fig. 2.4.

Notice that we have considered the condition $\Gamma/H > 1$ for chemical equilibrium of sterile neutrinos, since the rate Γ we used is the production rate. Kinetic equilibrium happens at larger mixing angles than chemical equilibrium. The reason for this is that the sterile neutrino scattering rate contains an extra $\sin^2\theta$ factor over the production rate. Thus, sterile neutrinos that are not in chemical equilibrium (i.e. for which the production rate is $\Gamma < H$) are also not in kinetic equilibrium, they are decoupled from the thermal bath.

On the thick blue lines in the figures, $f_{\nu_s-\mathrm{nl}} = (1-e^{-1})f_{\nu_\alpha} = 0.63 f_{\nu_\alpha}$. In Fig. 2.4 and Fig. 2.3 we also display with a solid black line where $f_{\nu_s-\mathrm{lin}} = 3 f_{\nu_\alpha}$, and thus $f_{\nu_s-\mathrm{nl}} = (1-e^{-3})f_{\nu_\alpha} = 0.95 f_{\nu_\alpha}$, where nearly full thermalization occurs. Above this black line, the sterile neutrino momentum distribution rapidly becomes $f_{\nu_s} = f_{\nu_\alpha}$ with increased mixing (i.e. the right hand side of the Boltzmann equation Eq. (2.38) goes to zero). The equations of the thick black line in the figures are:

$$\text{for STD:} \qquad \sin^2 2\theta = 1.73\times 10^{-2}\left(\frac{d_\alpha}{1.27}\right)^{-1}\left(\frac{m_s}{\mathrm{eV}}\right)^{-1}\left(\frac{g_*}{10.75}\right)^{\frac{1}{2}}, \tag{2.60}$$

$$\text{for K:} \qquad \sin^2 2\theta = 4.29\times 10^{-2}\epsilon^{-\frac{1}{3}}\left(\frac{d_\alpha}{1.27}\right)^{-1}\left(\frac{m_s}{\mathrm{eV}}\right)^{-\frac{2}{3}}\left(\frac{g_*}{10.75}\right)^{\frac{1}{2}}, \tag{2.61}$$

$$\text{for ST1:} \qquad \sin^2 2\theta = 5.27\times 10^{3}\epsilon^{0.27}\left(\frac{d_\alpha}{1.27}\right)^{-1}\left(\frac{m_s}{\mathrm{eV}}\right)^{-1.27}\left(\frac{g_*}{10.75}\right)^{\frac{1}{2}}, \tag{2.62}$$

$$\text{for ST2:} \qquad \sin^2 2\theta = 5.52\times 10^{-4}\left(\frac{d_\alpha}{1.27}\right)^{-1}\left(\frac{m_s}{\mathrm{eV}}\right)^{-1}\left(\frac{g_*}{10.75}\right)^{\frac{1}{2}}, \tag{2.63}$$

$$\text{and for LRT:} \qquad \sin^2 2\theta = 8.34\times 10^{-1}\epsilon^{-1}\,. \tag{2.64}$$

Eqs. (2.46) and (2.47) emply that $f_{\nu_s-\mathrm{lin}} = 3 f_{\nu_\alpha}$ corresponds to $n_{\nu_s-\mathrm{nl}}/n_{\nu_\alpha} \simeq 0.95$, which leads to $\rho_s = \rho_{\mathrm{DM}}$ for $m_s = 11.5$ eV. In fact, in the figures the thick blue line intersects the DM density limit near $m_s = 11.5$ eV, as expected.

2.5 Limits and potential signals for Non-resonant Production

Here we discuss constraints, regions of interest in the mass-mixing plane and potential signals for sterile neutrinos produced via non-resonant active-sterile oscillations in different pre-BBN cosmologies. The results are shown in Figs. 2.3 and 2.4. In the figures we assume that the sterile neutrino only mixes with ν_e.

The most stringent cosmological and astrophysical limits on sterile neutrinos come from Lyman-α forest and X-ray observations for the 1 to 10 keV mass range and BBN for $m_s < 100$

eV. We also discuss the 3.5 keV X-ray line as well as upcoming laboratory experiments such as KATRIN/TRISTAN [17] and HUNTER [19] for the 1 to 10 keV mass range, reactor and accelerator neutrino experiments for $m_s < 10$ eV and also the $0\nu\beta\beta$ searches.

2.5.1 Lyman-α forest WDM and HDM limits

Sterile neutrinos of $m_s = \mathcal{O}(\text{keV})$ produced non-resonantly constitute a warm DM (WDM) candidate. The free-streaming of DM particles suppresses structure formation below the free-streaming scale (see e.g. Ref. [131])

$$\lambda_{\rm fs} = a(t_U)\int_{t_i}^{t_U} dt' \frac{v(t')}{a(t')} \simeq 1 \text{ Mpc}\left(\frac{\text{keV}}{m_s}\right)\frac{\langle p_{\nu_s}\rangle}{\langle p_{\nu_\alpha}\rangle} = 1 \text{ Mpc}\left(\frac{\langle\epsilon\rangle}{3.15}\right)\left(\frac{\text{keV}}{m_s}\right)\frac{T_{\nu_s}}{T_{\nu,0}} \ , \qquad (2.65)$$

where $v(t)$ is a typical DM velocity, t_U is the present lifetime of the Universe, t_i is some initial very early time whose exact value is not important, $a(t)$ is the scale factor of the Universe, $\langle p_{\nu_s}\rangle$ and $\langle p_{\nu_\alpha}\rangle$ are the average absolute values of the sterile and active neutrino momentum and T_{ν_s} and $T_{\nu,0}$ are the present temperatures of the sterile and active neutrinos, respectively.

Observations of the Lyman-α forest[7] in the spectra of distant quasars constrain the power spectrum on $\sim 0.1 - 1$ Mpc scales [10], which from Eq. (2.65) constrains WDM and thus sterile neutrinos with $m_s = \mathcal{O}(\text{keV})$.

The Lyman-α limits are usually given in terms of the mass $m_{\rm therm}$ of a fermion that was in thermal equilibrium at some point in the history of the Universe, and thus has a Fermi-Dirac spectrum, and thus has $\langle\epsilon\rangle = 3.15$, and a temperature $T_{\rm therm}$ that depends on when the fermion decoupled from the radiation bath. Hence, the relic density $\Omega_{\rm therm}$ of this thermal fermion, which depends on its temperature and mass, and its mass are free independent parameters. Sterile neutrinos produced via active-sterile oscillations do not have a thermal equilibrium spectrum, and could have $\langle\epsilon\rangle \neq 3.15$ (see Eqs. (2.32) and (2.33)). Sterile neutrinos may also have a temperature T_{ν_s} smaller than the active neutrino temperature T_ν. In fact, for $m_s = \mathcal{O}(\text{keV})$ the temperature of maximum production $T_{\rm max} >$

[7] An alternative approach is to use DM halo counts, whose number and formation are also related to free-streaming scales (see the discussion in Ref. [131]).

100 MeV (except in the LRT models) is much higher than the active neutrino decoupling temperature $T \simeq 3$ MeV, resulting in $T_{\nu_s} < T_\nu$.

Following Ref. [182], we equate the free-streaming scales of thermal WDM and sterile neutrinos

$$\frac{\langle \epsilon \rangle \; T_{\nu_s}}{m_s} = \frac{3.15 \; T_{\rm therm}}{m_{\rm therm}} \;, \tag{2.66}$$

as well as their energy densities, $\Omega_{\rm therm} = \Omega_{\nu_s} = f_{\rm s,DM}\, \Omega_{DM}$. This allows to identify the sterile neutrino mass that would result in the same free-streaming as a thermal WDM fermion with mass $m_{\rm therm}$

$$m_s = 4.46 \text{ keV} \left(\frac{\langle \epsilon \rangle}{3.15}\right) \left(\frac{m_{\rm therm}}{\rm keV}\right)^{\frac{4}{3}} \left(\frac{T_{\nu_s}}{T_{\nu_\alpha}}\right) \left(\frac{0.12}{f_{\rm s,DM}\; \Omega_{DM} \; h^2}\right)^{\frac{1}{3}} \;, \tag{2.67}$$

where $T_{\nu_s}/T_{\nu_\alpha} = (10.75/g_*)^{1/3}$. For our figures we use $g_* = 30$ except for the LRT cosmology for which we take $g_* = 15$.

The Lyman-α bounds of Ref. [10] on $m_{\rm therm}$ can now be translated into bounds on m_s through Eq. (2.67). We use the 2-σ bounds from the right panel of Fig. 6 of Ref. [10] coming from SDSS, XQ and HR data. These limits impose that sterile neutrinos do not account for more than $\sim 8\%$ of the DM density for $m_s \lesssim 1$ keV. Lower m_s values yield larger free-streaming lengths, which for $\lambda_{\rm fs} \gtrsim 1$ Mpc scales will not significantly alter the Lyman-α bounds. Hence, in Figs. 2.3 and 2.4 we extend the saturated bound of Ref. [10] to lighter sterile neutrinos that would constitute Hot DM (HDM), until it is superseded by the BBN bound in Eq. (2.71).

Due to thermalization, these bounds will move to higher mixing angles, changing the limits derived from the 2-σ warm DM limit from SDSS+XQ+HR in Fig. 6 of Ref. [10], which has an asymptote of $(\Omega_s/\Omega_{\rm DM}) \lesssim 0.08$ for small sterile neutrino masses. This limit is given in terms of $m_{\rm therm}$ which can be converted to limits on m_s using [182] $m_s = 4.46\,\text{keV}\,(\langle\epsilon\rangle/3.15)\,(m_{\rm therm}/\text{keV})^{\frac{4}{3}}\,(T_{\nu_s}/T_{\nu_\alpha})\,(0.12/(\Omega_s\; h^2))^{\frac{1}{3}}$. We apply Eq. (2.53) with $(\Omega_s/\Omega_{\rm DM}) = 0.08$ replacing $(\sin^2 2\theta)_{\rm old}$ to obtain the present Lyman-α bounds.

2.5.2 BBN limit on the effective number of neutrino species

The impact on BBN of an increased expansion rate of the Universe yields an upper limit on $N_{\rm eff}$, the effective number of relativistic active neutrino species present during BBN. Assuming that only sterile neutrinos and SM active neutrinos contribute to $N_{\rm eff}$,

$$N_{\rm eff} = 3.045 + \left(\frac{\rho_{\nu_s}}{\rho_{\nu_\alpha}}\right) , \tag{2.68}$$

where 3.045 is the contribution of the SM active neutrinos alone [183, 184]. All the sterile neutrinos we consider are relativistic during BBN, thus $(\rho_{\nu_s}/\rho_{\nu_\alpha})$ is the ratio during BBN of the relativistic energy densities of the sterile neutrino, $\rho_{\nu_s} = \langle\epsilon\rangle T n_{\nu_s}$ with $\langle\epsilon\rangle$ given in Eq. (2.32), and one active neutrino species ν_α, $\rho_{\nu_\alpha} = 3.15 T n_{\nu_\alpha}$[8]. Hence,

$$\Delta N_{\rm eff} = N_{\rm eff} - 3.045 \simeq \left(\frac{\langle\epsilon\rangle}{3.15}\right)\left(\frac{10.75}{g_*}\right)^{1/3}\left(\frac{n_{\nu_s}}{n_{\nu_\alpha}}\right) . \tag{2.69}$$

Here, the ratio n_{ν_s}/n_{ν_α} in each cosmology (see Sec. 2.3.4 and Appendix 4.1.3 for sterile neutrinos produced non-resonantly) is the same during BBN and at present, since both the number densities of sterile and of active neutrinos just redshift for $T < 1$ MeV (and BBN starts at about $T = 0.8$ MeV). Using Eq. (2.19), the present number density of one active neutrino is

$$n_{\nu_\alpha} \simeq 112 \text{ cm}^{-3} \left(\frac{T_{\nu,0}}{1.95 \text{ K}}\right)^3 . \tag{2.70}$$

The BBN upper bound of $N_{\rm eff} < 3.4$ at 95% confidence level [9] through the Eq. (2.69) rejects the cyan region in mass-mixing labelled "BBN" in Figs. 2.3 and 2.4. This upper limit is similar to the Planck 2018 limit [46] derived from cosmic microwave background radiation (CMB) data on $N_{\rm eff}$.

Alternatively to obtaining the limit from Eq. (2.69), we can use the same equation to derive a limit on the present fraction of the DM consisting of sterile neutrinos. The present value of the number density $n_{\nu_s 0}$ determines the present relic density $\rho_{s,0} = n_{\nu_s 0} m_s$ and thus

[8] We note that only for neutrinos much heavier than those we consider here sterile neutrinos could decay before BBN, thus increasing $N_{\rm eff}$ due to their decay products (heavy sterile neutrinos have been recently suggested as a solution to the observed tension between local and early Universe measurements of the Hubble constant [185]).

the present fraction of the DM in sterile neutrinos corresponding to a particular $\Delta N_{\rm eff}$:

$$f_{s,\rm DM} = \frac{n_{\nu_s 0} m_s}{\rho_{\rm DM}} = 35.5 \left(\frac{\langle\epsilon\rangle}{3.15}\right)^{-1} \left(\frac{m_s}{\rm keV}\right) \left(\frac{T_{\nu,0}}{1.95\ \rm K}\right)^{3} \left(\frac{g_*}{10.75}\right)^{\frac{1}{3}} \left(\frac{\Omega_{\rm DM} h^2}{0.1198}\right)^{-1} \left(\frac{\Delta N_{\rm eff}}{0.4}\right) , \tag{2.71}$$

where g_* is the number of entropy degrees of freedom when ν_s are produced. Using Eq. (4.19) for $f_{s,\rm DM}$, or the equation corresponding to a particular cosmological model, $\Delta N_{\rm eff} < 0.4$ imposes an upper limit on the fraction of the DM consisting of sterile neutrinos.

In addition to the BBN $N_{\rm eff}$ bounds, we apply for $m_s \lesssim 10$ eV the combined CMB $\Delta N_{\rm eff}$ and $m_{\rm eff}$ [46], for sterile neutrinos which are respectively relativistic and becoming non-relativistic close recombination. The current 95% Planck 2018 limits in Eq. (70a) of Ref. [46] are[9]

$$N_{\rm eff} < 3.29, \qquad m_{\rm eff} < 0.65 \text{ eV} . \tag{2.72}$$

Using the definitions $N_{\rm eff} = 3.04 + (\rho_{\nu_s}/\rho_{\nu_\alpha})$ and $m_{\rm eff} = n_{\nu_s} m_s / n_{\nu_a}$ [140, 46] with $\rho_{\nu_s}/\rho_{\nu_\alpha} = (\langle\epsilon\rangle\, n_{\nu_s-\rm nl})/(3.15\, n_{\nu_a})$ and $n_{\nu_s} = n_{\nu_s-\rm nl}$, and replacing in Eq (2.47) the upper limits on $n_{\nu_s-\rm nl}$ derived from the $N_{\rm eff}$ and the $m_{\rm eff}$ limits we get respectively

$$\frac{n_{\nu_s-\rm lin}}{n_{\nu_\alpha}} < \ln\left(\frac{1}{1-0.25(3.15/\langle\epsilon\rangle)}\right) \simeq 0.29, \qquad \frac{n_{\nu_s-\rm lin}}{n_{\nu_a}} < -\ln\left[1-\frac{0.65\text{ eV}}{m_s}\right] . \tag{2.73}$$

Using now Eqs. (2.23), (2.25), (4.12), (4.14), and (4.16) for $n_{\nu_s-\rm lin}$, we obtain the upper limits on the mixing angle shown with red solid lines in the upper left hand corners of Figs. 2.4 and 2.3 for $m_s < 10$ eV. The $m_{\rm eff}$ bound becomes more restrictive than the $\Delta N_{\rm eff}$ bound for $m_s > 3$ eV, which causes the change in slope of the red lines. As it is clear from the figures, these CMB limits are very close to the BBN $N_{\rm eff}$ (cyan) limits, thus do not change significantly the allowed parameter regions.

2.5.3 Distortions of the CMB spectrum

Photons produced in the decays of sterile neutrinos before recombination, i.e. $\tau < t_{\rm rec} \simeq 1.2 \times 10^{13}$ sec, can distort the CMB spectrum [187, 188] if they are produced after the

[9] While these bounds were formulated for thermally produced sterile neutrinos, they are expected to be reasonably accurate for other models [186]. We thus apply them to all cosmologies.

thermalization time $t_{\rm th} \simeq 10^6$ sec (see e.g. the discussion in Ref. [176]). Lifetimes of Majorana sterile neutrinos[10] equal to the lifetime of the Universe, $t_U = 4.36 \times 10^{17}$ sec, to $t_{\rm rec}$ and to $t_{\rm th}$ are indicated with red long-dashed straight lines in Figs. 2.3 and 2.4. The COBE FIRAS limits [16] on distortions of the CMB spectrum reject lifetimes $t_{\rm rec} > \tau > t_{\rm th}$ (region diagonally hatched in red in Figs. 2.3 and 2.4 labeled "CMB").

Non-thermal photons produced before the thermalization time $t_{\rm th}$ are rapidly incorporated into the Planck spectrum through processes that change the number of photons, such as double Compton scattering ($\gamma e \to \gamma\gamma e$), which are no longer effective after $t_{\rm th}$. For $t_{\rm th} < \tau_s < 10^9$ sec, photon number preserving processes, such as elastic Compton scattering, are still efficient. These processes thermalize the photons into a Bose-Einstein spectrum with a non-zero photon chemical potential μ. If the initial spectrum has fewer photons than a black body of the same total energy the chemical potential is positive and $\mu > 0$ (if instead it has more photons, $\mu < 0$). For $|\mu| \ll 1$, the only values of μ allowed by the COBE satellite limit $|\mu| < 0.9 \times 10^{-4}$ at the 95% CL [16], the energy released into photons in the decay is [187]

$$\frac{\Delta\rho_\gamma}{\rho_\gamma} \simeq 0.714\mu \; . \tag{2.74}$$

For longer lifetimes, the photon number preserving processes can no longer establish a Bose-Einstein spectrum. Thus, for 10^9 sec $< \tau_s < t_{\rm rec}$ the energy released into photons by the decays is not thermalized but still heats up the electrons. Through inverse-Compton scattering this produces a distorted spectrum characterized by a parameter y. The COBE bound on this parameter is $|y| < 1.5 \times 10^{-5}$ [16] and, for $|y| \ll 1$, y is related to the energy released in non-thermal photons as [187]

$$\frac{\Delta\rho_\gamma}{\rho_\gamma} \simeq 4y \; . \tag{2.75}$$

Coincidentally, the upper limits on μ and y are such that in both cases, Eqs. (2.74) and (2.75), the upper limit on the fractional increase in the photon energy density due to the decay of the sterile neutrinos is 6×10^{-5}. Thus, assuming that the decays happen instantaneously at

[10] For Dirac neutrinos the lifetime must be multiplied by 2.

$t = \tau_s$, and noting that the energy of each photon produced in a decay is $m_s/2$, $\rho_\gamma = 2.7\, T\, n_\gamma$, the temperature-time relation is $T \simeq$ MeV $(t/\text{sec})^{1/2}$, we have

$$\frac{\Delta\rho_\gamma}{\rho_\gamma} = \frac{B\ (m_s/2)\, n_{\nu_s}}{2.7\ T\, n_\gamma} \simeq \frac{(B/2)\, m_s\, n_{\nu_s}}{2.7\,\text{MeV}\ n_\gamma} \left(\frac{\tau_s}{\text{sec}}\right)^{1/2} \simeq \frac{(B/2)\, f_{s,\text{DM}}\ \rho_{\text{DM}}}{2.7\,\text{MeV}\ n_\gamma} \left(\frac{\tau_s}{\text{sec}}\right)^{1/2} \lesssim 6 \times 10^{-5}\ . \tag{2.76}$$

Here B is the branching ratio for the radiative decay, so that $B\ n_{\nu_s}$ is the number of photons produced when the sterile neutrinos decay, the ratio (n_{ν_s}/n_γ) is the same for any $T < 1$ MeV, and at present the energy density in sterile neutrinos is $n_{\nu_s} m_s = f_{s,\text{DM}}\ \rho_{\text{DM}}$. In our case the branching ratio is $B = 0.78 \times 10^{-2}$, and at present $n_\gamma = 413/\text{cm}^3$ and $\rho_{\text{DM}} \simeq 1.25$ keV/cm^3, thus we get

$$f_{s,\text{DM}} \left(\frac{\tau_s}{t_{\text{rec}}}\right)^{1/2} \lesssim 4 \times 10^{-3}\ . \tag{2.77}$$

This mean that for $\tau = 10^6$ the limit is $f_{s,\text{DM}} < 12$. We can easily see in Figs. 2.3 and 2.4 that the values of the fraction $f_{s,\text{DM}}$ of the DM in sterile neutrinos are much larger than the upper limit in the whole lifetime range $t_{\text{rec}} > \tau > t_{\text{th}}$ where the limit applies.

2.5.4 SN1987A disfavored region

The energy loss due to sterile neutrinos produced in core collapse supernovae explosions disfavors [3] the region horizontally hatched in brown and labeled "SN" in Figs. 2.3 and 2.4. Due to the considerable uncertainty in the neutrino transport and flavor transformation within hot and dense nuclear matter [137], it is difficult to exclude this region entirely. Recent studies regarding sterile neutrinos mixing with ν_μ or ν_τ have been carried out in e.g. Ref. [189, 190].

2.5.5 X-ray observations and the 3.5 keV line

The most restrictive limits on sterile neutrinos with mass $m_s = 1 - 10$ keV come from astrophysical indirect detection searches of X-rays produced in their $\nu_s \to \nu_\alpha \gamma$ two-body decay[11] [11, 12, 13]. The rate of this decay mode is [191, 192]

$$\Gamma_\gamma = 1.38 \times 10^{-32}\ \mathrm{s}^{-1} \left(\frac{\sin^2(2\theta)}{10^{-10}}\right) \left(\frac{m_s}{\mathrm{keV}}\right)^5 . \tag{2.78}$$

Due to the rapid decrease of the decay rate with decreasing m_s, X-ray observations do not provide meaningful constraints for sterile neutrinos with $m_s < 1$ keV.

The model independent X-ray bounds found in the literature [11, 12, 13] assume that sterile neutrinos constitute the entirety of the DM. In order to translate the published limits into those that apply in our scenarios we take into account that the X-ray signal depends on the produced photon flux, thus the limits actually constrain the product $(\Omega_s/\Omega_{\rm DM})\sin^2 2\theta$ and not just $\sin^2 2\theta$. The present sterile neutrino fraction $f_{s,\rm DM} = (\Omega_s/\Omega_{\rm DM})$ of the DM is itself proportional to $\sin^2 2\theta$ (because of the dependence of n_{ν_s} in Eq. (4.10), and Sec. 2.3.4 and Appendix 4.1.3 on the mixing). Hence, the X-ray limits shown in Fig. 2.3 are related to the published model independent X-ray bounds through a simple rescaling.

From Eq. (4.25), DM fraction in sterile neutrinos can be written for non-resonant production as $f_{s,\rm DM} = \sin^2(2\theta)/\sin^2(2\theta)_{\rm DW,lim}$, thus the constraint on our models is the geometric mean of the published model independent limit and $\sin^2(2\theta)_{\rm DW,lim}$ (given in Eq. (2.36), Eq. (2.37) and Appendix 4.1.6 for the different cosmologies we consider).

The same rescaling applies to upper limits on the diffuse extragalactic background radiation (DEBRA) [14] on sterile neutrinos decaying after recombination, i.e. $\tau > t_{\rm rec}$ (the lower boundary of the DEBRA rejected region is indicated by a straight green line in Figs. 2.3 and (2.4)). X-ray limits coming from galaxies and galaxy clusters only apply to relatively recent times after these structures formed, thus they are superseded by the DEBRA limits which apply on the integrated flux of all decays that occur between $t_{\rm rec}$ and the present.

The 3.5 keV X-ray emission line signal reported in 2014 [4, 5], which remains a matter of lively debate (see e.g. [193, 194]), could be due to the decay of $m_s \simeq 7$ keV sterile neutrinos whose mixing should be $\sin^2 2\theta = 5 \times 10^{-11}$ if they constitute all of DM. The active-sterile mixing necessary for sterile neutrinos produced non-resonantly to reproduce the putative

[11] The branching ratio for the photon decay channel is subdominant, the dominant decay channel is $\nu_s \to 3\nu_\alpha$.

signal line shifts in the same way as the X-ray bounds just mentioned, and is indicated with a black star in Figs. (2.3) and (2.4). These figures show that in all the models we consider, except ST2, the signal would correspond to sterile neutrinos that constitute only a small fraction of the DM. Fig. 2.3 shows that in the ST2 model, the signal rejected by Lyman-α limits. Comparing the K, ST1 and LRT to the standard cosmology in Figs. 2.3 and (2.4), we see clearly that decreased production in cosmologies with faster expansion rates increases the mixing angle required to produce the signal. In the K cosmology the mixings necessary to produce the 3.5 keV signal is $\sin^2 2\theta = \mathcal{O}(10^{-9})$, and in the LRT and ST1 cosmologies it is $\sin^2 2\theta = \mathcal{O}(10^{-7})$, within the reach of the KATRIN experiment with its proposed TRISTAN upgrade [17] as well as the upcoming HUNTER experiment and its upgrades [19].

2.5.6 Laboratory experiments

For eV- and keV-mass sterile neutrinos, multiple laboratory experiments can probe and restrict sizable portions of the parameter space. Since these experiments directly probe the active-sterile mixing angle and mass by searching for active neutrino appearance and disappearance, the resulting bounds they set are independent of cosmology and require no further modification.

In the eV-mass range of sterile neutrinos mixing with ν_e, the limits are dominated by the Daya Bay [6], Bugey-3 [7] and PROSPECT [8] reactor and accelerator experiments, which combined reject the green regions labelled “R" in Figs. 2.3 and (2.4). Several anomalous results, consistent with a sterile neutrino of $m_s \sim$ eV mass contributing to active-sterile neutrino oscillations, have been reported from the short-baseline studies of ν_e appearance by the LSND [121] and MiniBooNE [122] experiments. These claims have been further bolstered recently with analysis of additional MiniBooNE data [20]. We show in Figs. 2.3 and (2.4) with a black densely hatched band denoted “MB" the parameter space allowed at the 4-σ level consistent with these excesses, reproduced from Fig. 4 of Ref. [20] (see discussions in Ref. [20] for details). We stress, however, that the anomalous ν_e appearance results discussed above are in strong tension with the ν_μ disappearance results from IceCube [195] and MINOS [196]. In the same sterile neutrino mass region, recent reactor neutrino results from the DANSS [21] and NEOS [22] experiments are also consistent with a sterile neutrino interpretation. A combined fit to their data [129, 23, 130] allows for a sterile neutrino with $m_s \simeq 1.14$ eV mass and $\sin^2 2\theta \simeq 0.04$ mixing with a ν_e active neutrino. The regions allowed at 3-σ level by the DANSS and NEOS data reproduced from Fig. 4 of Ref. [23] are indicated with black vertical elliptical contours in Figs. 2.3 and 2.4.

As we display in Fig. 2.3 and (2.4), the eV-mass parameter space relevant for anomalous observations in short-baseline and reactor experiments will be fully or at least partially tested by KATRIN [18] (whose reach is shown with a solid blue line labeled “KA") as well as PTOLEMY [24] (whose reach is shown with solid orange lines labeled “P" and “P2" for 10 mg-yr and 100 g-yr exposures, respectively). PTOLEMY is a tritium β-decay experiment aimed at detecting the cosmological relic neutrino background which is expected to start collecting data within few years. As shown in Fig. 2.3 and Fig. 2.4, the cosmological bounds in the ST1 and LRT cosmologies are significantly relaxed for eV-mass sterile neutrinos compared to those in the Std cosmology. Hence, the required parameter space for anomalous observations in short-baseline and reactor experiments is not rejected by cosmology.

In the keV mass-scale, the tritium decay experiment KATRIN [197, 198] will probe active-sterile mixing down to $\sin^2(2\theta) \leq 10^{-4}$ [17], shown with solid blue and denoted “KA” on Figs. 2.3 and 2.4. Its upgraded version, TRISTAN (denoted with a solid blue line and labelled “T” and “T2”, corresponding to a 1 year and 3 year data collecting period, respectively), is expected to reach sensitivities of $\sin^2(2\theta) \sim 10^{-8}$ within a 3 year run-time [17]. The upcoming cesium trap experiment HUNTER [19] is expected to probe even more further within the sterile neutrino parameter space. Here, the missing mass of the neutrino will be reconstructed from ^{131}Cs electron capture decays occurring in a magneto-optically trapped sample. The prototype version of the experiment is already under construction and will have two phases, whose sensitivity we display in Figs. 2.3 and (2.4) with magenta solid lines and labelled “H1A” and “H1B”, respectively. The upgrade version of Hunter, denoted by “HU”, is expected to be sensitive to mixings down to $\sin^2(2\theta) \sim 10^{-11}$. The above-mentioned experiments will be able to test the sterile neutrino origin of the 3.5 keV X-ray signal line.

In non-standard cosmologies that result in decreased sterile neutrino density, the required mixing angle to explain the signal increases, allowing for sterile neutrinos to appear more visible for laboratory studies (see e.g. LRT and ST1 in Figs. 2.3 and (2.4)).

If the sterile neutrinos are Majorana particles, they will mediate the neutrinoless double beta $0\nu\beta\beta$ decay. A sterile neutrino that mixes with the electron neutrino contributes $\langle m \rangle_s = m_s \sin^2(\theta) e^{i\beta_s}$ to the effective electron neutrino Majorana mass $\langle m \rangle$ that affects the half-life of $0\nu\beta\beta$ decay, where β_s denotes a Majorana CP-violating phase. Hence, using the present bound on the magnitude of $\langle m \rangle$, $|\langle m \rangle| < 0.165$ eV [15], the corresponding bound on the sterile neutrino mass and mixing angle is $m_s \sin^2(2\theta) < 0.660$ eV. This limit is shown in orange in Figs. 2.3 and (2.4), with the label "$0\nu\beta\beta$". We note that this bound is not completely robust. The contribution of the sterile neutrino might interfere with the contributions from the active ones, leading to a suppression in the effective Majorana mass and, therefore, avoiding the experimental bounds [199].

2.6 Resonant sterile neutrino production

2.6.1 Boltzmann equation

As in the case of non-resonant sterile neutrino production [67] (see section 2.3.1), for resonant production the time evolution of the momentum distribution function of sterile neutrinos $f_{\nu_s}(p,t)$ is given by the Boltzmann equation [142, 137, 140]

$$- HT \left(\frac{\partial f_{\nu_s}(E,T)}{\partial T} \right)_{E/T=\epsilon} \simeq \Gamma(E,T) f_{\nu_\alpha}(E,T) \ , \tag{2.79}$$

where $f_{\nu_\alpha}(p,t) = (e^{\epsilon-\xi}+1)^{-1}$ is the density function of active neutrinos, p is the magnitude of the neutrino momentum, $\epsilon = p/T$ is the dimensionless momentum, $\xi = \mu_{\nu_\alpha}/T$ is the T-scaled dimensionless chemical potential where μ_{ν_α} is the chemical potential of ν_α, $\Gamma(p,t)$ is the conversion rate of active to sterile neutrinos, the energy is $E \simeq p$, since all neutrinos of interest are relativistic at production, and derivative in the left-hand side of the equation is computed at constant ϵ. Eq. (2.79) is valid if $f_{\nu_s} \ll 1$ and $f_{\nu_s} \ll f_{\nu_\alpha}$.

The total rate Γ of active to sterile neutrino conversion is given by the probability $\langle P_m \rangle$

of an active-sterile flavor oscillation in matter (for mixing angle in matter θ_m) times the interaction rate

$$\Gamma_\alpha = d_\alpha G_F^2 \epsilon T^5, \tag{2.80}$$

of active neutrinos with the surrounding plasma [137]

$$\Gamma \;=\; \frac{1}{2}\langle P_m(\nu_\alpha \to \nu_s)\rangle \Gamma_\alpha \;\simeq\; \frac{1}{4}\sin^2(2\theta_m) d_\alpha G_F^2 \epsilon T^5 \;, \tag{2.81}$$

where $d_\alpha = 1.27$ for ν_e and $d_\alpha = 0.92$ for ν_μ, ν_τ. The mixing angle in matter θ_m is given by

$$\sin^2(2\theta_m) = \frac{\sin^2(2\theta)}{\sin^2(2\theta) + \Big[\cos(2\theta) - 2\epsilon T(V_D + V_T)/m_s^2\Big]^2} \;. \tag{2.82}$$

In the right hand side of Eq. (2.79) we have omitted the quantum damping factor $[1 - (\Gamma_\alpha \ell_m/2)^2]^{-1}$ where ℓ_m is the oscillation length in matter (see e.g. the discussion in Refs. [137, 200]). This term is typically negligible for the range of parameters relevant for our study, but could become significant at the resonance (because at resonance the neutrino oscillation length is maximal), as we discuss in Sec. 2.6.4.

In the denominator of Eq. (2.82) V_T is the thermal potential

$$V_T \;=\; -\,B\epsilon T^5 \;, \tag{2.83}$$

where B is a constant prefactor dependent on flavor (given below in parenthesis) and temperature range (given to the right of each line below)

$$B = \begin{cases} 10.88 \times 10^{-9}\ \mathrm{GeV}^{-4}\ (e); & 3.02 \times 10^{-9}\ \mathrm{GeV}^{-4}\ (\mu,\tau); \qquad\qquad T \lesssim 20\ \mathrm{MeV} \\ 10.88 \times 10^{-9}\ \mathrm{GeV}^{-4}\ (e,\mu); & 3.02 \times 10^{-9}\ \mathrm{GeV}^{-4}\ (\tau); \quad 20\ \mathrm{MeV} \lesssim T \lesssim 180\ \mathrm{MeV} \\ 10.88 \times 10^{-9}\ \mathrm{GeV}^{-4}\ (e,\mu,\tau); & \qquad\qquad\qquad\qquad\qquad\qquad T \gtrsim 180\ \mathrm{MeV} \end{cases} \tag{2.84}$$

The density potential V_D depends on the particle-antiparticle asymmetries in the background

$$V_D \;=\; \frac{2\sqrt{2}\zeta(3)}{\pi^2} G_F T^3 \left(\mathcal{L} \pm \frac{\eta}{4}\right) \simeq 0.34\, G_F T^3 \mathcal{L} \;, \tag{2.85}$$

where $\zeta(3) \simeq 1.202$ is the Riemann zeta function, $\eta \simeq 6 \times 10^{-10}$ is the baryon-to-photon ratio [9] that represents the lepton asymmetry stored in electrons (which is equal to the baryon asymmetry due to charge neutrality), the "+" sign is taken for $\alpha = e$ while "-" is for $\alpha = \mu, \tau$ and $\mathcal{L}$ is the lepton number[12] in active neutrinos,

$$\mathcal{L} = 2L_{\nu_\alpha} + \sum_{\beta \neq \alpha} L_{\nu_\beta} \ . \tag{2.86}$$

The individual lepton number for each active neutrino flavor is $L_{\nu_\alpha} = (n_{\nu_\alpha} - n_{\bar{\nu}_\alpha})/n_\gamma$, where n_γ is the photon number density. BBN constrains the magnitude of the electron neutrino asymmetry to be $|L_{\nu_e}| \lesssim \mathcal{O}(10^{-3})$ [201]. The upper limit imposed by BBN and CMB on the asymmetries in the other neutrino flavors is larger, $|L_{\nu_\mu,\nu_\tau}| \lesssim \mathcal{O}(10^{-1})$ [202]. Throughout our discussion $\mathcal{L} \gg \eta$ and hence η is neglected. If neutrino oscillations efficiently redistribute the lepton asymmetry among the flavors, the resulting lepton number is

$$\mathcal{L} \simeq \frac{4}{3} \sum_\alpha L_{\nu_\alpha} \ . \tag{2.87}$$

For non-resonant (DW) sterile neutrino production, for which V_D is negligible, the maximum of the momentum-integrated production rate over H (namely $(\gamma/H) = d(n_{\nu_s}/n_{\nu_\alpha})/d\ln T$, as considered in the DW paper [135] - see App. 4.1.1) occurs at the temperature $T_{\rm max}$, which for the standard cosmology is [135, 179]

$$T_{\rm max}^{\rm Std} \simeq 108 \ {\rm MeV} \left(\frac{m_s}{\rm keV}\right)^{1/3} \ . \tag{2.88}$$

The temperature $T_{\rm max}$ does not change significantly in the different cosmologies we consider (see App. 4.1.1).

2.6.2 Resonance conditions

For resonant sterile neutrino production [136] we follow the discussion of Ref. [137]. A resonant neutrino conversion occurs when the mixing angle in matter $\sin^2(2\theta_m)$ is maximized. Thus, the condition for resonance is that the square bracket in the denominator of Eq. (2.82), denoted here as $R(T)$, vanishes (i.e. $\sin^2(2\theta_m) = 1$)

$$R(T) \equiv m_s^2 \cos(2\theta) - 2\epsilon T(V_D + V_T) \simeq m_s^2 - aT^4 + bT^6 = 0 \ . \tag{2.89}$$

[12] This is also known as "potential lepton number" [200].

Here, $a \simeq 0.69\, G_F \epsilon \mathcal{L}$, $b = 2\epsilon^2 B$ and $\cos(2\theta) \simeq 1$ for all the mixing angles we consider. In general there are two roots of this equation. Since the lower temperature root corresponds to a larger production rate, it is the only one we consider. In the presence of a sizable lepton asymmetry the dominant resonance occurs at a temperature [136]

$$T_{\rm res} = 18.8 \text{ MeV } \epsilon^{-\frac{1}{4}} \left(\frac{m_s}{\text{keV}}\right)^{\frac{1}{2}} \mathcal{L}^{-\frac{1}{4}} \ . \tag{2.90}$$

Due to the inverse dependence of $T_{\rm res}$ on $\epsilon = p/T$, active neutrinos with lower momentum undergo resonant conversion earlier, at higher temperatures. Thus, with increasing time (decreasing temperature) the resonance "sweeps" from the low momentum end of the active neutrino distribution towards higher momenta, converting active to sterile neutrinos and reducing $\mathcal{L}$, which in turn further increases the sweep rate $\dot{\epsilon}$ (see Eq. (7.11) of Ref. [137]).

The minimum of $R(T)$, where $dR/dT = 0$, occurs at a temperature called $T = T_{\rm PEAK}$ in Ref. [137]. Imposing that $R(T_{\rm PEAK}) = 0$, which amounts to requiring that the two roots of $R(T)$ converge into one, defines the critical lepton number - which we call $\mathcal{L}_{\rm reslim}$ - below which there are no resonances for a given mass m_s and momentum ϵ,

$$\mathcal{L}_{\rm reslim} = 1.83 \times 10^{-4} \epsilon^{\frac{1}{3}} \left(\frac{m_s}{\text{keV}}\right)^{\frac{2}{3}} \left(\frac{B}{10.88 \times 10^{-9}\text{ GeV}^{-4}}\right)^{\frac{2}{3}} \ . \tag{2.91}$$

Namely, given a sterile neutrino mass m_s and momentum ϵ, resonant production occurs only for $\mathcal{L} > \mathcal{L}_{\rm reslim}$.

We display a typical resonance behavior in Fig. 2.5. The right panel shows the contributions of the potentials V_T and V_D as well as the mass term to the denominator of Eq. (2.82), for $m_s = 1$ keV and $\mathcal{L} = 10^{-3}$ as function of the temperature. Resonances occur when the V_D term (blue line) crosses the sum of V_T and the mass term (black line). The left panel shows the production rate $(\partial f_{\nu_s}/\partial T)_\epsilon$ as a function of the temperature T for $m_s = 1$ keV, $\epsilon = 1$ and different values of $\mathcal{L}$: 0 (black line), 10^{-1} (long dashed red line), 10^{-3} (short dashed green line) and $\mathcal{L}_{\rm reslim}$ (dot-dashed blue line). As $\mathcal{L}$ decreases, the two visible resonant peaks move towards each other, eventually merging into one peak at the critical lepton number $\mathcal{L}_{\rm reslim}$ of Eq. (2.91), below which there is no resonance. In this case $\mathcal{L}_{\rm reslim} = 1.83 \times 10^{-4}$ and the figure shows that for $\mathcal{L} > \mathcal{L}_{\rm reslim}$ there are two resonances, with the one at lower T being dominant. For $\mathcal{L} = \mathcal{L}_{\rm reslim}$ there is only one resonance, and none for $\mathcal{L} < \mathcal{L}_{\rm reslim}$.

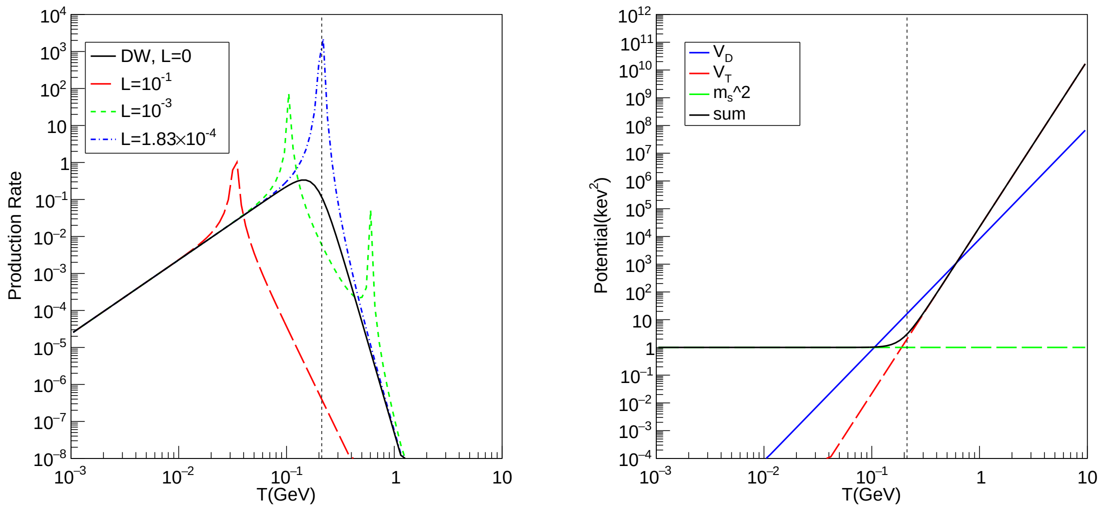

Figure 2.5: [Left] Production rate $(\partial f_{\nu_s}/\partial T)_\epsilon$ for $\epsilon = 1$ and $m_s = 1$ keV in the standard cosmology for non-resonant oscillations with $\mathcal{L} = 0$, i.e. DW production (black solid line), and resonant oscillations with $\mathcal{L} = 10^{-1}$ (red long dashed line), $\mathcal{L} = 10^{-3}$ (green short dashed line) and $\mathcal{L}_{\text{reslim}} = 1.83 \times 10^{-4}$ (blue dot-dashed line). The peaks indicate occurrence of resonances. For large $\mathcal{L}$ only the low temperature peak is visible. As $\mathcal{L}$ decreases, the two visible resonant peaks move towards each other, eventually merging into one peak at the critical lepton number $\mathcal{L}_{\text{reslim}}$ of Eq. (2.91) below which there is no resonance. The resonance temperature for $\mathcal{L}_{\text{reslim}}$ is denoted by the black dotted line. Notice that the high temperature resonance is always significantly suppressed relative to the low temperature resonance. [Right] Contributions of different terms to the denominator of Eq. (2.82), including sterile neutrino mass squared $m_s^2 = 1$ keV^2 (green dashed line), thermal potential V_T (red dashed line), density potential V_D (blue solid line) for $\mathcal{L} = 10^{-3}$, and sum of the mass and thermal potential terms (black solid line), for $\epsilon = 1$. Resonance occurs when the V_D term (blue line) crosses the sum of V_T and the mass term (black line), corresponding to locations of the peaks for $\mathcal{L} = 10^{-3}$ (green short dashed line) shown in the left panel. For $\mathcal{L} = \mathcal{L}_{\text{reslim}}$ the blue and black lines would intersect at only one point and would not cross for $\mathcal{L} < \mathcal{L}_{\text{reslim}}$.

Inverting Eq. (2.91) one can obtain the upper limit on m_s to have a resonance for a given value of $\mathcal{L}$ and momentum ϵ, called $(m_s)_{\rm PEAK}$ in Ref. [137],

$$m_{\rm reslim} = (m_s)_{\rm PEAK} = 4.03 \times 10^5 \text{ keV } \epsilon^{-\frac{1}{2}} \mathcal{L}^{\frac{3}{2}} \left(\frac{B}{10.88 \times 10^{-9} \text{ GeV}^{-4}} \right)^{-1} . \quad (2.92)$$

Assuming $\epsilon = 1$ (ϵ is of $\mathcal{O}(1)$ or smaller for resonant production) for each particular lepton number in Figs. 2.6 to 2.8 resonant production occurs only for $m_s < m_{\rm reslim}$. No resonant production can occur in the region to the right of the vertical line labeled "no res. prod." shaded in dark gray in the figures.

2.6.3 Combined resonant and non-resonant production

When both V_T and V_D terms contribute to the potential of Eq. (2.82), a combination of resonant and non-resonant production could occur at different times. It is thus important to consider the possibility of non-resonant production happening either before or after resonant production. As we will show, non-resonant production cannot happen before the resonant production. Such a scenario would result in a non-negligible initial f_{ν_s}, which we assume to be zero. On the other hand, non-resonant production after the resonant production can result in a second population of sterile neutrinos, hotter than those produced resonantly. As we will discuss, there exists a narrow range of masses below $m_{\rm reslim}$ in which this is possible, consistent with the previous findings of e.g. Refs. [200] and [203].

Sterile neutrinos are produced non-resonantly if the lepton number stored in active neutrinos is small enough so that the V_D potential is negligible with respect to V_T, i.e. $V_T \gg V_D$. This can happen when an earlier resonant production has already depleted the active neutrino lepton asymmetry by converting it into sterile neutrinos, so that V_D becomes small enough with respect to V_T. In this case, there could be non-resonant production after resonant production, for lower temperatures. This regime can be approximately identified by requiring that the temperature of maximum non-resonant production $T_{\rm max}$ (see Sec. 2.6.1) is smaller than the temperature of resonant production $T_{\rm res}$ (see Eq. (2.90)). The condition $T_{\rm max} < T_{\rm res}$ translates into a lower limit on the sterile neutrino mass $m_s > m_{\rm non-res}$. Note that because there is still considerable non-resonant production at temperatures below $T_{\rm max}$,

$m_s \gtrsim m_{\rm non-res}$ is not a strict limit to have significant non-resonant production, which could also happen for masses smaller than but still close to $m_{\rm non-res}$.

For the standard cosmology, using $T_{\rm max}^{\rm Std}$ of Eq. (2.13), we obtain

$$m_s \gtrsim m_{\text{non-res}}^{\rm Std} = 3.59 \times 10^4 \text{ keV } \epsilon_{\rm res}^{\frac{3}{2}} \mathcal{L}^{\frac{3}{2}} \ . \tag{2.93}$$

Analogously, for the ST1 cosmology and using $T_{\rm max}^{\rm ST1}$ of Eq. (2.14) one obtains

$$m_s \gtrsim m_{\text{non-res}}^{\rm ST1} = 6.11 \times 10^4 \text{ keV } \epsilon_{\rm res}^{\frac{3}{2}} \mathcal{L}^{\frac{3}{2}} \ . \tag{2.94}$$

For the K and ST2 cosmologies, $m_{\rm non-res}^{\rm K}$ and $m_{\rm non-res}^{\rm ST2}$ are given in App. 4.2.2.

As we have previously found, for a given lepton number $\mathcal{L}$ resonant production only occurs when $m_s < m_{\rm reslim}$ (see Eq. (2.92)). Combining this upper limit with the lower limit above approximately identifies the range of m_s for each cosmology and each value of $\mathcal{L}$ where it is possible, following our arguments, to produce two distinct populations of the same sterile neutrino,

$$m_{\text{non-res}} \lesssim m_s < m_{\rm reslim} \ . \tag{2.95}$$

For $\epsilon = 1$ this range defines the vertical bands diagonally hatched in red shown in Figs. 2.6 to 2.8, for four different cosmologies and four values of the initial lepton number that we consider. Note that full resonant production, where both the adiabaticity and coherence conditions discussed below are satisfied (shown as blue or red wedges in Figs. 2.6 to 2.8), seldom happens within the bands set by Eq. (2.95).

Another condition for two sterile neutrino populations to appear, assumed implicitly above, is that the initial lepton number $\mathcal{L}$ in active neutrinos must be substantially depleted by the resonance. That is, the remaining lepton number after the resonant conversion, $\mathcal{L}_{\rm after}$, must be small enough for the condition necessary for non-resonant production $V_T > V_D$ to hold. We will now show that this approximately requires $\mathcal{L}_{\rm after} \lesssim \mathcal{O}(0.1)\mathcal{L}$.

Consider that at resonance the V_D term (assuming V_T is negligible) is equal to the mass term. On the other hand, for non-resonant production at $T_{\rm max}$ (Eq. (2.88) for the Std cosmology and App. 4.1.1 for other cosmologies), the V_T term is always approximately a fraction ~ 0.34 of the mass term[13], assuming that the $V_D \ll V_T$. Since V_D is linearly dependent on $\mathcal{L}$, immediately after the lepton number depletion at the resonance, the V_D term diminishes by a factor of $(\mathcal{L}_{\rm after}/\mathcal{L})$. Thus, we need $(\mathcal{L}_{\rm after}/\mathcal{L}) \lesssim 0.1$ in order to ensure $V_T > V_D$. This is often the case, e.g. the numerical simulations of resonant production of Ref. [204] find that $\gtrsim 90\%$ of the initial lepton number is depleted across a wide range of input parameters. The appearance of two sterile neutrino populations from non-resonant production that occurs after the resonant production, has been also found in some previous calculations, e.g. in Ref. [200]. For example, Fig. 1 of Ref. [200] shows that about 30% of the sterile neutrino relic density is produced non-resonantly after significant lepton number depletion by resonant production. Using the parameters of that figure ($L_{\nu_e} = L_{\nu_\mu} = L_{\nu_\tau} = 1.1 \times 10^{-3}$, i.e. $\mathcal{L} = 4.4 \times 10^{-3}$ and $m_s = 64$ keV), we see that the assumed sterile neutrino mass is in between $m_{\text{non-res}} \simeq 10$ keV and $m_{\rm reslim} \simeq 117$ keV, for $\epsilon = 1$ (a value of ϵ consistent with the resonant production shown in the same figure), in agreement with our finding in Eq. (2.95).

Two such populations of sterile neutrinos have been also found in Ref. [203] for $m_s \simeq$ O(keV) (e.g. for $m_s = 3$ keV in Fig. 1 of Ref. [203]), assuming the standard cosmology and a "lepton asymmetry parameter" $L_6 = 16$ (denoting $L = 16 \times 10^{-6}$). As we explain now, these parameters appear to be consistent with Eq. (2.95), when expressed in terms of a range of $\mathcal{L}$ values for a fixed mass m_s. Using Eqs. (2.92) and (2.93) (taking the B-dependent factor to be 1) in Eq. (2.95), translates into the following condition for two populations to be produced,

$$1.8 \times 10^{-4}\, \epsilon^{1/2} \left(\frac{m_s}{\rm keV}\right)^{2/3} < \mathcal{L} < 9.2 \times 10^{-4}\, \epsilon^{-1} \left(\frac{m_s}{\rm keV}\right)^{2/3} . \tag{2.96}$$

For $\epsilon \simeq 1$ and $m_s = 3$ keV (in agreement with what is shown in Fig. 1 of Ref. [203]), we see that $\mathcal{L}$ should be of order 10^{-4} for our condition of Eq. (2.96) to be fulfilled. It may seem contradictory then, that the "lepton asymmetry parameter" is $L_6 = 16$ in Fig. 1 of

[13]Here we used the definition of $T_{\rm max}$ which yields Eq. (2.88) (and the values in App. 4.1.1 for non Std cosmologies) and $\epsilon = 3.15$, which is the average value of ϵ resulting from DW production. We note that in Ref. [67, 66] a different definition of $T_{\rm max}$ is used (not employing the momentum integrated rate and thus ϵ dependent), which results in the V_T term being approximately 0.2 of the mass term at $T_{\rm max}$ instead. This does not significantly affect our arguments.

Ref. [203]. However, this parameter is defined as $L_6 = 10^6(n_{\nu_e} - \bar{n}_{\nu_e})/s$ and, in the model used in Ref. [203] (see e.g. Ref. [205]), there are 9 Weyl leptonic spinors with equal asymmetry L_6, which for us translates into $\mathcal{L} \simeq 9(s/n_\gamma)10^{-6}L_6 \simeq 1.44 \times 10^{-4}(s/n_\gamma)$ for $L_6 = 16$. Additionally, the entropy density s is larger than n_γ. Although a strict comparison of the results of Ref. [203] with ours is difficult to make due to the complexities of their model, the lepton asymmetry specified in Ref. [203] appears to be compatible with our condition of Eq. (2.96) to have two sterile neutrino populations, both produced via active sterile neutrino oscillations.

Let us now demonstrate that non-resonant sterile production does not occur prior to a resonant production. Resonant production after non-resonant production, i.e. $T_{\rm res} < T_{\rm max}$, would require that at some temperature the V_D term is equal to the mass term (the condition for resonance) while at higher temperatures, when both the V_D and V_T terms are larger (as both grow with increasing temperature) the V_T would be only $\sim 0.34 \times$ (mass term) and $V_D < V_T$ (the condition at maximum-non resonant production). This is not possible, since the mass term does not change with temperature. Hence, whenever $T > T_{\rm res}$ the mass term is guaranteed to be smaller than the V_D term.

As an example of the preceding argument, let us consider the case of the standard cosmology. Using $T^{\rm Std}_{\rm max}$ from Eq. (2.13), the requirement of $V_D(T_{\rm max}) < V_T(T_{\rm max})$ translates into the condition

$$m_s > 5.5 \times 10^6 \text{ keV} \epsilon^{-3/2} \mathcal{L}^{3/2} \left(\frac{B}{10.88 \times 10^{-9} \text{ GeV}^{-4}} \right)^{-1} . \tag{2.97}$$

However, this condition is incompatible with having a resonance, $m_s < m_{\rm reslim}$ in Eq. (2.92). This implies that significant non-resonant sterile neutrino production does not occur before resonant production, which is also true for the non-standard cosmologies we consider.

The considerations we discussed in this section thus far apply to all cases of resonant production in general. In the next subsection we focus specifically on fully resonant conversion.

2.6.4 Fully resonant conversion

A “fully resonant" neutrino production requires that two additional conditions hold during resonance: coherence and adiabaticity [137]. If both are satisfied, there is a Mikheyev-Smirnov-Wolfenstein (MSW) resonance [206, 207].

The first condition, coherence, ensures that neutrinos do not suffer scattering-induced de-coherence as they propagate through the resonance. It is satisfied if the active neutrino mean free path (the inverse of the scattering rate Γ_α given above Eq. (2.81)) is significantly larger than the resonance width $\delta r_{\rm res}$,

$$\Gamma_\alpha^{-1} > \delta r_{\rm res} \simeq \frac{\tan(2\theta)}{3H} \simeq \frac{\sin(2\theta)}{3H} \ , \tag{2.98}$$

where we took $\cos(2\theta) \simeq 1$. This condition translates into an upper limit on the active-sterile mixing during resonance

$$\sin^2(2\theta) < \frac{9H^2}{G_F^4 \epsilon^2 T_{\rm res}^{10}} \ , \tag{2.99}$$

which defines the regions below the solid red lines in Figs. 2.6 to 2.8 (below the upper boundary of the red shaded wedges). Substituting $T_{\rm res}$ from Eq. (2.90) into Eq. (2.99) explicitly shows the dependence on the lepton number. The resulting expression for this upper limit written in terms of the η and β parameters is given in Eq. (4.39). In the Std cosmology this is

$$\sin^2(2\theta)^{\rm Std} < 2.19 \times 10^{-6} \epsilon^{-\frac{1}{2}} \left(\frac{m_s}{\rm keV}\right)^{-3} \mathcal{L}^{\frac{3}{2}} \left(\frac{g_*}{10.75}\right) \ , \tag{2.100}$$

while for ST1 the upper limit is much higher

$$\sin^2(2\theta)^{\rm ST1} < 1.38 \times 10^5 \epsilon^{-0.09} \left(\frac{m_s}{\rm keV}\right)^{-3.82} \mathcal{L}^{1.91} \left(\frac{T_{\rm tr}}{5\ {\rm MeV}}\right)^{1.64} \left(\frac{g_*}{10.75}\right) \ . \tag{2.101}$$

Results for K and ST2 are given in Appendix 4.2.3.

When the neutrino flavor evolution is adiabatic, neutrinos oscillate many times during the resonance width, in which case flavor conversion is very efficient and the lepton number in active neutrinos is quickly transferred to sterile neutrinos. Comparing the neutrino oscillation length $l_m^{\rm res}$ in matter at the resonance

$$l_m^{\rm res} = \frac{4\pi\epsilon T_{\rm res}(\epsilon)}{m_s^2 \sin(2\theta)} \tag{2.102}$$

with the resonance width $\delta r_{\rm res}$ from Eq. (2.98), the degree of adiabaticity can be characterized using the γ parameter (see e.g. [137]),

$$\gamma = 2\pi \frac{\delta r^{\rm res}}{l_m^{\rm res}} \simeq \frac{m_s^2}{2\epsilon T_{\rm res}} \sin^2(2\theta) \left| 4\frac{\dot{T}}{T} + \frac{\dot{\mathcal{L}}}{\mathcal{L}} \right|^{-1} = \frac{m_s^2}{2\epsilon T_{\rm res}} \sin^2(2\theta) \left| 4H - \frac{\dot{\mathcal{L}}}{\mathcal{L}} \right|^{-1} . \quad (2.103)$$

The condition $\gamma > 1$ for adiabatic evolution ensures that the change in mass eigenstates proceeds slowly during level crossing at the resonance, so that the probability of jumping between mass eigenstates is low[14]. Eq. (2.103) shows that for an evolution initially described by $\gamma \gg 1$ to not lead to one with $\gamma < 1$, the sweep $(\dot{\mathcal{L}}/\mathcal{L})$ should remain small, not much larger than H (see the discussion in Ref. [204]).

If $(\dot{\mathcal{L}}/\mathcal{L}) < H$, we can neglect $(\dot{\mathcal{L}}/\mathcal{L})$ in Eq. (2.103), and the adiabaticity condition $\gamma > 1$ reduces to

$$\sin^2(2\theta) > \frac{8\epsilon H T_{\rm res}}{m_s^2} . \quad (2.104)$$

This condition defines the mass-mixing regions above the long dashed red straight lines in Figs. 2.6 to 2.8 (above the lower boundary of the red shaded wedges). In terms of general parameters η and β, Eq. (2.104) is given in Eq. (4.42). In the Std cosmology, this condition is

$$\sin^2(2\theta)^{\rm Std} > 2.34 \times 10^{-11} \gamma_{\rm lim} \epsilon^{\frac{1}{4}} \left(\frac{m_s}{\rm keV}\right)^{-\frac{1}{2}} \mathcal{L}^{-\frac{3}{4}} \left(\frac{g_*}{10.75}\right)^{\frac{1}{2}} , \quad (2.105)$$

where $\gamma_{\rm lim}$ is the chosen minimum value of the parameter γ (we take $\gamma_{\rm lim} = 1$ for our figures, but in general $\gamma_{\rm lim} \geq 1$). For the ST1 cosmology, the condition becomes

$$\sin^2(2\theta)^{\rm ST1} > 5.88 \times 10^{-6} \gamma_{\rm lim} \epsilon^{0.46} \left(\frac{m_s}{\rm keV}\right)^{-0.91} \mathcal{L}^{-0.55} \left(\frac{g_*}{10.75}\right)^{\frac{1}{2}} \left(\frac{T_{\rm tr}}{5\ \rm MeV}\right)^{0.82} . \quad (2.106)$$

Expressions for the K and ST2 cosmologies are provided in the Appendix 4.2.4.

As the resonance sweeps across the active neutrino momentum distribution $\mathcal{L}$ decreases, while the fractional change in lepton number $(\dot{\mathcal{L}}/\mathcal{L})$ steadily increases. When $(\dot{\mathcal{L}}/\mathcal{L}) \gg H$, as seen from Eq. (2.103), γ rapidly decreases and adiabaticity is lost.

[14] Assuming a linear change in potential across resonance and small mixing angles, the probability of $\nu_\alpha \to \nu_s$ conversion at resonance is $P_{\nu_s \to \nu_\alpha} = 1 - P_{\rm LZ}$, where $P_{\rm LZ} \simeq \exp(-\pi\gamma/2)$ is the Landau-Zener probability [137].

The maximum value of ϵ, $\epsilon_{\rm max}$, can be found from the condition [204]

$$\mathcal{L}(\epsilon_{\rm max}) = \frac{1}{2\zeta(3)}\left(\frac{T_\nu}{T_\gamma}\right)^3 \frac{\epsilon_{\rm max}^3}{(e^{\epsilon_{\rm max}-\xi}+1)} = \mathcal{L}_{\rm init} - \frac{1}{2\zeta(3)}\left(\frac{T_\nu}{T_\gamma}\right)^3 \int_0^{\epsilon_{\rm max}} \frac{x^3}{e^{x-\xi}+1}dx \ . \quad (2.107)$$

To solve this equation we neglect ξ, having verified that $\xi \ll \epsilon_{\rm max}$. The momentum distribution of resonantly produced sterile neutrinos has a sharp peak at $\epsilon \simeq \epsilon_{\rm max}$ (see e.g. Fig. 2 of Ref. [204]). Hence, we can estimate that the average T-scaled momentum is approximately[15] $\langle\epsilon\rangle \simeq \epsilon_{\rm max}$.

To obtain the region in sterile neutrino mass and mixing parameter space associated with adiabaticity and coherence and to compute the limits in Sec. 2.7 that depend on the relic abundance, we numerically solve Eq. (2.107) for $\epsilon_{\rm max}$ and then set $\epsilon = \epsilon_{\rm max}$ in Eq. (2.99) and Eq. (2.104). Eq. (2.107) shows that $\epsilon_{\rm max}$ depends only on the initial value of $\mathcal{L}$, thus is the same for all the cosmologies we consider. For the values of $\mathcal{L}$ used in Figs. 2.6 to 2.8, we find that $\epsilon_{\rm max}$ is

$$\langle\epsilon\rangle \simeq \epsilon_{\rm max} = \begin{cases} 0.03, & \text{for } \ \mathcal{L} = 10^{-5} \\ 0.07, & \text{for } \ \mathcal{L} = 10^{-4} \\ 0.35, & \text{for } \ \mathcal{L} = 10^{-3} \\ 0.83, & \text{for } \ \mathcal{L} = 10^{-2} \ . \end{cases} \quad (2.108)$$

For each particular cosmology we consider, the coherence and adiabaticity conditions determine a wedge shown shaded in red for the Std, ST1, K and ST2 cosmologies in the mass-mixing plane in Figs. 2.6 to 2.8, between the solid and dashed red boundary straight lines, where fully resonant MSW conversion happens. The particular shape of the wedge delineating the full resonance conversion region is governed by the specific temperature dependence of $H(T)$ in each cosmology (i.e. the β dependence in Eq. (2.2)), while the location of the wedge depends on the η parameter. Since the coherence condition (upper solid boundary line) of Eq. (2.99) scales as H^2 and the adiabaticity condition (lower dashed boundary line) of Eq. (2.104) scales as H, the wedges of non-standard cosmologies with higher expansion rates compared to Std move to larger mixings, and those with lower expansion rates move to smaller mixings.

[15] We note that this approximation may not entirely capture the relevant behavior if the distribution has a long tail in one direction.

Equating the conditions for coherence and adiabaticity, Eq. (2.98) and Eq. (2.103) with $\gamma = 1$, gives

$$\Gamma_\alpha l_m^{\rm res} = 2\pi \ . \tag{2.109}$$

This corresponds to the locus of intersection of the adiabaticity $\gamma = 1$ boundary (lower dashed boundary of the wedges in the figures) and the coherence $\Gamma_\alpha^{-1} = \delta r_{\rm res}$ boundary (the upper solid boundary of the wedges). The line of intersections is valid for all cosmological models and is defined by the following mixing angle as a function of mass

$$\sin^2(2\theta)_{\rm intersect} = 2.60 \times 10^{-16} \epsilon \left(\frac{m_s}{\rm keV}\right)^2 \mathcal{L}^{-3} \ , \tag{2.110}$$

which is indicated with a diagonal dot-dashed violet line in Figs. 2.6 and 2.9. Hence, coherence (i.e. $\Gamma_\alpha^{-1} > \delta r_{\rm res}$) and adiabaticity (i.e. $\delta r_{\rm res} > l_m^{\rm res}/2\pi$) can only happen together for $\sin^2(2\theta) > \sin^2(2\theta)_{\rm intersect}$, where $\Gamma_\alpha^{-1} > l_m^{\rm res}/2\pi$.

As we mentioned above, in the right hand side of Eq. (2.79) we omitted the quantum damping factor $[1 - (\Gamma_\alpha \ell_m/2)^2]^{-1}$ since it is generally negligible for the range of parameters relevant for our study. However, for $\sin^2(2\theta) < \sin^2(2\theta)_{\rm intersect}$, this factor becomes non-negligible at the resonance, where the neutrino oscillation length $\ell_m^{\rm res}$ is maximal. Namely, we have $\ell_m^{\rm res} > 2\pi\Gamma_\alpha^{-1}$ in the parameter space below and to the right of the diagonal violet dot-dashed line labelled "no c. with a." (i.e. "no coherence with adiabaticity") in Figs. 2.6 to 2.8. In this region, neutrino scattering-induced decoherent production takes place (see discussion in Ref. [200]).

Assuming that fully resonant conversion has happened and that most of the initial lepton number $\mathcal{L}$ has been depleted, the present number density of resonantly produced sterile neutrinos, $n_{\nu_s,\rm res}$, is given by

$$n_{\nu_s,\rm res} = \left(\sum L_{\nu_\alpha}\right) n_\gamma = \left(\frac{3}{4}\mathcal{L}\right) \frac{2\zeta(3)}{\pi^2} T_0^3 \ . \tag{2.111}$$

Here we have used Eq. (2.87) to rewrite $\sum L_{\nu_\alpha}$ in terms of $\mathcal{L}$, assuming that neutrino oscillations redistribute efficiently the lepton asymmetry among the flavors, and $T_0 = 2.75$ K is the present temperature of the CMB. Using this equation, the fraction of the DM consisting of resonantly produced sterile neutrinos is

$$f_{s,\mathrm{DM}}^{\mathrm{res}} = \frac{n_{\nu_s,\mathrm{res}}\, m_s}{\rho_{\mathrm{DM}}} = \left(\frac{m_s}{4.08\ \mathrm{eV}}\right)\left(\frac{0.12}{\Omega_{\mathrm{DM}}h^2}\right)\mathcal{L}\ . \tag{2.112}$$

Thus, requiring $f_{s,\mathrm{DM}}^{\mathrm{res}} \leq 1$ implies an upper limit on the sterile neutrino mass. In Figs. 2.6 to 2.8, the portions of the wedges where sterile neutrinos can be fully resonantly produced in which $f_{s,\mathrm{DM}}^{\mathrm{res}} > 1$ are shaded in dark gray and labelled $\Omega_s > \Omega_{\mathrm{DM}}$.

We stress two important assumptions that go into our estimation of $f_{s,\mathrm{DM}}^{\mathrm{res}}$, namely (1) that the conversion is adiabatic and coherent (which does not hold outside the wedges shaded in red, for each particular considered cosmology and lepton number, in Figs. 2.6 to 2.8) and (2) that practically all of the initial lepton number is converted into sterile neutrinos. If only a small fraction of the initial lepton number is converted into sterile neutrinos, their resulting number and energy densities would be reduced by the same fraction. It is important to acknowledge these approximations when comparing our abundance limits to the existing literature that deals with resonant production of sterile neutrinos, e.g. Ref. [208]. For fully resonant conversion the number density is fixed solely by the lepton number and thus the relic energy density is independent of the mixing angle, in contrast to what is shown in Ref. [208].

2.6.5 Thermalization

Similar to the non-resonant production, we must consider the possibility that production of sterile neutrinos due to interactions with the thermal bath could have brought the sterile neutrinos to thermal equilibrium before resonant production could occur. In this case, without significant entropy dilution, sterile neutrinos could contribute to the energy density as much as an active neutrino species, i.e. $\Delta N_{\mathrm{eff}} = 1$, during BBN and thus be forbidden by the limit $N_{\mathrm{eff}} < 3.4$ [9] (see below). The thermal dominant production rate is $\Gamma \simeq \sin^2(\theta_m)\Gamma_\alpha \simeq \sin^2(\theta_m) d_\alpha G_F^2 \epsilon T^5$ (similar to the rate in Eq. (2.81)), where we have used Eq. (2.80) for the active neutrino rate Γ_α and assumed that one sterile neutrino is produced in each interaction instead of an active one. This rate can be suppressed by a large enough lepton number $\mathcal{L}$, because the corresponding density potential V_D diminishes the mixing angle in the medium $\sin(\theta_m)$. This could prevent thermalization even for relatively high vacuum mixing angles. We derive below a conservative upper bound, above which thermalization should occur, and compare it with Fig. 4 of Ref. [181] where the same limit is computed numerically for $m_s \simeq eV$ solving quantum kinetic equations. The parameter space above this bound is forbidden, and possibly, some of the space below near it could be forbidden too by a more accurately derived limit.

The denominator of the matter mixing angle in Eq. (2.82) is dominated by the V_D term for temperatures in between the two resonance temperatures, namely when $2\epsilon T V_D/m_s^2 > 1$, i.e. for temperatures above the lower-temperature resonance, and $2\epsilon T V_D/m_s^2 > 2\epsilon T V_T/m_s^2$ i.e. for temperatures below the higher-temperature resonance. These two conditions give the range of temperatures where the density potential V_D is dominant,

$$0.596\ \text{MeV}\epsilon^{-\frac{1}{4}}\left(\frac{m_s}{\text{eV}}\right)^{\frac{1}{2}}\mathcal{L}^{-\frac{1}{4}} < T < 19.1\ \text{GeV}\epsilon^{-\frac{1}{2}}\mathcal{L}^{\frac{1}{2}} \tag{2.113}$$

We will find the parameter space for which the thermal production rate becomes larger than the expansion rate H, i.e. $\Gamma/H > 1$, within this temperature range but outside the resonances, which we take as condition for thermalization. We thus compute Γ/H when $2\epsilon T V_D/m_s^2 = x > 1$, where x is a positive real parameter, namely when

$$T = 0.596\ \text{MeV}x^{\frac{1}{4}}\epsilon^{-\frac{1}{4}}\left(m_s/\text{eV}\right)^{\frac{1}{2}}\mathcal{L}^{-\frac{1}{4}}\ . \tag{2.114}$$

Since we are computing Γ/H always at this temperature, when Γ/H=1 this is also the freeze-out temperature $T_{\text{f.o.}}$. We choose $x = 3$ for Figs. 2.6 to 2.8. For this evaluation, we neglect the 1 and the V_T terms in the denominator of the matter mixing angle, Eq. (2.82). In the Std cosmology, the $\Gamma/H > 1$ thermalization condition is fulfilled and thus rejects the mixings

$$\sin^2(2\theta) > 119\frac{(1-x)^2}{x^{\frac{3}{4}}}\left(\frac{\epsilon}{3.15}\right)^{\frac{3}{4}}\left(\frac{m_s}{\text{eV}}\right)^{-\frac{3}{2}}\mathcal{L}^{\frac{3}{4}}\left(\frac{g}{10.75}\right)^{\frac{1}{2}}\ , \tag{2.115}$$

and for ST1, it rejects

$$\sin^2(2\theta) > 6.17\times 10^8\frac{(1-x)^2}{x}\left(\frac{\epsilon}{3.15}\right)\left(\frac{m_s}{\text{eV}}\right)^{-2}\mathcal{L}\left(\frac{g}{10.75}\right)^{\frac{1}{2}}\ . \tag{2.116}$$

Results for K and ST2 are given in Appendix 4.2.5. The region where thermalization is reached is shown in each panel of Figs. 2.6 to 2.8 shaded in cyan with the label "therm.".

When the freeze-out temperature $T_{\rm f.o.}$ in Eq. (2.114) becomes smaller than 5 MeV the "therm." region for non-standard cosmologies should become the equal to the standard cosmology region (since sterile neutrino would be in equilibrium after the cosmology becomes standard). This means that in all our figures for non-standard cosmologies the "therm." cyan region has a vertical left boundary at $T_{\rm f.o.} = 5$ MeV (because the Std. region does not extend to the left of this boundary).

In the darker cyan region, sterile neutrinos would be as abundant or almost as abundant as active neutrinos, thus this regions is forbidden by the $\Delta N_{\rm eff} < 0.4$ BBN limit (see below). Due to the entropy increase of interacting species between $T_{\rm f.o.}$ and the freeze-out of active neutrinos at 3 MeV, when $T_{\rm f.o.}$ becomes larger than about 250 MeV (above the QCD phase transition), the sterile neutrino number density is diluted by a factor of about 5, so that sterile neutrinos become allowed by the $\Delta N_{\rm eff}$ limit. This transition is indicated with a lighter cyan shade. Another transition to a yet lighter cyan is indicated when $T_{\rm f.o.}$ becomes larger than 1 GeV and the entropy dilution factor becomes close to 8.

The bound in Eq. (2.116) is valid as long as the conditions in Eq. (2.113) are satisfied which can only happen if the lepton number is large enough, namely for

$$\mathcal{L} > 2.1 \times 10^{-6} \left(\frac{\epsilon}{3.15}\right)^{\frac{1}{3}} \left(\frac{m_s}{\rm eV}\right)^{\frac{2}{3}} \left(\frac{x}{3}\right)^{\frac{1}{3}} . \tag{2.117}$$

This condition agrees with Refs. [181, 209] (assuming m_s is much larger than the active neutrino mass, as we do here) in that for $m_s \simeq$ eV, the mass range required for MiniBoone/LSND, enough suppression of the mixing in matter by the V_D term to avoid thermalization requires a lepton number $\mathcal{L} > 10^{-5}$ (so the effect of $\mathcal{L}$ less than approximately 10^{-5} is similar to that of $\mathcal{L} = 0$ [181]). As can be seen in Fig. 2.8 in the MiniBoone/LSND parameter region (hatched in black) in the standard cosmology (upper left panel) sterile neutrinos are partially or fully thermalized ($\Delta N_{\rm eff} \approx 1$) for a lepton asymmetry $\mathcal{L} = 10^{-5}$, and for this and smaller values of $\mathcal{L}$ would thus be in tension with CMB/BBN bounds on $N_{\rm eff}$ (see Sec. 2.7). Comparing our bound in Eq. (2.115) for the standard cosmology and $\mathcal{L} \simeq 10^{-2}$ to the $\Delta N_{\rm eff} = 0.6$ limit in the upper panel of Fig. 4 of Ref. [181], we see that both are similar in magnitude and shape.

The lower limit in Eq.(2.117) with $x = 1$ is similar to the lower limit necessary to have a resonance $\mathcal{L}_{\text{reslim}}$ in Eq. (2.91), since the V_D term needs to be equal to the sum of the other two terms in the denominator of Eq. (2.82) to have a resonance and in our case the V_T term is small. This is why in Figs. 2.6 to 2.8 the cyan thermalization region finishes at the boundary of the dark gray region of no resonance production.

So far we have considered the condition for chemical equilibrium of sterile neutrinos. We would like to point out that kinetic decoupling happens before chemical decoupling. The sterile neutrino scattering rate contains an extra $\sin^2\theta$ factor over the production rate. Thus sterile neutrinos that are not in chemical equilibrium are also not in kinetic equilibrium.

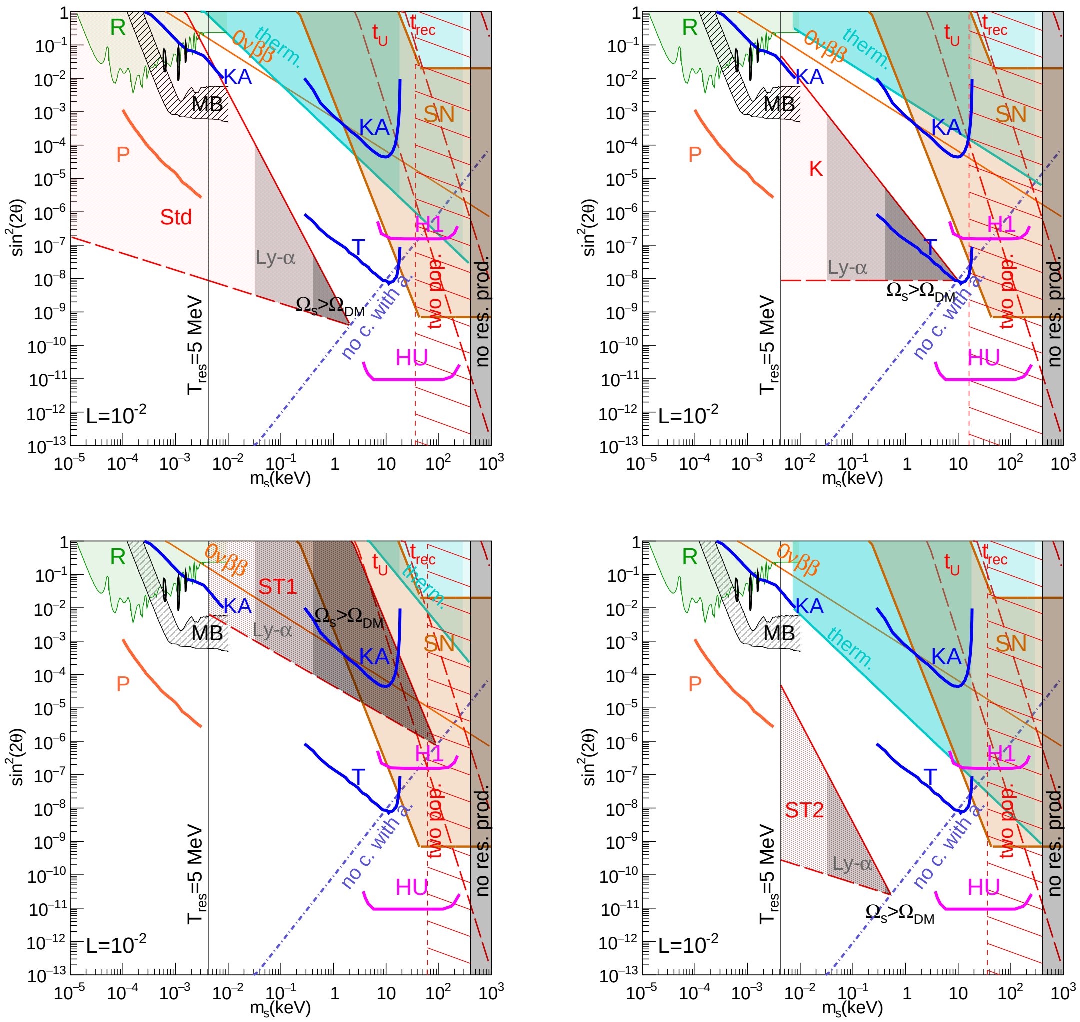

Figure 2.6: Regions/limits for resonantly produced ν_s mixed with ν_e, for Std, K, ST1 and ST2 cosmologies assuming $\mathcal{L} = 10^{-2}$. Resonant production is not possible to the right of the "no res. prod." vertical black line (gray shading). Additional non-resonant production is possible in the adjacent diagonally red hatched vertical strips. $T_{\rm res} < 5$ MeV to the left of the $T_{\rm res}$=5 MeV line. Fully resonant conversion possible only above the violet dot-dashed diagonal line, within the red wedges between the adiabaticity and coherence limits. Regions excluded by $\Omega_s > \Omega_{\rm DM}$ and Ly-α/HDM [10] limits for fully resonantly produced ν_s, thermalization ("therm.") and reactor data (R) [6, 7, 8] are shaded in dark gray, gray, dark cyan and green respectively (lighter cyan "therm." regions allowed due to entropy dilution). Shown are the upper limit from $0\nu\beta\beta$ decays (orange) [25], the Majorana ν_s lifetimes $\tau_S = t_U$, $t_{\rm rec}$ and $t_{\rm th}$ (dashed red), the reach of KATRIN (KA) and TRISTAN 3 yr (T) [17, 18] in blue, HUNTER phase 1 (H1) and upgrade (HU) [19] in purple, and PTOLEMY for 100 g-yr (P) (Figs. 6 and 7 of [24]) in orange, the region (SN) disfavored by supernovae [3] (shaded in brown), the 4-σ band of compatibility with LSND and MiniBooNE data (MB) in Fig. 4 of [20] (hatched in black) and regions allowed at 3-σ by DANSS [21] and NEOS [22] data in Fig. 4 of [23] (3 black vertical contours).

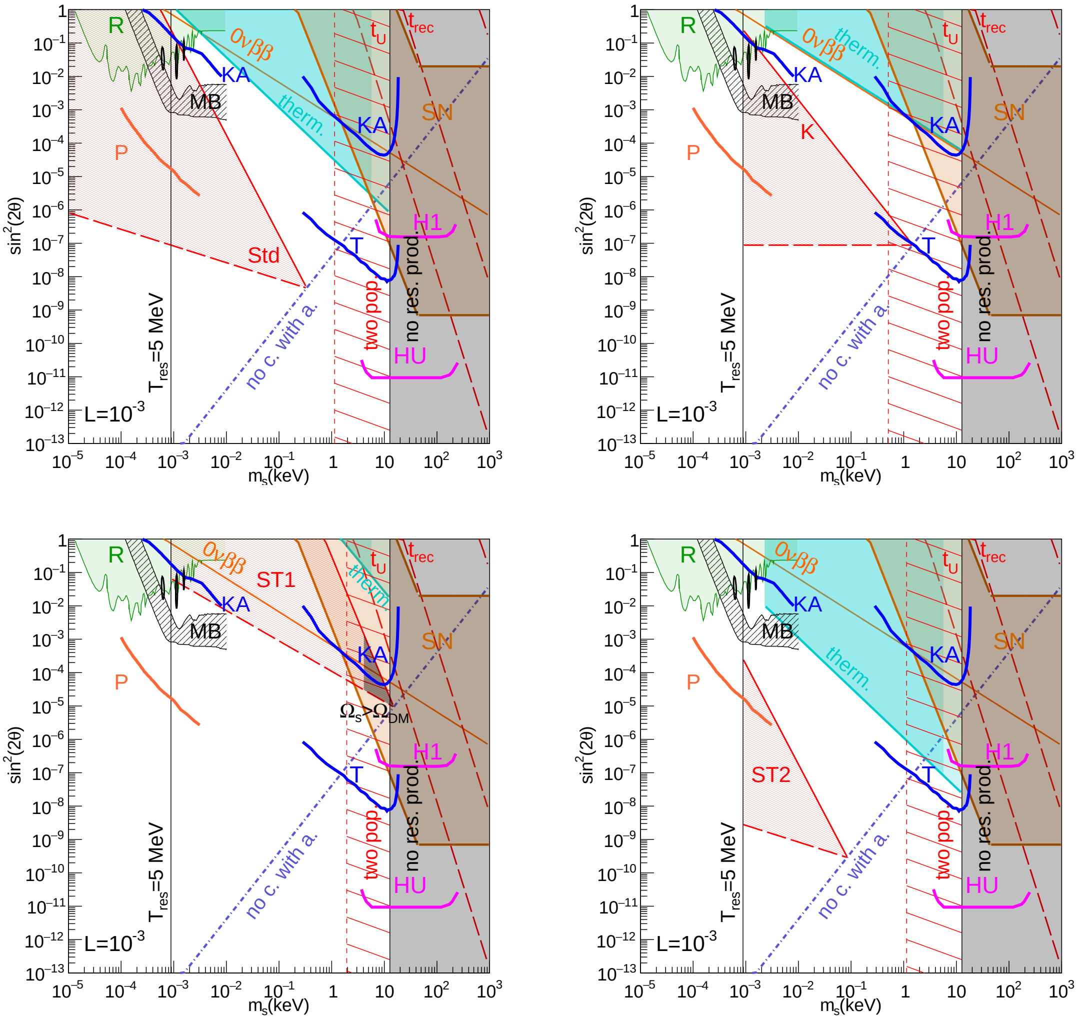

Figure 2.7: As in Fig. 2.6, but for $\mathcal{L} = 10^{-3}$.

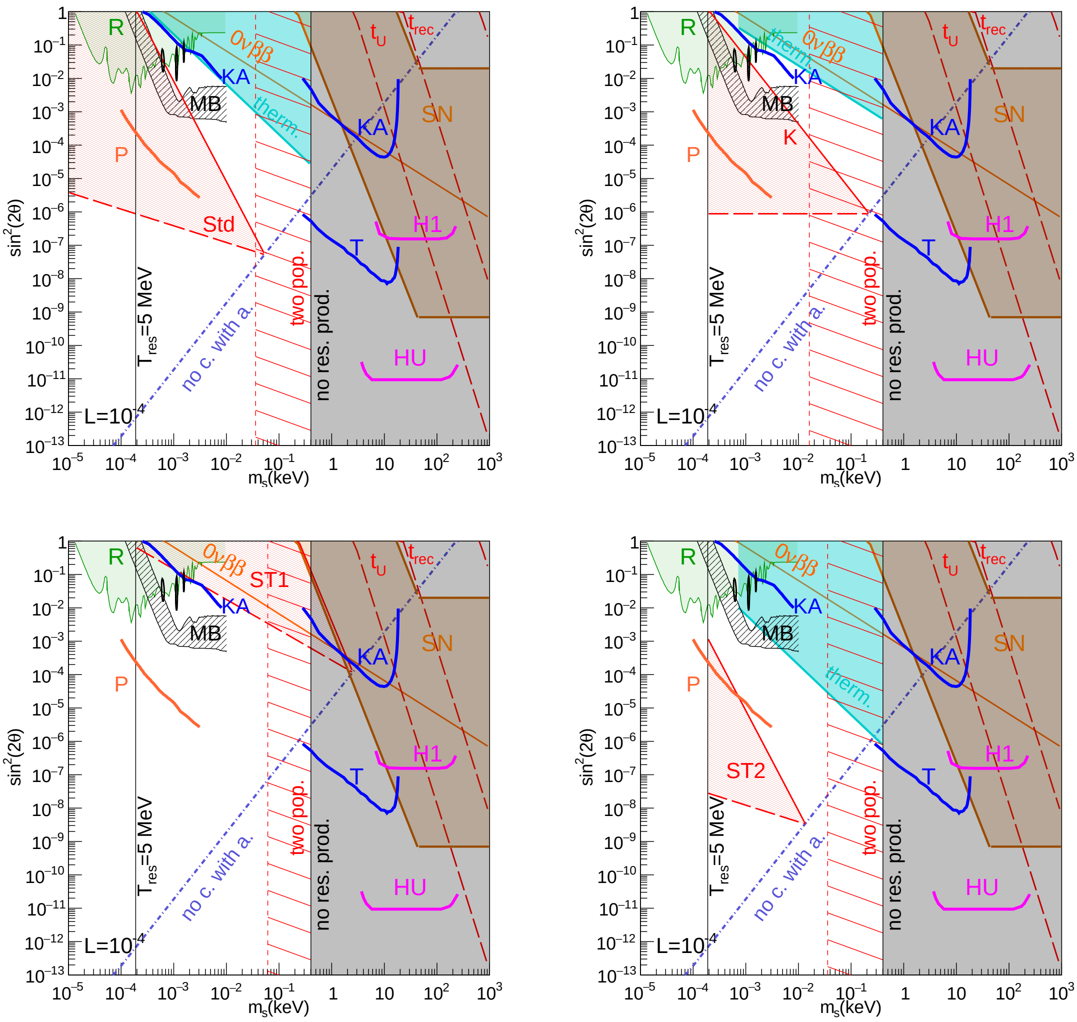

Figure 2.8: As in Fig. 2.6, but for $\mathcal{L} = 10^{-4}$.

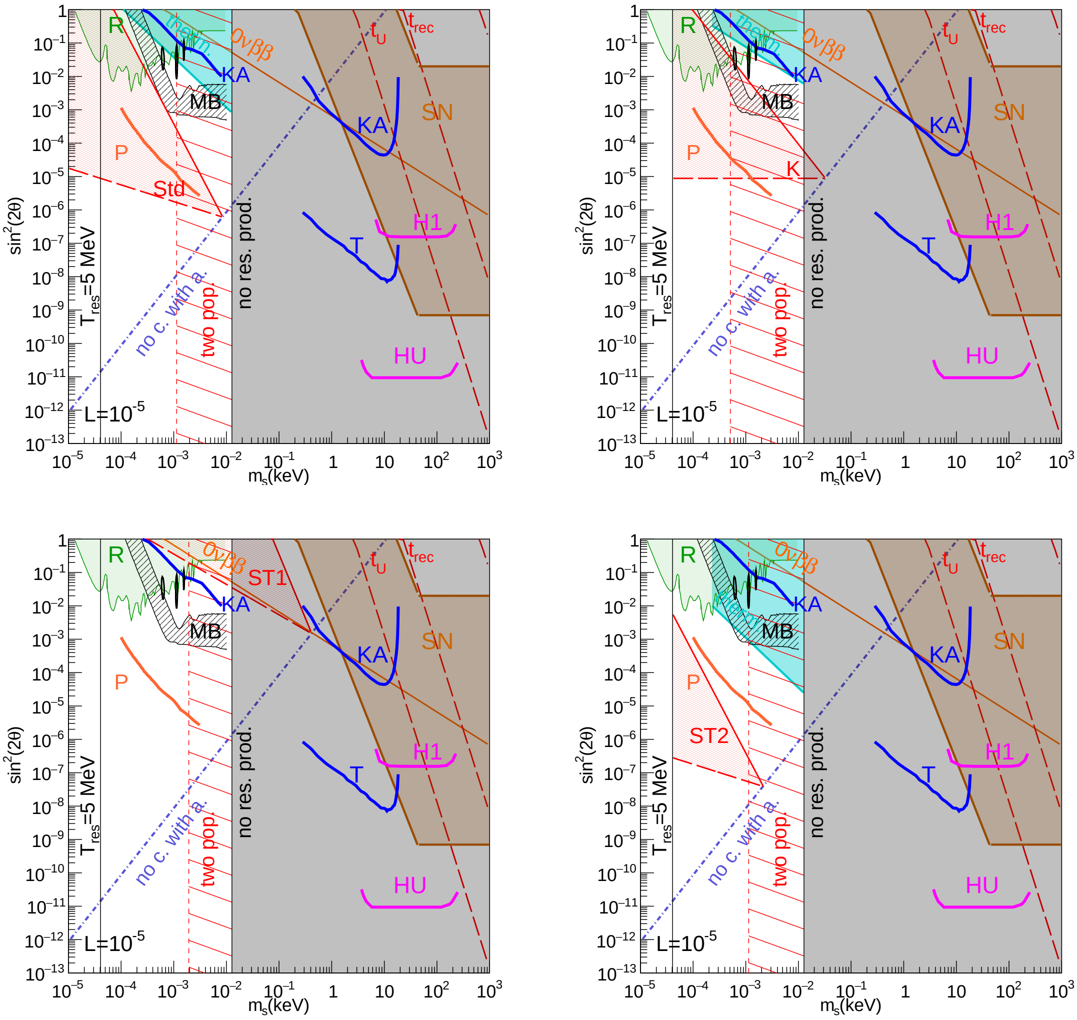

Figure 2.9: As in Fig. 2.6, but for $\mathcal{L} = 10^{-5}$.

2.7 Limits and potential signals for Resonant Production

We consider here the same constraints and regions of interest in the mass-mixing plane for resonantly produced sterile neutrinos in different pre-BBN cosmologies as we considered in our studies of non-resonant production [66, 67, 68] (see section 2.5), modifying the relic density and characteristic momentum as necessary. The difference in the sterile neutrino production mechanism only affects the limits that depend on these quantities. Here we focus primarily on the changes due to the different production mechanism (resonant vs. non-resonant). The resulting limits and regions of interest are shown in Figs. 2.6 to Fig. 2.8, where we assume that the sterile neutrino only mixes with ν_e. Since we assume fully resonant conversion (i.e. coherent and adiabatic) in computing the relic abundance and characteristic momentum, the limits that depend on the relic abundance and momentum are only shown within the red shaded wedges in which sterile neutrinos can be fully resonantly produced. We note that there are scalar-tensor cosmologies that produce wedges in between those we show for ST1 and ST2, always above the dot-dashed violet line. As with the non-resonant case, we consider the effects of thermalization on these limits (see section 2.6.5) which is largely encapsulated by the cyan region in Figs. 2.6 to 2.8.

Warm DM candidates are constrained by observations related to structure formation, which is suppressed below their free-streaming scales. In particular, measurements associated with $\sim 0.1 - 1$ Mpc scales [10], as probed by the Lyman-α forest absorption spectrum[16], provide a strong limit on $\mathcal{O}$(keV) mass sterile neutrinos. Typically, bounds from Lyman-α are given in the literature in terms of the mass $m_{\rm therm}$ of a thermally produced particle with a Fermi-Dirac spectrum. While for non-resonant production the average momentum of such particles $\langle \epsilon \rangle$ is close to 3 for all the cosmologies we consider, resonantly-produced sterile neutrinos have a lower average momentum that is close to or below 1 (see Eq. (2.108)). Following Ref. [182] (see discussion in section 2.5 [67]), the limit on the sterile neutrino m_s

[16]Structure formation on similar scales can be also probed via DM halo counts [131].

can be related to a given limit on the mass of a thermal relic $m_{\rm therm}$ as

$$m_s = 4.46\ \text{keV}\ \left(\frac{\langle\epsilon\rangle}{3.15}\right)\ \left(\frac{m_{\rm therm}}{\text{keV}}\right)^{\frac{4}{3}}\ \left(\frac{T_{\nu_s}}{T_{\nu_\alpha}}\right)\ \left(\frac{0.12}{f_{\rm s,DM}\ \Omega_{DM}\ h^2}\right)^{\frac{1}{3}}\ , \tag{2.118}$$

where $T_{\nu_s}/T_{\nu_\alpha} = (10.75/g_*)^{1/3}$. Taking $g_* = 10.75$, we use Eq. (2.118) to translate to m_s the limits of Ref. [10]. We take the 2-σ bound on warm DM from SDSS+XQ+HR data shown on the right panel of Fig. 6 of Ref. [10], but extend the limit horizontally to smaller masses, at 8% of the DM energy density. To obtain the corresponding Lyman-α bounds for sterile neutrinos, which reject the gray vertical bands shown within the wedges in Fig. 2.6, we bounded the mass-mixing region by finding where the predicted DM fraction in each cosmology and for each $\mathcal{L}$ value becomes larger than the published 2-σ limit. Fully resonant sterile production affects the limits on m_s found through Eq. (2.118), due to the different values of $\langle\epsilon\rangle$ it predicts, which decrease as $\mathcal{L}$ decreases. For small $\mathcal{L}$, the corresponding $\langle\epsilon\rangle$ is also small, as shown in Eq. (2.108), i.e. a colder momentum distribution. Due to the diminished number density in Eq. (2.112), along with the $\langle\epsilon\rangle$ dependence in Eq. (2.118), there are no Ly-α bounds for $\mathcal{L} < 10^{-3}$, thus the limit is only shown in Fig. 2.6.

Astrophysical indirect detection searches for X-ray emission probe the radiative decay $\nu_s \to \nu_\alpha\gamma$, whose lifetime τ_γ is [191, 192]

$$\tau_\gamma^{-1} \simeq 1.38 \times 10^{-32} s^{-1}\left(\frac{\sin^2(2\theta)}{10^{-10}}\right)\left(\frac{m_s}{\text{keV}}\right)^5\ , \tag{2.119}$$

of sterile neutrinos in galaxies and galaxy clusters provide stringent constraints for $m_s > 1$ keV [11, 12, 13]. Additionally, observations of the diffuse extragalactic background radiation (DEBRA) [14] limit the integrated flux from sterile neutrino decays occurring between the recombination time $t_{\rm rec}$ and the present (thus it extends to $\tau = t_{\rm rec}$). However, these limits scale with the density of sterile neutrinos and affect neutrinos with masses $m_s \geq 1$ keV. Since our regions of interest are either already bounded by other limits at the keV scale or do not reach this mass, we do not show the X-ray/DEBRA bounds.

BBN imposes a limit on $N_{\rm eff}$, the effective number of active neutrino species, contributing to the energy density during BBN. In addition to $N_{\rm eff} = 3.045$ coming from active neutrinos [183, 184], fully resonantly produced sterile neutrinos provide an extra contribution of

$$\Delta N_{\text{eff}} = N_{\text{eff}} - 3.045 \simeq \left(\frac{\langle\epsilon\rangle}{3.15}\right)\left(\frac{n_{\nu_s}}{n_{\nu_\alpha}}\right)\left(\frac{10.75}{g_*}\right)^{1/3}. \tag{2.120}$$

Using Eq. (2.111), the current 95% confidence level BBN bound[17] of $N_{\text{eff}} < 3.4$ [9] can be thus translated into an upper bound on the lepton number

$$\mathcal{L} = 0.36\ \Delta N_{\text{eff}}\left(\frac{\langle\epsilon\rangle}{3.15}\right)^{-1}\left(\frac{g_{\nu_s}}{10.75}\right)^{\frac{1}{3}} < 0.14\left(\frac{\langle\epsilon\rangle}{3.15}\right)^{-1}\left(\frac{g_{\nu_s}}{10.75}\right)^{\frac{1}{3}}. \tag{2.121}$$

Since the average momentum of fully resonantly produced sterile neutrinos is $\langle\epsilon\rangle < 3.15$ (see Eq. (2.108)), for $\Delta N_{\text{eff}} < 0.4$ the values of $\mathcal{L}$ chosen for Figs. 2.6 to 2.8 easily evade this limit in the absence of thermalization. In the dark cyan shaded region where thermalization occurs, sterile neutrinos have the same (or close to the same) relic number density as one specifies of active neutrinos, i.e. $\Delta N_{\text{eff}} = 1$ (or close to 1, depending on entropy dilution) which is forbidden by the present limit (in the lighter cyan regions entropy dilution brings the sterile neutrino number density to be below the present limit, as explained above).

Sterile neutrinos produced in supernova explosions could result in significant energy loss [3], disfavoring the brown region of parameter space labelled “SN" displayed in Figs. 2.6 and 2.9. It is difficult to exclude this region entirely, due to large uncertainties associated with the process [137] (for recent related studies of sterile neutrinos mixing with ν_μ and ν_τ see Ref. [190, 189]).

Laboratory experiments can directly probe sterile neutrinos in the eV and keV mass-ranges by searching for active neutrino appearance or disappearance due to active-sterile neutrino mixing. These searches are completely independent of cosmology. In the eV-mass range, we display in Figs. 2.6 and 2.9 the combined limits (denoted by “R”, green shading) from Daya Bay [6], Bugey-3 [7] and PROSPECT [8], assuming sterile mixing with ν_e. We highlight the regions (densely hatched in black) corresponding to the anomalous signals[18] in

[17] This bound is similar in magnitude to the N_{eff} constraint from CMB observations of Planck-2018 [46], which is however only applicable to sterile neutrinos with mass of $m_s \ll 1$ eV. Bounds on effective sterile neutrino mass $m_{s,eff}$ or the sum of active neutrino masses [46, 210] from Planck-2018, BICEP2/Keck and BAO data do not significantly affect our results.

[18] We stress that these signals are in strong tension with results from IceCube [195] and MINOS [196].

LSND [121] and MiniBooNE [122, 20] data, reproduced from Fig. 4 of Ref. [20]. Additionally, we display (3 black vertical elliptical contours) the anomalous signal regions from DANSS [21] and NEOS [22] data, following Fig. 4 of Ref. [23]. The eV-mass parameter space region will be further tested with KATRIN [18] (solid blue lines) and PTOLEMY [24] (solid orange lines) experiments. In the keV-mass range, KATRIN [197, 198] and its upgraded version TRISTAN [17] (solid blue lines), as well as the upcoming HUNTER [19] (solid magenta lines) experiment, will be able to probe a significant portion of the active-sterile mixing parameter space[19].

Limits on neutrinoless double-beta decay constrain sterile neutrinos mixed with ν_e, if neutrinos are Majorana fermions, through their contribution $\langle m \rangle_s = m_s \sin^2(\theta) e^{i\beta_s}$ to the effective electron neutrino Majorana mass (β_s is a Majorana CP-violating phase). The present bound on the magnitude of this effective mass is $|\langle m \rangle| < 0.165$ eV [15]. Hence, this implies an upper limit (denoted "$0\nu\beta\beta$", solid orange line) of $m_s \sin^2(2\theta) < 0.660$ eV. We note that this bound is not completely robust. The contribution of the sterile neutrino might interfere with the contributions from the active ones, leading to a suppression in the effective Majorana mass and, therefore, avoiding the experimental bounds [199].

2.8 Summary of Sterile Neutrino Results

The early Universe pre-BBN cosmology could be drastically different from the usually assumed radiation-dominated cosmology with SM particle content, as happens in motivated theoretical models – for example in models based on moduli or quintessence. Since no remnant has been detected from the pre-BBN epoch, this era of the early Universe currently remains completely untested. Visible sterile neutrinos, those which could be detected in near future laboratory experiments, could be the first remnants from this epoch. First we revisited the production of sterile neutrinos via non-resonant active-sterile oscillations assuming different cosmologies before the temperature of the Universe was 5 MeV and showed that

[19] The effects of lepton asymmetry on cosmological sterile neutrino bounds at keV mass range have been also recently discussed in Ref. [211].

these neutrinos can act as sensitive probes of the pre-BBN cosmology.

In particular, in section 2.6 we studied non-resonant sterile neutrino production within the standard and several non-standard cosmologies before $T = 5$ MeV. We dealt mostly with cosmological models in which entropy in matter and radiation is conserved, such as the Scalar Tensor and Kination models, using a parameterization of the expansion rate H in terms of its amplitude and temperature dependence that has the particular cosmologies we studied as special cases. We also revisited Low Reheating Temperatures models, in which entropy is not conserved during the non-standard cosmological phase, but sterile neutrinos are produced dominantly in the standard phase, at $T < 5$ MeV. In all cases we assumed that the cosmology is standard at $T < 5$ MeV.

We found that the resulting sterile neutrino relic abundance can be either suppressed or enhanced and that the momentum distribution can be colder or hotter compared to those in the standard cosmology for the same neutrino masses and mixings. We derived general expressions for all relevant quantitites using the mentioned parametrization of H with two parameters, and give them also for the particular cosmological models we studied. We updated and extended the cosmological and astrophysical bounds on all the cosmologies we considered.

In particular, in the Low Reheating Temperature and one of the Scalar Tensor (ST1) models we studied, the cosmological bounds are significantly relaxed, and the mixing of the sterile neutrinos possibly responsible for the 3.5 keV signal is more accessible to the reach of the upcoming KATRIN/TRISTAN and HUNTER experiments. These experiments have already started or are expected to start taking data soon. The observation of a ~ 7 keV mass sterile neutrino in one of them would not only constitute a momentous discovery in particle physics, but also in cosmology, even if this neutrino does not consitute all of the DM. Namely, it would not only constitute the discovery of a new elementary particle, a particle physics discovery of fundamental importance, but could hold vital information about the pre-BBN cosmology from which this sterile neutrino could be the first ever detected remnant.

For example, if the measured mixing would be $\sin^2 2\theta = \mathcal{O}(10^{-7})$, the discovery would be consistent with a non-standard cosmology such as the ST1 and Low Reheating Temperature we studied here. On the other hand, a measured value of $\sin^2 2\theta = \mathcal{O}(10^{-9})$ could instead point towards a Kination model (or maybe special particle models, e.g. [212]). For a $\sin^2 2\theta = \mathcal{O}(10^{-10})$, it would point to a standard pre-BBN cosmology, as indicated in Figs. 2.3 and 2.4 (see the location of the black stars).

The relaxation of cosmological bounds on eV-scale mass sterile neutrinos in non-standard pre-BBN cosmologies, mostly in the Low Reheating Temperature and the ST1 models, allows for the results reported from the LSND, and MiniBooNE short-baseline as well as the DANSS and NEOS reactor neutrino experiments to be unrestricted by cosmology[20]. If the discovery of a sterile neutrino in any of these experiments would be confirmed, again this would be of fundamental importance not only for particle physics, but possibly for the pre-BBN cosmology in which they were produced, and it could provide an indication of a non-standard cosmology in this yet untested epoch.

We have further considered the approach of sterile neutrinos to thermalization that happens for large enough active-sterile mixing angles. The allowed regions of parameter space found in section 2.3 are not affected by these considerations. In particular, the interesting region in which there are several suggested potential signals of a light sterile neutrino with mass close to 1 eV are free from cosmological bounds in the ST1 and LRT cosmologies.

In addition to non-resonant production, we studied the cosmological dependence of resonant sterile neutrino production for sterile neutrino masses between 10^{-2} eV $< m_s < 10^3$ keV, assuming different pre-BBN cosmologies. We derived general expressions for the relevant quantities of adiabaticity and coherence using a simple parametrization of the expansion of the Universe that covers a broad class of cosmologies and which has, as special cases, the particular cosmologies we studied as examples: the standard cosmology (Std), kination (K), and two scalar-tensor models denoted ST1 and ST2. Resonant production can only happen in the presence of a large lepton asymmetry.

We show the regions of interest and different astrophysical and cosmological limits for a ν_s

[20]The cosmological limits can be also suppressed by additional sterile neutrino interactions, such as those due to their coupling to an ultra-light scalar (see e.g. Refs. [213, 214]).

mixed only with ν_e, appropriate for our scenarios in Figs. 2.6 to 2.8 for $\mathcal{L} = 10^{-2}, 10^{-3}, 10^{-4}$ and 10^{-5}, respectively, for the four example cosmologies.

The vertical solid black line labeled "no res. prod." shows the maximum value of the mass in each panel for the given $\mathcal{L}$ and $\epsilon = p/T = 1$ for which resonant production can take place. No resonance production can occur in dark gray shaded region to the right of this line. In all the cosmologies we studied the resulting characteristic momentum is $\epsilon < 1$. The vertical strip to the left of this limit, diagonally hatched in red and labeled "two pop.", indicates the approximate range in which non-resonant production may take place after resonant production. Within this mass range the total momentum distribution would consist of an overlap of two populations of the same sterile neutrino with different characteristic momenta: a colder resonantly produced one with $\epsilon < 1$ and a hotter one with larger characteristic momentum $\epsilon \simeq 3$ (in comparison, the characteristic momentum for non-resonant production we found in section 2.3 [67, 66] is ~ 3 for all the considered cosmologies). We obtained this range by requiring the temperature of maximum non-resonant production $T_{\max}$ to be smaller than the resonance temperature. Since even for temperatures lower than $T_{\max}$ there can still be a considerable rate of non-thermal production, the lower limit of this narrow band is not strict. We note that within this band, the limits on non-resonant production presented e.g. section 2.3 [67, 66] would apply, which are not shown in the figures of this paper (including thermalization limits).

We identified the region (above the dot-dashed violet diagonal lines in each panel in Figs. 2.6 to 2.8) in the mass-mixing plane where both adiabaticity and coherence can happen simultaneously. In this region the damping term appearing in the Boltzmann equation is always negligible (below the dot-dashed violet diagonal lines the damping term is important at resonance). Further, we specifically identified where in the different cosmologies there is fully resonant conversion (in contrast to resonant scattering-induced production), which requires that two conditions hold during resonance: coherence and adiabaticity. A fully resonant conversion leads to a very effective transfer of the initial active neutrino lepton number into a population of sterile neutrinos with number density $n_{\nu_s,\mathrm{res}} \simeq \left(\sum L_{\nu_\alpha}\right) n_\gamma$, independent of the mixing angle, and a characteristic momentum $\epsilon < 1$ that diminishes with the initial lepton number (see Eq. (2.108)). Fully resonant conversion in each of the four cosmologies that we consider occurs in the red shaded wedges in Figs. 2.6 to 2.8, delimited from above by the coherence limit and by the adiabaticity limit from below. We clearly see in the figures that these wedges change considerably with the cosmology, allowing sterile neutrinos that in the standard cosmology would not be fully resonantly produced to be produced in this manner in a non-standard one. This type of production could in principle be distinguished by measuring the relic density and spectrum. To the left of the vertical line labeled $T_{\rm res} = 5$ MeV, resonant production would happen at temperatures smaller than 5 MeV where all our cosmologies become identical to the standard one, thus only the red wedge of the standard cosmology extends to the left of this line.

We note that practically all fully resonantly produced sterile neutrinos would constitute a part of the hot DM (except possibly for the ST1 and K cosmologies and $\mathcal{L} = 10^{-3}$, in which case they might be a subdominant warm DM component with mass close to a keV). Ly-α-HDM limits reject the gray region shown within the wedges in the plots for $\mathcal{L} = 10^{-2}$. To the left of this Ly-α-HDM rejected mass range for $\mathcal{L} = 10^{-2}$, and to the left of the dark gray "no res. prod. region" (where resonant production can happen) for $\mathcal{L} = 10^{-3}, 10^{-4}$ and 10^{-5} fully resonant production yields a viable DM component. The main distinguishing characteristic of these sterile neutrinos would be their colder spectrum (with respect to non-resonantly produced neutrinos). Sterile neutrinos with a colder spectrum could potentially be detected in the future by their impact on the matter power spectrum $P(k)$. In particular, sterile neutrinos would lead to a suppression of $P(k)$ for $k > k_{\rm nr}$ above the scale associated with $k_{\rm nr}$ (smaller length scales), where they become non-relativistic, proportional to their density fraction $f_{s,DM} = \Omega_s/\Omega_{\rm DM}$. This effect would be in addition to the qualitatively similar effect expected from the active neutrino bath $P(k)$ [215, 216, 217].

Finally, we found that the cosmological bounds on eV mass-scale sterile neutrinos are relaxed for fully resonantly produced sterile neutrinos in several of the cosmologies we considered, including the standard one for a lepton asymmetry larger than $\sim 10^{-5}$. This allows for the results reported from the LSND, and MiniBooNE short-baseline as well as the DANSS and NEOS reactor neutrino experiments to be unrestricted by cosmology. Furthermore, sterile neutrinos in this mass-range are also within the reach of the KATRIN and PTOLEMY experiments.

CHAPTER 3

Gas Heating Bounds on Primordial Black Holes

3.1 Introduction

Primordial black holes (PBH) can form in the early Universe through a variety of mechanisms and can significantly contribute to DM (e.g. [77, 78, 79, 80, 81, 82, 83, 84, 85, 86, 87, 88, 28, 89, 90, 91, 92, 93, 94, 95, 96, 34, 97, 98, 99, 100]). PBH surviving till present day can span many orders of magnitude in mass, ranging from 10^{15} g to well over 10^{10} $M_{\odot}$, depending on formation mechanism. Recent studies [218, 219, 220] of PBH in the mass window of $\sim 10^{-16} - 10^{-10} M_{\odot}$ have established that there is a sizable open parameter space for PBH to constitute all of the DM. Furthermore, PBH have been associated with a variety of astrophysical phenomena, such as seeds for formation of super-massive black holes [101, 102, 103] as well as the source of new signals [221, 222, 223] from compact star disruptions from PBH capture, among others.

With the detection of LIGO gravitational wave events [224, 225, 226], particular interest has been paid to the PBH from the intermediate mass window of $10 - 10^3 M_{\odot}$ that have also been suggested as possible progenitors (e.g. [227, 103, 228, 229, 230, 231, 232]). While a a variety of constraints exist for this PBH mass range (see e.g. [1]), they often rely on multiple assumptions and are subject to significant uncertainties. It is thus important to consider independent sources of constraints.

Here we establish novel constraints from PBH in the intermediate mass range $\sim 10 - 10^6 M_{\odot}$ traversing interstellar medium and heating the surrounding gas. We consider a variety of gas systems as well as several generic heating mechanisms, including dynamical friction, accretion disk emission as well as mass outflows/winds from accretion disk. Previously, constraints for passing massive BHs "heating" stars have been established [233, 234, 235], but gas heating effects have not been studied in detail. Theoretically expected luminous X-ray emission from traversing PBH interacting with surrounding medium has been also used to set limits [236, 28]. Recently, constraints from gas heating have been considered in the context of particle DM [237, 238, 239], which have different heating mechanisms compared to PBH. Furthermore, while the interest for particle DM is on systems with high relative particle velocity to ensure high collision rates, for PBH systems with slower relative velocities are preferential as this leads to increased PBH accretion and emission.

In addition to the intermediate mass PBH, we also consider light PBH with mass $\lesssim 10^{-16} M_\odot$ existing at present time, which will be evaporating and copiously emitting particles through Hawking radiation [104]. Non-rotating PBH with masses below $2.5 \times 10^{-19} M_\odot$ have lifetimes smaller than the age of the Universe and thus do not contribute to DM abundance [240, 241]. Particle emission from currently evaporating PBH produces a variety of signatures, providing insight into this region of PBH DM parameter space. Leading constraints on light PBH have been obtained from observations of photon flux [38, 39, 242, 43], cosmic microwave background [37, 243, 244, 245], electron and positron cosmic rays [36], 511 keV gamma-ray line [246, 247, 248, 249, 40, 41, 42], as well as neutrinos [42].

Usually, PBH are assumed to be non-rotating (Schwarzschild) [250, 251, 252]. However, PBH can be formed[1] with significant spin (Kerr BHs) [254, 255, 93, 256, 94, 99, 95]. BH spin will affect the Hawking radiation, generally increasing the emission while favoring particles with larger spin [104, 257, 241, 258]. Furthermore, the mass limit of $\sim 2.5 \times 10^{-19} M_\odot$ for PBH below which their lifetime is smaller than the age of the Universe varies by a factor of ~ 2 for maximally rotating PBH [257, 259, 260]. Besides mass (and electric charge), angular momentum constitutes a fundamental conserved parameter of a BH. Hence, it is important to explore the implications of spin for observations [242, 259, 261, 260, 262, 42].

Subsequent to our work on intermediate mass PBH, Ref. [263] considered heating of ISM gas due to light evaporating non-rotating PBH. We revisit and provide an alternative

[1]Heavier PBH can also efficiently acquire spin via accretion [253].

treatment of gas heating due to evaporating PBH, focusing again on the dwarf galaxy Leo T. We find that a more detailed, conservative, and proper treatment of energy deposition from PBH emission results in significantly weaker constraints than reported in the analysis of Ref. [263]. Furthermore, we study gas heating due to evaporating PBH with significant spin.

This chapter uses materials published in Refs. [69] and [43].

3.2 PBH in Interstellar Medium

3.2.1 Bondi-Hoyle-Lyttleton accretion

The accretion of gas onto floating BHs has been analyzed in Ref. [264] and applied to PBH in Ref. [28], whose arguments we follow. The process follows Bondi-Hoyle-Lyttleton accretion, with a rate of [98, 265, 266]

$$\dot{M} = 4\pi r_B^2 \tilde{v}\rho = \frac{4\pi G^2 M^2 n\mu m_p}{\tilde{v}^3} \,, \tag{3.1}$$

where M is the PBH mass, $r_B = GM/\tilde{v}^2$ is the Bondi radius[2], μ is the mean molecular weight, n is the ISM gas number density, m_p is the proton mass and $\tilde{v} \equiv (v^2 + c_s^2)^{1/2}$. Here, v is the relative PBH velocity to gas and c_s is the temperature-dependent sound speed in gas, which we take as $c_s \sim 10$ km/s [28]. Recent 3D hydrodynamical simulations show that the accretion rate at high Mach number would be limited to $\sim$ 10–20% of the canonical Bondi-Hoyle-Lyttleton accretion rate of Eq. (3.1) [267]. Since this depends on the assumed conditions and the dominant constraints in our study rely on low-velocity regime, throughout this work we adopt the canonical rate.

The BH accretion rate can be related to the bolometric emission luminosity as $L = \epsilon(\dot{M})\dot{M}$, with a scaling of radiative efficiency $\epsilon(\dot{M})$ describing different accretion regimes. The Eddington accretion rate, assuming a characteristic radiative efficiency of $\epsilon_0 = 0.1$[3], is

[2] Bondi radius sets the scale at which gravity becomes important and approximates how far from object material starts to be drawn in and accreted.

[3] The radiative efficiency ϵ_0 can vary from 0.057 for a non-rotating Schwarzschild BH to 0.42 for an

defined in terms of Eddington luminosity as

$$\dot{M}_{\rm Edd} = \frac{L_{\rm Edd}}{\epsilon_0 c^2} = 6.7 \times 10^{-16} \left(\frac{M}{M_\odot}\right) \; M_\odot/{\rm s} \; . \tag{3.2}$$

A convenient parameter for characterizing the accretion flow is

$$\dot{m} = \frac{\dot{M}}{\dot{M}_{\rm Edd}} = 2.64 \times 10^{-4} \left(\frac{M}{M_\odot}\right) \left(\frac{n}{1~{\rm cm}^{-3}}\right) \left(\frac{\mu}{1}\right) \left(\frac{\tilde{v}}{1~{\rm km/s}}\right)^{-3} \; . \tag{3.3}$$

3.2.2 Accretion disk formation

With a sufficient angular momentum, infalling gas can form accretion disk around the BH. For high accretion rates of $\dot{m} \gtrsim 0.07\alpha$, the accretion flow likely forms a thin α-disk, the so-called standard disk [269], where $\alpha \simeq \mathcal{O}(1)$ is a phenomenological parameter describing viscosity. The angular momentum necessary for disk formation can be supplied by perturbations in density or velocity of accreting gas. Due to density fluctuations in ISM described by Kolmogorov spectrum, a density differential between the opposite points on the accretion cylinder will supply angular momentum [270]. Equating this with Keplerian angular momentum, the outer edge of the resulting thin accretion disk is given by [264]

$$r_o \simeq 2.5 \times 10^6 r_s \left(\frac{M}{100 M_\odot}\right)^{\frac{2}{3}} \left(\frac{\tilde{v}}{100~{\rm km/s}}\right)^{-\frac{10}{3}} \; , \tag{3.4}$$

where $r_s = 2GM/c^2$ is the BH Schwarzschild radius. On the other hand, for inefficient accretion described by the Advection-Dominated Accretion Flow (ADAF) regime [271, 272], the inflowing matter does not follow Keplerian description. In that case, the outer accretion disk radius is uncertain and we consider a range of parameter values as described in Sec. 3.3.

For a Schwarzschild BH, the radius of innermost stable circular orbit (ISCO) of a test particle is $r_{\rm ISCO} = 3r_s$. If the outer edge of BH accretion disk is located within the ISCO radius, i.e. $r_o/r_{\rm ISCO} < 1$, we do not expect efficient disk formation. Thus, using Eq. (3.4) we can infer an approximate condition on BH mass for accretion disk formation as

$$M > 2.5 \times 10^{-8} M_\odot \left(\frac{\tilde{v}}{100~{\rm km/s}}\right)^5 \; . \tag{3.5}$$

---

extremal Kerr BH (see e.g. Ref. [268]).

3.2.3 Gas and PBH distribution

For PBH constituting a fraction of DM $f_{\rm PBH}$, the total number of PBH of mass M within a gas system of volume V and approximately constant DM density $\rho_{\rm DM}$ is

$$N_{\rm PBH}(M) = f_{\rm PBH} \frac{\rho_{\rm DM} V}{M} \ . \tag{3.6}$$

Here we assume a monochromatic PBH mass function for simplicity. The velocity of PBH contributing to DM can be described by a Maxwell-Boltzmann distribution

$$f(v) = \sqrt{\frac{2}{\pi}} \frac{v^2}{\sigma_v^3} \exp\left(-\frac{v^2}{2\sigma_v^2}\right) \ , \tag{3.7}$$

where σ_v is the velocity dispersion within a given system. Considering also a possible distribution in gas number density described by $f(n)$, analysis of resulting X-ray emission luminosity for a set of Milky Way gas clouds has been carried out in Ref. [264, 28].

As we will be interested in gas heating due to PBH, for a gas system in thermal equilibrium the total amount of heating from PBH of mass M is

$$H_{\rm tot}(M) = N_{\rm PBH}(M) H(M) = \int_{n_{\rm min}}^{n_{\rm max}} \int_{v_{\rm min}}^{v_{\rm max}} dn dv \frac{df_n}{dn} \frac{df_v}{dv} \mathcal{H}(M, n, v) \ , \tag{3.8}$$

where df_n/dn is the gas density distribution, df_v/dv is the relative PBH velocity distribution and $\mathcal{H}(M, n, v)$ is the amount of heat being deposited into the system from a single PBH (taking into account absorption). Here, $\mathcal{H}$ represents the cumulative contribution from all three considered heating processes and for photon emission and outflows there is an additional integration to treat absorption. Envisioning gas systems of approximately constant density, df_n/dn is simply a delta function.

A considered gas system can have a bulk relative velocity v_b with respect to the galactic frame. As shown in Appendix 4.3, this can be incorporated into our analysis via modification of Eq. (3.7) to

$$f(v) = \frac{v}{\sqrt{2\pi}\sigma v_b} \left[e^{-\frac{(v-v_b)^2}{2\sigma^2}} - e^{-\frac{(v+v_b)^2}{2\sigma^2}} \right] \ . \tag{3.9}$$

3.3 Gas Heating Mechanisms

We consider three distinct gas heating mechanisms due to PBH[4]: absorption of emitted photons from accretion disk, direct heating due to dynamical friction and energy deposit from emitted protons of outflows that are inherent to the ADAF accretion regime. Of these three, dynamical friction has the least uncertainty but typically forms a subdominant contribution.

3.3.1 Accretion photon emission

We first consider gas heating due to photon emission from accretion. Emission in the X-ray band will typically constitute the most dominant contribution and becomes more efficient at high mass accretion rates.

To characterize the accretion flow, we follow the scheme outlined in Ref. [272]. Namely, we consider that the accretion flow results in a thin disk for $\dot{m} > \dot{M} = 0.07\alpha$, and is described by ADAF for less efficient accretion. We do not consider slim disk or other solutions for near- or super-Eddington accretion $\dot{m} \sim 1$ as the PBH in our parameter space rarely achieve such high rates. Furthermore, the slim disk spectrum is not significantly different from the thin disk spectrum for $\dot{m} \lesssim 10$ [273]. In Fig. 3.1, we display dominant photon emission from accreting PBH over a wide PBH mass-range and for different densities of surrounding gas, assuming Bondi-Hoyle-Lyttleon accretion of Eq. 3.1 with characteristic flow velocity of $\tilde{v} \simeq 10$ km/s and also emission results of Sec. 3.3.1.1 and Sec. 3.3.1.2.

Hydrogen gas is optically thin to continuum emission below the ionization threshold of $E_\mathrm{i} = 13.6$ eV, and the velocity dispersion is not high enough for a significant Doppler broadening of the emission spectra. Thus, we ignore the absorption of photons with energies less than E_i. If the medium is optically thick to emitted photons, this signifies that photons are absorbed and we treat deposited energy as heating. For absorption, we employ photo-

[4]Since for relevant parameters of interest the BHs are large, the heating associated with Hawking evaporation is negligible in considered BH mass-range.

ionization cross-section of Ref. [274, 275] that is valid for $E > E_i$,

$$\sigma(E) = \sigma_0 y^{-\frac{3}{2}} \left(1 + y^{\frac{1}{2}}\right)^{-4} , \tag{3.10}$$

where $y = E/E_0$, $E_0 = 1/2E_i$ and $\sigma_0 = 605.73$ Mb $= 6.06 \times 10^{-16}$ cm^2. The optical depth for a gas system of size l and density n is then given by $\tau(n, E) = \sigma(E)nl$. Above 30 eV, we use the combined attenuation length data from Fig. (32.16) of Ref. [276].

The resulting heating power due to accretion emission photons is

$$\mathcal{H}(M, n, v) = \int_{E_i}^{E_{\max}} L_\nu(M, n, v) \left(1 - e^{-\tau}\right) d\nu , \tag{3.11}$$

where $\tau(n, E) = \sigma(E)nl$ is the optical depth for a gas system of size l and density n. For both ADAF and thin disk regimes the emission spectrum is exponentially decreasing at high energies and we evaluate the integral up to the maximum temperature $E_{\max}$, above which the contributions are negligible[5].

3.3.1.1 Thin disk

The standard (geometrically) thin α-disk, characterized by the viscosity parameter α, is optically thick and efficiently emits blackbody radiation [269]. Thin disk allows for a fully analytic description. The temperature of the disk varies with radius as [277]

$$T(r) = T_i \left(\frac{r_i}{r}\right)^{3/4} \left[1 - \left(\frac{r_i}{r}\right)^{\frac{1}{2}}\right]^{\frac{1}{4}} , \tag{3.12}$$

where σ is the Stefan-Boltzmann constant and r_i is the inner disk radius taken to be the ISCO radius $r_{\rm ISCO}$. Here, using Eq. (3.1),

$$T_i = \left(\frac{3GM\dot{M}}{8\pi r_i^3 \sigma}\right)^{1/4} = 300 \text{ eV} \left(\frac{n}{1 \text{ cm}^{-3}}\right)^{\frac{1}{4}} \left(\frac{\tilde{v}}{1 \text{ km/s}}\right)^{-\frac{3}{4}} . \tag{3.13}$$

The disk temperature is seen to be independent of the BH mass in the case of Bondi-Hoyle accretion. The disk temperature $T(r)$ decreases at large radii as $r^{-3/4}$, but also diminishes

[5]For thin disk, we choose the maximum temperature to be $E_{\max} = 5T_i$, where T_i is the characteristic temperature of the inner disk. For ADAF, we take $E_{\max} = 3T_e$, with T_e being the temperature of the electron plasma.

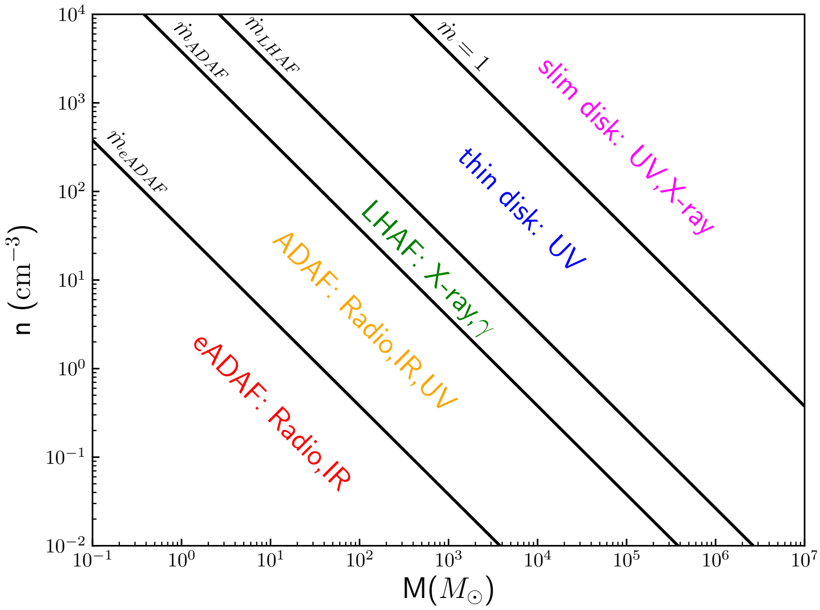

Figure 3.1: Dominant photon emission from PBH accretion over a wide PBH mass-range M for different densities of the surrounding gas n, assuming Bondi-Hoyle-Lyttleton accretion and a characteristic flow velocity of $\tilde{v} \simeq 10$ km/s in Eq. (3.1). Regions of different accretion regimes $\dot{m}$ (black diagonal lines) resulting in slim disk, thin disk and ADAF (including LHAF, ADAF, eADAF sub-regimes) accretion flows (see text) are shown.

near the inner radius. The disk attains a maximum temperature of $T_{\rm max} = 0.488 T_i$ at a radius of $r = 1.36 r_i$.

The thin disk emission spectrum is a combined contribution of the blackbody spectra from each radii. Using the scaling relations in Ref. [277] and requiring continuity, the resulting spectrum can be approximately described as

$$\begin{aligned} \nu < T_o: \qquad & L_\nu = c_\alpha \left(\frac{T_{\rm max}}{T_o}\right)^{\frac{5}{3}} \left(\frac{\nu}{T_{\rm max}}\right)^2 \\ T_o < \nu < T_{\rm max}: \qquad & L_\nu = c_\alpha \left(\frac{\nu}{T_{\rm max}}\right)^{\frac{1}{3}} \\ T_{\rm max} < \nu: \qquad & L_\nu = c_\alpha \left(\frac{\nu}{T_{\rm max}}\right)^2 e^{1-\frac{\nu}{T_{\rm max}}} \end{aligned} \tag{3.14}$$

where $c_\alpha = 2.26 \times 10^{31}$ erg eV^{-1}s$^{-1}(M/M_\odot)^2(n/1 \text{ cm}^{-3})^{3/4}(\tilde{v}/1 \text{ km/s})^{-9/4}$. Here c_α is normalized so that the total integrated luminosity $\int L_\nu d\nu = 0.057\dot{M}c^2$, i.e. emission is at the maximum possible efficiency for a Schwarzschild black hole. Using Eq. (3.1), (3.4) and (3.12), the temperature at the outer disk radius $T_o = T(r_o)$ is given by

$$T_o \simeq 1.09 \times 10^{-6} \text{ eV} \left(\frac{n}{1 \text{ cm}^{-3}}\right)^{\frac{1}{4}} \left(\frac{M}{M_\odot}\right)^{-\frac{1}{2}} \left(\frac{\tilde{v}}{1 \text{ km/s}}\right)^{\frac{7}{4}} . \tag{3.15}$$

For all relevant parameter values of interest for $n, M, \tilde{v}$, the temperature is always $T_o \ll 13.6$ eV. Hence, we only need to consider the temperature regimes when $T_o < \nu$.

From Eq. (3.13) it is seen that thin disks will efficiently emit in X-rays, a regime where the hydrogen ionization cross section is large. Hence, emission from thin disks will also efficiently absorbed and they can contribute significantly to gas heating.

3.3.1.2 ADAF disk

When the accretion is significantly sub-Eddington, advection-dominated accretion flow (ADAF) forms [271, 272]. Here, the heat generated by viscosity during accretion is not efficiently radiated out and much of the energy is advected via matter heat capture into the BH event horizon along with the gas inflow. In contrast to the thin disk, ADAF "disk" is geometrically thick and optically thin.

ADAF disk results in a complicated multi-component emission spectrum. We will consider three components of the ADAF spectrum, arising from electron cooling[6]: synchrotron radiation, inverse Compton (IC) scattering and bremsstrahlung.

To describe ADAF spectrum, we will employ approximate analytic expressions obtained in Ref. [279] in combination with the updated values for the phenomenological input parameters. The accretion inflow forms a hot two-temperature plasma [280], with the hotter ions at $T_{\rm ion} \simeq 10^{11} K$ and the cooler, radiating electrons with $T_e \simeq 10^9 - 10^{10} K$. We consider the temperature to be spatially uniform over the entire emission region. To characterize the flow, we use the following parameter values consistent with recent numerical simulations and

[6] We neglect additional possible contribution of synchrotron radiation from non-thermal electrons, which is present in ADAF models of Sgr A* [278].

observations [272]: the ratio of direct viscous heating to electrons and ions $\delta = 0.1 - 0.5$, the ratio of gas pressure to total pressure $\beta = 10/11$, the minimum flow radius is the ISCO radius with $r_{\rm min} = 3r_s$, and the viscosity parameter $\alpha = 0.1$. Furthermore, we use variable $x_M \simeq 4 \times 10^3 \dot{m}^{1/4}$ and constants $c_1 = 0.5$, $c_3 = 0.3$ as defined in Ref. [279].

For a more robust analysis, we will further sub-divide ADAF into three distinct regimes, depending on the accretion rate, following Ref. [272]. Namely, we shall consider luminous hot accretion flow (LHAF) for accretion rates $\dot{M}_{\rm ADAF} = 0.1\alpha^2 < \dot{m} < \dot{M}_{\rm LHAF} = 0.07\alpha$, standard ADAF in the range $10^{-3}\alpha^2 = \dot{M}_{\rm eADAF} < \dot{m} < \dot{M}_{\rm ADAF}$, and "electron" ADAF (eADAF) for $\dot{m} < \dot{M}_{\rm eADAF}$. As discussed in below and in detail in Appendix 4.4, the temperature determination is handled differently for each of these ADAF regimes.

The synchrotron emission is self-absorbed and produces a rising $L_\nu \propto \nu^{2/5}$ spectrum, similar to the $\nu^{1/3}$ spectrum in the optically thin regime and also to that of the thin disk, which peaks at

$$\nu_p = 1.83 \times 10^{-2}\ {\rm eV} \left(\frac{\alpha}{0.1}\right)^{-\frac{1}{2}} \left(\frac{1-\beta}{1/11}\right)^{\frac{1}{2}} \theta_e^2 \left(\frac{r_{\rm min}}{3r_s}\right)^{-\frac{5}{4}} \left(\frac{M}{M_\odot}\right)^{-\frac{1}{2}} \left(\frac{\dot{m}}{10^{-8}}\right)^{\frac{3}{4}} , \tag{3.16}$$

where

$$\theta_e = \frac{kT_e}{m_e c^2} = \frac{T}{5.93 \times 10^9 K} \tag{3.17}$$

is the temperature in units of the electron mass m_e. The peak luminosity is given by

$$L_{\nu_p} = 5.06 \times 10^{38} \frac{\rm erg}{\rm s \cdot eV}\ \alpha^{-1}(1-\beta) \left(\frac{M}{M_\odot}\right) \dot{m}^{\frac{3}{2}} \theta_e^5 r_{\rm min}^{-\frac{1}{2}} . \tag{3.18}$$

The total resulting synchrotron power is

$$P_{\rm syn} = \int_0^{\nu_p} L_\nu d\nu \simeq 0.71 \nu_p L_{\nu_p} . \tag{3.19}$$

For our typical parameters of interest, the synchrotron emission is poorly absorbed by the surrounding medium since it peaks well below the hydrogen ionization threshold. Therefore, it does not significantly contribute to gas heating.

The synchrotron photons undergo inverse-Compton scattering with the surrounding electron plasma. The thermal IC spectrum can be well approximated by a power law in the frequency range $\nu_p \leq \nu \lesssim 3T_e$ as

$$L_{\nu,\mathrm{IC}} = L_{\nu_p} \left(\frac{\nu}{\nu_p}\right)^{-\alpha_c} , \tag{3.20}$$

where

$$\alpha_c = -\frac{\ln \tau_{es}}{\ln A} . \tag{3.21}$$

The exponent α_c depends on the electron scattering optical depth $\tau_{es} = 12.4\dot{m}\alpha^{-1}r_{\mathrm{min}}^{-1/2}$ and the amplification factor (mean amplification per scattering) $A = 1 + 4\theta_e + 16\theta_e^2$. The total IC power

$$P_{\mathrm{IC}} = \int_{\nu_p}^{3T_e} L_{\nu,\mathrm{IC}} d\nu = \frac{\nu_p L_{\nu_p}}{1-\alpha_c} \left(\left[\frac{6.25 \times 10^7 \left(\frac{T_e}{10^9\ \mathrm{K}}\right)}{\left(\frac{\nu_p}{10^{12}}\right)} \right]^{1-\alpha_c} - 1 \right) \tag{3.22}$$

is sensitive to the considered temperature due to T^5 dependence of L_{ν_p} and the dependence implicit in α_c.

Depending on the accretion rate, different components of the ADAF spectrum can dominate. At low mass accretion rates (eADAF regime), the exponent in IC luminosity becomes $\alpha_c > 2$, resulting in $P_{\mathrm{IC}} \simeq P_{\mathrm{syn}}/0.71(\alpha_c - 1)$, and the IC power is a fraction of the synchrotron power. For moderate accretion (ADAF regime), $1 < \alpha_c \lesssim 2$ and while IC power is the dominant emission component synchrotron emission is still comparable. At the highest accretion rates right below the thin disk threshold (LHAF regime), $\alpha_c < 1$ the IC radiation becomes highly efficient. See Appendix 4.4 for details of how temperature θ_e is treated for each regime.

The third component of the ADAF emission spectrum comes from bremsstrahlung of the thermal electrons, which provides a flat spectrum with an exponential drop at T_e

$$\begin{aligned} L_{\nu,\mathrm{brems}} = 1.83 \times 10^{17} \left(\frac{\alpha}{0.1}\right)^{-2} \left(\frac{c_1}{0.5}\right)^{-2} \ln\left(\frac{r_{\mathrm{max}}}{r_{\mathrm{min}}}\right) F(\theta_e) \\ \left(\frac{T_e}{5 \times 10^9\ \mathrm{K}}\right)^{-1} e^{-\frac{h\nu}{kT_e}} m\dot{m}^2 \ \mathrm{ergs\ s^{-1}Hz^{-1}} , \end{aligned} \tag{3.23}$$

where r_{max} is $\mathcal{O}(10^3)$ and where $F(\theta_e)$ is $\mathcal{O}(1)$ given by

$$F(\theta_e) = \begin{cases} 4\left(\frac{2\theta_e}{\pi^3}\right)^{\frac{1}{2}} (1 + 1.78\theta_e^{1.34}) + 1.73\theta_e^{\frac{3}{2}}(1 + 1.1\theta_e + \theta_e^2 - 1.25\theta_e^{\frac{5}{2}}), & \theta_e \leq 1 , \\ \left(\frac{9\theta_e}{2\pi}\right) (\ln[1.12\theta_e + 0.48] + 1.5) + 2.30\theta_e(\ln[1.12\theta_e] + 1.28), & \theta_e \geq 1 . \end{cases} \tag{3.24}$$

While bremsstrahlung produces the majority of hard X-rays and gamma rays, IC typically generates more power in the relevant range of high electron optical depth 10 eV $\sim$ 100 eV. Since the total bremsstrahlung power is also negligible relative to the combined synchrotron and IC power in the relevant parameter space, it will thus not contribute significantly to gas heating.

3.3.2 Dynamical friction

Dynamical friction due to gravitational interactions of traversing PBH with surrounding medium can both heat the gas and change the PBH velocity distribution. In contrast to photon emission and outflows, dynamical friction has the advantage of directly depositing kinetic energy and heating the gas without additional considerations of attenuation length for emitted particles and stopping power.

While some of the other heating mechanisms we have considered contain a high degree of uncertainty, dynamical friction follows a straightforward description via "gravitational drag" force given by [281]

$$\begin{aligned} F_{\rm dyn} &= -\frac{4\pi G^2 M^2 \rho}{v^2} I \\ &= -3.95 \times 10^{12}\ \mathrm{N} \left(\frac{M}{M_\odot}\right)^2 \left(\frac{\rho}{1\ \mathrm{GeV\ cm^{-3}}}\right) \left(\frac{v}{10\ \mathrm{km\ s^{-1}}}\right)^{-2} I\ , \end{aligned} \tag{3.25}$$

where I is a velocity-dependent geometrical factor. For collisionless medium, such as DM, this factor takes the form of

$$I_{\rm col} = \ln\left(\frac{r_{\rm max}}{r_{\rm min}}\right) \left[\mathrm{erf}\left(\frac{v}{\sqrt{2}\sigma}\right) - \frac{2v}{\sqrt{2\pi}\sigma} e^{-\frac{v^2}{2\sigma^2}}\right]\ , \tag{3.26}$$

where σ is the (DM) velocity dispersion, $r_{\rm max}$ denotes the size of the surrounding affected system that we identify with the gas cloud size and $r_{\rm min}$ is the size of the perturbing body, which we take to be the Schwarzchild radius of the BH. For a gaseous medium, I depends on the mach number $\mathcal{M} = v/c_s$, where c_s is the medium sound speed, and whether the motion of the perturbing PBH is subsonic ($\mathcal{M} < 1$) or supersonic ($\mathcal{M} > 1$) [282]

$$I = \begin{cases} \frac{1}{2}\ln\left(\frac{1+\mathcal{M}}{1-\mathcal{M}}\right) - \mathcal{M}, & \mathcal{M} < 1 \ , \\ \frac{1}{2}\ln\left(1 - \frac{1}{\mathcal{M}^2}\right) + \ln\left(\frac{r_{\rm max}}{r_{\rm min}}\right), & \mathcal{M} > 1 \ . \end{cases} \tag{3.27}$$

The resulting output power due to dynamical friction for PBH traversing gas, which in this case is also $\mathcal{H}$ as the gas is directly heated, is

$$P_{\rm dyn} = F_{\rm dyn} v = 3.95 \times 10^{23}\ {\rm erg\ s^{-1}} \left(\frac{M}{M_\odot}\right)^2 \left(\frac{\rho}{1\ {\rm GeV\ cm^{-3}}}\right) \left(\frac{v}{10\ {\rm km\ s^{-1}}}\right)^{-1} I \ . \tag{3.28}$$

We can estimate the change in PBH velocity due to dynamical friction using Eq. (3.26). Envisioning applying our results to dwarf galaxies, let us consider a gaseous system with DM density $\rho_{\rm DM}$ in the central region of the system that is significantly higher than the gas density $\rho = n m_p$. The effect of dynamical friction on PBH velocity can be seen from comparing the total work done on the PBH traversing the system to its kinetic energy

$$\frac{F_{\rm dyn} r_{\rm max}}{\frac{1}{2} M v^2} = -6.13 \times 10^{-7} \left(\frac{M}{M_\odot}\right) \left(\frac{\rho}{1\ {\rm GeV\ cm^{-3}}}\right) \left(\frac{v}{10\ {\rm km\ s^{-1}}}\right)^{-4} \left(\frac{r_{\rm max}}{500\ {\rm pc}}\right) I \ . \tag{3.29}$$

The effect on PBH velocity is insignificant throughout most of the parameter space of interest, unless we consider gaseous environments of significantly higher density (in either gas or DM) or super-massive PBH with mass $M \gtrsim 10^5 M_\odot$. We therefore ignore dynamical friction effect on PBH velocity. We note that lower relative velocities will generally increase the PBH accretion rate, resulting in an increase of the photon and outflow power delivered to the gaseous system. Hence, ignoring the velocity modification yields more conservative bounds on PBH gas heating.

3.3.3 Accretion mass outflows/winds

Mass outflows (winds) composed of protons can also contribute to the heating of surrounding medium by PBH and are expected to be significant for hot accretion flows [272]. In contrast to jets[7], the outflows are not highly relativistic and cover wider angular distribution. There is significant uncertainty in description of outflows.

[7] As jets are typically associated with Kerr black holes, they would require a separate treatment and we do not consider them here.

The outflows reduce accretion rate at smaller radii and can be approximately modelled by a self-similar power-law form [283]

$$\dot{M}_{\rm in}(r) = \dot{M}_{\rm in}(r_{\rm out}) \left(\frac{r}{r_{\rm out}}\right)^s , \tag{3.30}$$

where index $0 \leq s < 1$ is limited by energy and mass conservation. Here, $\dot{M}_{\rm in}(r_{\rm out})$ is the Bondi-Hoyle-Lyttleton accretion rate of Eq. (3.1). The corresponding outflow (wind) is [284]

$$\dot{M}_w(r) = r\frac{d\dot{M}_{\rm in}}{dr} = s\dot{M}_{\rm in}(r_{\rm out}) \left(\frac{r}{r_{\rm out}}\right)^s . \tag{3.31}$$

From simulations, the exponent s is seen to be $0.4 - 0.8$ [285, 272]. The outer radius $r_{\rm out}$ has been considered in the literature over a wide range of values, including $100r_s$ [286], $500r_s$ [285], r_B [287], to $10r_B$ [288]. The resulting outgoing wind has a velocity that is a fraction $f_k \simeq 0.1 - 0.2$ [288, 289, 285] of the Keplerian velocity at the radius at which it is ejected (due to Be/v_k^2 being roughly constant) [285]), i.e. $v(r) \simeq f_k\sqrt{GM/r}$. Most of the kinetic energy of the wind comes from the inner region, with the kinetic energy per particle determined at the ISCO radius with $v_{\rm in} = v(r_{\rm in} = 3r_s)$ being

$$E_{\rm kin} \simeq \frac{1}{2}m_p v_{\rm in}^2 = 782 \text{ keV} \left(\frac{r_{\rm in}}{3r_s}\right)^{-1} \left(\frac{f_v}{0.1}\right)^2 , \tag{3.32}$$

which is independent of PBH mass.

To evaluate how much energy is deposited into the gas system from streaming outflow protons, we derive the energy distribution of the wind, $f(E)$, and convolute it with the heat generated per proton ΔE. Using the values of the stopping power $dE/dx = nS(E)$ adopted from Ref. [290] (see their Fig. 9),

$$\Delta E = \int \frac{dE}{dx}dx \simeq \min(E, nS(E)r_{\rm max}) . \tag{3.33}$$

The total heat deposited in the cloud is then

$$\mathcal{H}_{\rm outflow} = \int_{r_{\rm in}}^{r_{\rm out}} \Delta E \frac{\mathcal{D}}{\mu m_p}\frac{d\dot{M}_{\rm in}}{dr}dr = \int_{E(r_{\rm min})}^{E(r_{\rm out})} \Delta E f(E) dE , \tag{3.34}$$

where the distribution function is given by

$$
\begin{aligned}
f(E) &= s\dot{M}_{\rm in}(r_{\rm out})\left(\frac{r}{r_{\rm out}}\right)^s \frac{1}{E} \\
&= 3.54\times 10^{25}\ \frac{\rm erg}{\rm eV^2\ sec}\ s(2.35\times 10^8)^s \left(\frac{M}{M_\odot}\right)^2 \left(\frac{n}{1\ {\rm cm}^{-3}}\right) \\
&\times \left(\frac{\tilde{v}}{1\ {\rm km/s}}\right)^{-3} \left(\frac{\mathcal{D}}{0.1}\right) \left(\frac{r_{\rm out}}{r_s}\right)^{-s} f_v^{2s} E^{-s-1}\ .
\end{aligned}
\tag{3.35}
$$

and we have also included an outflow duty cycle penalty factor $\mathcal{D} \simeq 0.1$ [291].

3.4 Astrophysical Systems

We now apply our analysis to several example astrophysical systems, Milky Way gas clouds and dwarf galaxies. We stress, however, that our methods can be readily applied to other systems as well. To constrain PBH mass fraction $f_{\rm PBH}$, we consider the balance between heating and cooling processes of the gas system. Our approach to set limits is similar the one used for particle DM [237, 238, 239], but the heating mechanisms and preferred gas systems are different compared to our study of PBH.

For simplicity, we ignore the contribution of natural heating sources (e.g. stellar radiation) and hence our bounds are conservative. Requiring thermal equilibrium, we only consider gas systems that are expected to be approximately stable on sufficiently long timescales $\tau_{\rm sys}$. Hence, the characteristic time over which the gas system remains steady must be greater than the cooling timescale of the gas $\tau_{\rm therm}$

$$
\tau_{\rm sys} \gg \tau_{\rm therm} = \frac{3nkT}{2\dot{C}}\ , \tag{3.36}
$$

where k is the Boltzmann constant and $\dot{C}$ is the gas cooling rate per volume.

In principle a multitude of processes can participate in gas temperature exchange, and a detailed analysis involving a full chemistry network can be performed using numerical methods [292]. For parameters of interest, we employ approximate results obtained in Ref. [239]. For hydrogen gas, the cooling rate is given by

$$
\dot{C} = n^2 10^{[{\rm Fe/H}]}\Lambda(T)\ , \tag{3.37}
$$

where [Fe/H]$\equiv \log_{10}(n_{\rm Fe}/n_{\rm H})_{\rm gas} - \log_{10}(n_{\rm Fe}/n_{\rm H})_{\rm Sun}$ is the metallicity, and $\Lambda(T) \propto 10^{\rm [Fe/H]}$ is the cooling function. Fitting numerically to the results of Ref. [292] library, Ref. [239] obtained $\Lambda(T) = 2.51 \times 10^{-28} T^{0.6}$, valid for 300 K $< T <$ 8000 K.

The total PBH heating in the cloud $H_{\rm tot} = N_{\rm PBH} H(M) = f_{\rm PBH}\rho_{\rm DM} V H(M)/M$ given by Eq. (3.8), where $H(M)$ is the average heat generated from one PBH of mass M, should be less than the total cooling $\dot{C}V$. This yields a condition on PBH abundance that we use to set our limits

$$f_{\rm PBH} < f_{\rm bound} = \frac{M\dot{C}}{\rho_{\rm DM} H(M)}~. \tag{3.38}$$

We note that the above argument involving thermal equilibrium only applies if, on average, there is at least one PBH in the gas system. This consideration results in a lower "incredulity" limit for our limits obtained from Eq. 3.38

$$f_{\rm bound} > \frac{3M}{4\pi r_{\rm sys}^3 \rho_{\rm DM}}~, \tag{3.39}$$

where $r_{\rm sys}$ is the size of the system.

3.4.1 Milky-Way gas clouds

A variety of interstellar neutral hydrogen (HI) gas clouds exist in the inner Galaxy within a few hundred pc of the Galactic plane [293]. In general, such Milky-Way clouds are not ideal candidates for analysing PBH due to the high relative rotational velocity, high velocity dispersion, and low total DM mass (relative e.g. to dwarf galaxies) due to their small size. The last of these shortcomings limits the maximum mass considered for PBH due to the incredulity limit of Eq. (3.39). Thus, even if a cloud had favorable properties otherwise, it would not be able to provide significant constraints in the intermediate PBH mass range.

To demonstrate our analysis, we consider as an example a particular Milky-May cloud, G33.4-8.0. To describe G33.4-8.0, we use parameters from Ref. [293, 294, 295, 296, 297, 298, 239]. Namely, the atomic hydrogen gas density is taken to be $n = 0.4 \pm 0.1$ cm^{-3}, cloud radius $r \simeq 30$ pc, bulk relative velocity $v_{\rm bulk} = 220$ km/s, temperature $T = 400 \pm 90$ K and corresponding adiabatic sound speed $c_s = 2.4$ km/s, and the cooling rate of $\sim 2.1 \times$

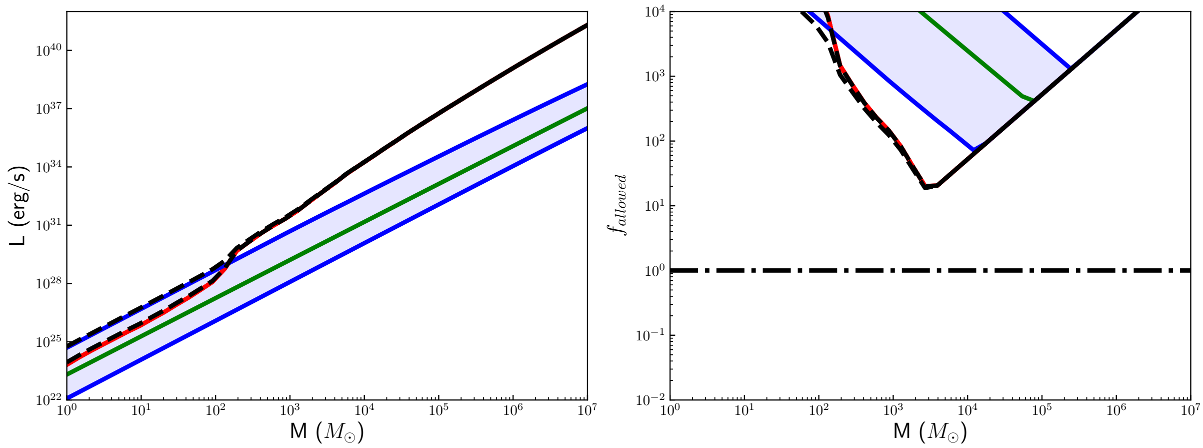

Figure 3.2: Left: The amount of heat absorbed by Milky-Way gas cloud G33.4-8.0 from a single PBH of mass M. Three heating components are shown: photon emission (red), dynamical friction (green), mass outflows (blue), as well as the total heat (black dashed). Both Model 1 and Model 2 of emission are shown, and the variation in the outflow luminosity is shaded in blue. The observed irregularities are due to transitions between the eADAF, ADAF, LHAF, and thin disk regimes. **Right:** Constraints from G33.4-8.0 on fraction of PBH contributing to the total amount of DM derived by from considerations of only photon emission (red), dynamical friction (green), mass outflows (blue), as well as combined (black dashed). The variation in the constraint from Models 1 and 2 are shaded in blue. The reach of constraints is bounded by the diagonal upward-going incredulity limit.

10^{-27} erg cm^{-3} s^{-1}. The DM density of the cloud is $\rho = 0.64$ GeV/cm^3, assuming Navarro-Frenk-White (NFW) profile, with the DM velocity dispersion of 124.4 km/s.

In Fig. 3.2, we display the heating from a single PBH for G33.4-8.0, including contributions due to photon emission, dynamical friction as well as mass outflows. Here, we numerically integrate Eq. (3.8). To treat the PBH emission as well as uncertainty, we consider two distinct input parameter sets[8] as shown in Tab. 3.1. The observed irregularities in the figure are due to transitions between the eADAF, ADAF, LHAF, and thin disk regimes.

[8] We do not consider a variation in PBH emission parameter δ between $0.1 - 0.5$ for our analysis, since it only corresponds to a $\mathcal{O}(\%)$ variation in the photon luminosity.

	δ	β	α	s	$r_{\rm outer}$	f_v	$\mathcal{D}$
Model 1	0.3	10/11	0.1	0.5	r_B	0.1	1
Model 2	0.3	10/11	0.1	0.7	$100r_s$	0.2	1

Table 3.1: Input parameters for PBH emission.

We also display in Fig. 3.2 combined resulting constraints for G33.4-8.0 from gas heating, bound by the incredulity limit

$$f_{\rm bound} > 5.25 \times 10^{-4} \left(\frac{M}{M_\odot}\right) \left(\frac{r_{\rm sys}}{30\ {\rm pc}}\right)^{-3} \left(\frac{\rho_{\rm DM}}{0.64\ {\rm GeV\ cm^{-3}}}\right)^{-1} . \tag{3.40}$$

Conversely, the largest PBH mass G33.4-8.0 can bound by this method is $1.9 \times 10^3 M_\odot$.

3.4.2 Dwarf galaxies

Dwarf DM-rich galaxies provide a good setting to study DM-gas heating. In contrast to Milky-Way gas clouds, their lack of additional relative bulk velocity as well as significant size that allows to extend the incredulity limit makes them favorable systems for PBH heating.

We will focus on Leo T, a transition type galaxy between dwarf irregular and spheroidal that is a few hundred kpc away from the Milky Way. Leo T has been well studied and modeled theoretically and with desired properties, such as a low baryon velocity dispersion that is also favorable for PBH heating.

The gas in the inner region of Leo T, $r \lesssim 350$ pc, is dominated by atomic hydrogen and highly ionized outside [299]. Since the free electrons in the ionized region cool very efficiently (see e.g. Ref. [292]), we limit our analysis to the central region of Leo T. From the model of Ref. [299], the hydrogen gas density is found to vary from $\sim 0.2\ {\rm cm^{-3}}$ in the center to $\sim 0.03\ {\rm cm^{-3}}$ at $r = 350$ pc. Both the cooling and heating rates scale roughly as n^2, so we approximate the gas density to be a constant $n = 0.07\ {\rm cm^{-3}}$ in the inner region. Similarly, the DM mass density drops from $\rho_{\rm DM} \simeq 4\ {\rm GeV/cm^3}$ at the center to $2\ {\rm GeV/cm^3}$ at $r = 350$ pc, which we approximate to be as a constant value of $1.75\ {\rm GeV/cm^3}$. The

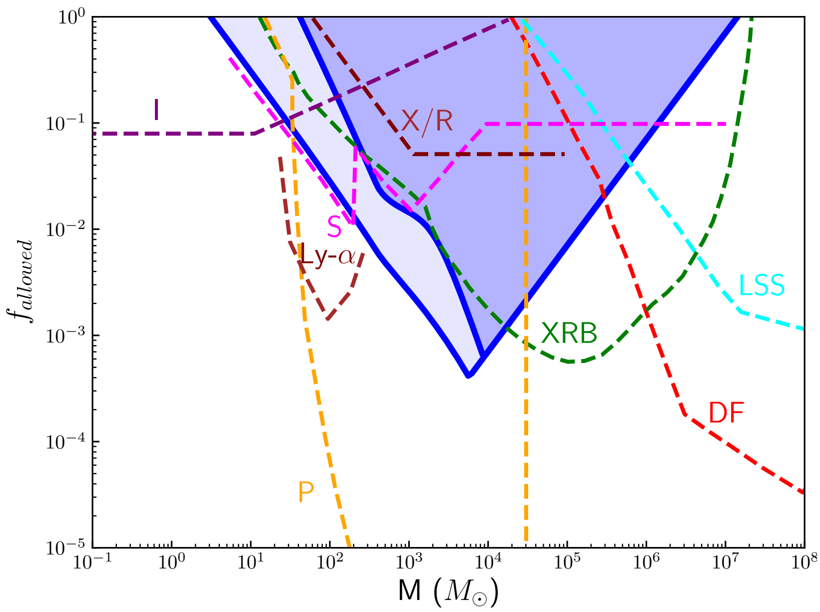

Figure 3.3: Constraints from Leo T dwarf galaxy on intermediate mass PBH gas heating are shown in blue. Light blue shaded band denotes variation in considered PBH emission parameters. These constraints are bounded by the PBH incredulity limit. Other existing constraints are shown by dashed lines, including Icarus [26] (I) in purple, Planck [27] (P) in yellow, X-ray binaries [28] (XRB) in green, dynamical friction of halo objects [29] (DF) in red, Lyman-α [30] (Ly-α) in maroon, combined bounds from the survival of astrophysical systems in Eridanus II [31], Segue 1 [32], and disruption of wide binaries [33] (S) shown in magenta, Large scale structure [34] (LSS) in cyan, and X-ray/radio [35] (X/R) in brown.

hydrogen gas has a dominant non-rotating warm component with a velocity dispersion of $\sigma_g = 6.9$ km/s and $T \simeq 6000$ K [300, 299] and also a sub-dominant cold component that we will ignore. The DM is expected to have the same velocity dispersion as the gas, $\sigma_v = \sigma_g$. The sound speed is taken to be $c_s = 9$ km/s from the adiabatic formula with $T \simeq 6000$ K. Combining the radius and number density, the column density of hydrogen gas in the central region of Leo T is $nr_{\rm sys} = 7.56 \times 10^{19}$ cm^{-2}. Using the above input parameters as well as metallicity of [Fe/H] $\simeq -2$ [301] in Eq. (3.37), the resulting Leo T's cooling rate is taken to be $\dot{C} = 2.28 \times 10^{-30}$ erg cm^{-3} s^{-1}.

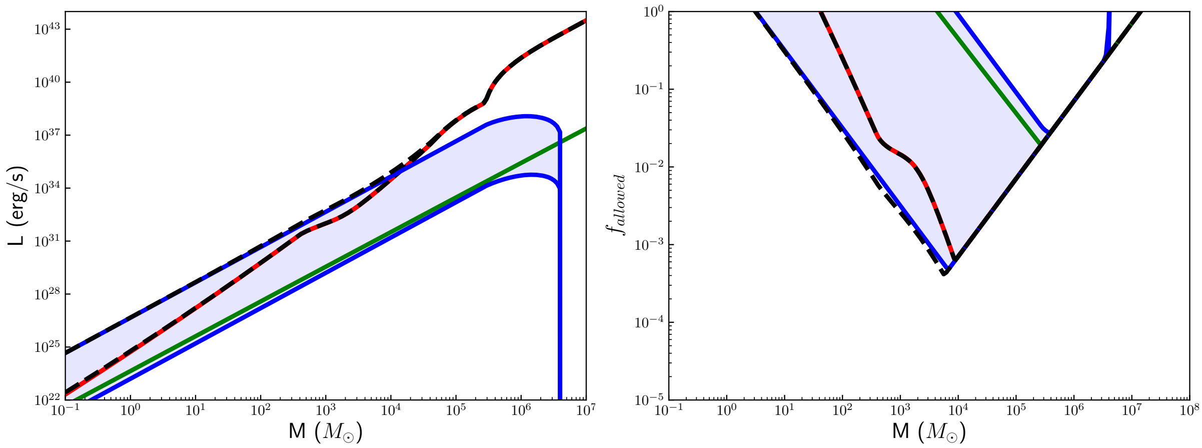

Figure 3.4: Left: The amount of heat absorbed by Leo T dwarf galaxy from a single PBH of mass M. Three heating components are shown: photon emission (red), dynamical friction (green), mass outflows (blue), as well as the total heat (black). The observed irregularities are due to transitions between the eADAF, ADAF, LHAF, and thin disk regimes. Both Model 1 and Model 2 of emission are shown, and the variation in the outflow luminosity is shaded in blue. **Right:** Constraints from Leo T on fraction of PBH contributing to the total amount of DM derived by from considerations of only photon emission (red), dynamical friction (green), mass outflows (blue), as well as combined (black). The reach of constraints is bounded by the diagonal upward-going incredulity limit. The variation in the constraint from Models 1 and 2 are shaded in blue. The black line shows the combined constraint from Model 2.

In Fig. 3.4, we display the heating from a single PBH for Leo T, including contributions due to photon emission, dynamical friction as well as mass outflows. As before, we numerically integrate Eq. (3.8) and consider PBH emission parameter variation as described in Tab. 3.1. We note that with Leo T parameters, the condition for thin disks, $\dot{m} > 0.07\alpha$, is satisfied only for very massive PBH $M \gtrsim 10^5 M_\odot$.

We also display in Fig. 3.4 the combined resulting constraints from gas heating for Leo T, bound by the incredulity limit given by

$$f_{\rm bound} > 7.05 \times 10^{-8} \left(\frac{M}{M_\odot}\right) \left(\frac{r_{\rm sys}}{350~\rm pc}\right)^{-3} \left(\frac{\rho_{\rm DM}}{1.75~\rm GeV~cm^{-3}}\right)^{-1} . \tag{3.41}$$

Conversely, the largest PBH mass Leo T can bound by this method is $1.42 \times 10^7 M_\odot$.

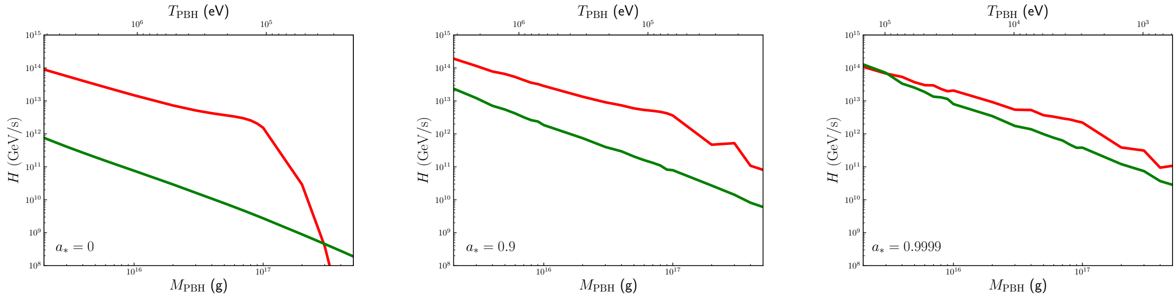

Figure 3.5: Emission components from evaporating PBH contributing to gas heating in Leo T, assuming PBH are non-rotating with $a_* = 0$ **[Left]**, PBH are spinning with $a_* = 0.9$ **[Middle]**, and PBH approaching the Kerr BH limit with spin $a_* = 0.9999$ **[Right]**. Contributions from primary photons (green line) and electrons/positrons (red line) are displayed.

3.5 Evaporating Black Hole Emission

An un-charged[9] rotating (Kerr) PBH radiates at a temperature given by [240, 257, 241, 304, 305, 306]

$$T_{\rm PBH} = \frac{1}{4\pi G M_{\rm PBH}}\left(\frac{\sqrt{1-a_*^2}}{1+\sqrt{1-a_*^2}}\right)\,, \tag{3.42}$$

where G is the gravitational constant, $M_{\rm PBH}$ and $a_* = J_{\rm PBH}/(G M_{\rm PBH}^2)$ are the PBH mass and reduced spin Kerr parameter, for a PBH with angular momentum $J_{\rm PBH}$. In the limit $a_* \to 0$, Eq. (3.42) reduces to the usual Hawking evaporation temperature of a Schwarzschild BH, $T_{\rm PBH} \simeq 1.1$ MeV $(M_{\rm PBH}/10^{16}{\rm g})^{-1}$. The temperature is seen to be significantly diminished for a Kerr BH in the limit $a_* \to 1$.

Evaporating PBH start to emit significant quantities of a given particle as the BH temperature reaches the particle mass, and at high temperatures the emission spectrum resembles that of blackbody radiation [240]. For spin-1/2 particles, the emission peak occurs at $E \simeq 4.03\, T_{\rm PBH}$ [306]. At lower BH masses, secondary emission channels due to quark and gluon QCD jets become relevant.

For primary emission, the number of particles, N_i, emitted per unit energy per unit time

[9]BHs with mass below $\lesssim 10^5 M_\odot$ are expected to rapidly lose any accumulated charge due to Schwinger pair production [302, 303].

is given by [240, 257, 241, 304, 305, 306]

$$\frac{d^2N_i}{dtdE} = \frac{1}{2\pi}\sum_{\text{dof}}\frac{\Gamma_i(E, M_{\text{PBH}}, a_*)}{e^{E'/T_{\text{PBH}}} \pm 1} , \tag{3.43}$$

where the greybody factor $\Gamma_i(E, M_{\text{PBH}}, a_*)$ encodes the probability that the emitted particle overcomes the gravitational well of the BH, E' is the total energy of a particle when taking BH rotation into account, the $\pm$ signs are for fermions and bosons, respectively, and summation is over considered degrees of freedom. Secondary emission of particles from QCD jets can be computed numerically [307].

For our study we generate the PBH emission spectrum for each particle species using the BlackHawk code[10] [308].

3.6 Gas Heating by Evaporating PBH

As proposed in Ref. [69], accretion emission from heavier PBH will deposit energy and heat the gas in surrounding interstellar medium. It was subsequently suggested that emitted particles from evaporating light PBH can also deposit energy and heat surrounding gas [263]. Below, we revisit gas heating due to non-rotating evaporating PBH with an improved treatment. We also extend our study of gas heating to emission from rotating evaporating PBH.

For our PBH masses of interest, both photon as well as electron/positron emission channels from evaporating PBH can contribute to heating. In Ref. [263], photon heating contribution has been assumed negligible due to power law scaling of photo-electric cross-section $\sigma_{\text{PE}} \propto E^{-3.5}$ when photon energies are above keV. However, for photon energies around MeV that are typical to our study, the cumulative photon interaction cross-section levels out, primarily due to Compton scattering contribution (see Fig. 33.19 of Ref. [9]). The average heating rate due to photon emission of PBH of mass M_{PBH} and spin a_* is given by [69]

$$H_\gamma(M_{\text{PBH}}, a_*) = \int_0^\infty f_h(E) E \frac{d^2N_\gamma}{dtdE}\left(1 - e^{-\tau}\right) dE , \tag{3.44}$$

[10] Results of numerical computation have been verified against semi-analytical formulas [240, 257, 241, 304].

where $f_h(E) \sim \mathcal{O}(1)$ is the fraction of photon energy loss deposited as heat, and $\tau = m_{\rm H} n_{\rm H} r_s/\lambda$ is the optical depth of gas in terms of the absorption length λ. We take the cumulative photon absorption length from Ref. [9]. We assume that the photon deposits heat similarly to electrons of the same energy. Hence, we approximate the fraction of energy deposited as heat to be similar to that of electrons, $f_h(E) = 0.367+0.395(11\ {\rm eV}/(E-m_e))^{0.7}$ [309, 310, 311, 263], where m_e is the electron mass. The efficiency of photon heating is rather poor, with the heat deposited within Leo T from characteristic MeV photons with $\lambda \simeq 10$ g/cm^2 being only $\sim 10^{-5}$ fraction of the photon energy.

Analogously to the photon case, heating due to PBH electron/positron emission can be stated as

$$H_e(M_{\rm PBH}, a_*) = 2\int_{m_e}^{\infty} f_h(E)[E-m_e]\frac{d^2N_e}{dtdE}\left(1-e^{-\tau}\right) dE\ , \tag{3.45}$$

where factor of 2 comes from summing contributions of electrons and positrons, $f_h(E)$ is taken as before and the factor $(1-e^{-\tau})$ accounts for the gas system's optical thickness. When the system is not optically thick, optical depth can be written in terms of stopping power, $S(E)$, as $\tau \simeq m_{\rm H} n_{\rm H} r_s S(E)/E$. For the electron stopping power on hydrogen gas, we use NIST database [312]. For characteristic MeV electrons with $S(E) \simeq 2$ MeV cm^2/g, only $\sim 10^{-4}$ fraction of the electron energy is deposited as heat in Leo T.

In Ref. [263] it was argued that for Leo T MeV scale energies are efficiently thermalized by elastic scattering within the cooling time scale. However, the suppression of gas heating in Eq. (3.45) from positrons and electrons, $(1-e^{-\tau})$, due to optical thickness of the gas system was not accounted for in the study of Ref. [263], effectively assuming that the gas is fully optically thick (i.e., $\tau \gtrsim 1$). This lead to significant overestimation of the limits from evaporating PBH gas heating than we find, as discussed below. Since the size of the gas system in consideration is finite and it can be optically thin, this factor should be present. We note that presence of magnetic fields in the ISM can also affect emitted positrons. However, the strength, orientation and distribution of magnetic fields in Leo T is highly uncertain and very poorly known. Furthermore, propagation of positrons can be affected in a non-trivial way by diffusion, collisions, advection, and other processes. Even in a relatively well-studied region like the Milky Way Galactic Center, the positron propagation distance is highly uncertain [313]. We expect such uncertainties to be present in Leo T too, especially in the absence of our understanding of the magnetic field, turbulence, and other astrophysical properties of that galaxy. Hence, our resulting bounds from PBH heating are conservative.

In Fig. 3.5 (left panel), we display the resulting heating rates $H(M_{\rm PBH}, a_*)$ for Leo T, including contributions of primary photons and electrons/positrons. Secondary emission of photons and electrons/positrons is negligible in our range of interest $M_{\rm PBH} \gtrsim 2 \times 10^{15}$ g, and hence is not shown[11]. Electrons/positrons are seen to provide the dominant contribution to heating rate within a broad range of parameter space of interest. Photons provide a sub-dominant contribution to the heating, but could in fact dominate in the regimes $T_{\rm PBH} \ll m_e$ (where electron emission is heavily suppressed).

We further analyze heating from spinning PBH, displaying results for $a_* = 0.9$ (Fig. 3.5, middle panel) and $a_* = 0.9999$ (Fig. 3.5, right panel). The emission for $a_* = 0$ and $a_* = 0.9$ is seen to be similar. As the spin approaches the extreme Kerr limit, $a_* \to 1$, the pattern of PBH emission and hence heating contributions changes. The emission tends to be higher for spinning PBH and for highly spinning PBH, photons can become dominant at smaller PBH masses, as they are produced in greater abundance than electrons [257].

[11] As discussed in recent work of Ref. [314], computation of secondary production by BlackHawk can be improved over some emission regimes.

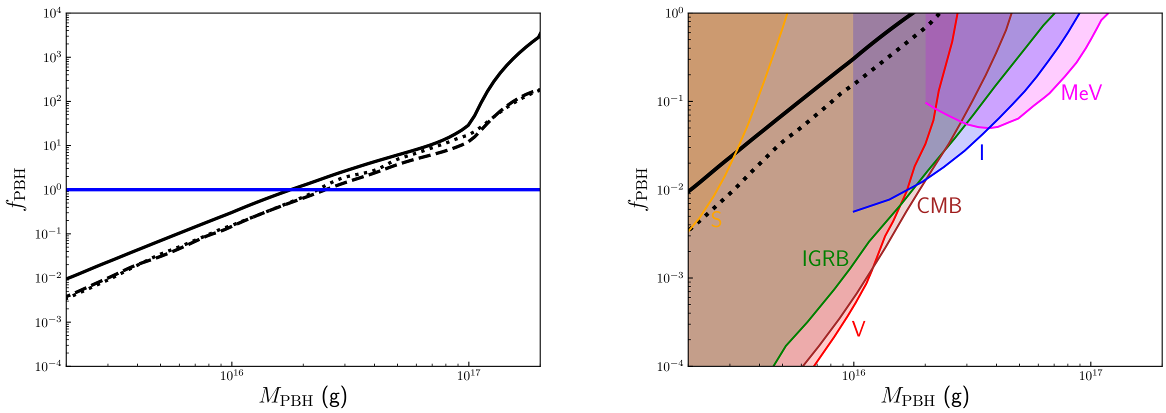

Figure 3.6: Constraints from Leo T on the fraction of DM PBH, $f_{\rm PBH}$, for a monochromatic PBH mass function. **[Left]** Results for non-rotating PBH with spin $a_* = 0$ (black solid line), PBH with spin $a_* = 0.9$ (black dashed line) and PBH approaching Kerr limit with $a_* = 0.9999$ (black dotted line) are shown. The "elbow" feature seen at the higher PBH masses is due to increased photon contribution. **[Right]** Overlay of our results with existing constraints on non-spinning PBH from *Voyager-1* detection of positrons and using propagation model B without background ("V", shaded red) [36], *Planck* cosmic microwave background ("CMB", shaded brown) [37], isotropic gamma-ray background ("IGRB", shaded green) [38, 39, 1], *INTEGRAL* 511 keV emission line for the isothermal DM profile with 1.5 kpc positron annihilation region ("I", shaded blue) [40, 41, 42], *Super-Kamiokande* neutrinos ("S", shaded orange) [42], as well as *INTEGRAL* Galactic Center MeV flux ("MeV", shaded magenta) [43]. The constraint marked "I" and "MeV" are shown till the lowest PBH masses as displayed in Refs. [41] and [43] respectively.

3.7 Summary of Primordial Black Hole Results

We have presented a new constraint on the abundance of PBH over a broad mass range of $\mathcal{O}(1)M_\odot - 10^7 M_\odot$. This parameter space covers the detected stellar and the very recently observed intermediate-mass BHs, as well as seeds for supermassive black holes. PBH interactions with ISM result in the heating of gas, which we applied to dwarf galaxy Leo T to set the limit. We considered several generic heating mechanisms, including the photon emission from accretion, dynamical friction, and mass outflows/winds. This type of a constraint has not been previously considered for PBH. Our limit does not depend on the cosmological history, which makes it an attractive independent test of PBH in the IMBH mass-range, and this analysis can be readily applied to other systems.

Light PBH, with masses $\lesssim 10^{17}$ g, contributing to DM will significantly emit particles via Hawking radiation depositing energy and heat in the surrounding gas. We have studied gas heating due to spinning and non-spinning PBH, focusing on the dwarf galaxy Leo T. A detailed, conservative, and proper treatment of heating results in presented limits being significantly weaker than previously claimed. We find that limits from spinning evaporating PBH are stronger than for the non-spinning case.

CHAPTER 4

Appendix

4.1 Additional formulas for non-resonant production

Below we show the equations in their general form as function of the η and β parameters appearing in the parametrization of H given in Eq. (2.2) and for the K, ST2 and LRT cosmologies, which were not given in the main text.

We give the equations for the following quantities: the temperature of maximum rate of production $T_{\rm max}$ (except for the LRT model in which the maximum rate of production is at $T_{\rm RH}$), the sterile neutrino momentum distributions $f_{\nu_s}(\epsilon)$ as function of the diensional momentum $\epsilon = p/T$, the relic number density n_{ν_s} and the relic energy density ρ_{ν_s} in general and at present, the present fraction $f_{s,\rm DM}$ of the DM consisting of sterile neutrinos, and the mixing and function of mass $\sin^2(2\theta)_{\rm DW,lim}$ for which this fraction is 1.

In the main text we included only the Std and the ST1 to easily compare the standard cosmology with the alternative cosmology that provides the largest departure from the standard results.

4.1.1 Temperature of maximum rate of production of sterile neutrinos

For the parametrization of H in Eq. (2.2) the temperature of maximum DW production for $\beta \leq 2$ is

$$T_{\rm max} \simeq 190 \text{ MeV } \epsilon^{-\frac{1}{3}} \left(\frac{2-\beta}{10+\beta}\right)^{\frac{1}{6}} \left(\frac{m_s}{\rm keV}\right)^{\frac{1}{3}} \left(\frac{B}{10.88 \times 10^{-9} \text{ GeV}^{-4}}\right)^{-\frac{1}{6}} . \tag{4.1}$$

In K pre-BBN cosmology ($\beta = 1$) it is

$$T^{\rm K}_{\rm max} = 127 \text{ MeV } \epsilon^{-\frac{1}{3}} \left(\frac{m_s}{\rm keV}\right)^{\frac{1}{3}} \left(\frac{B}{10.88 \times 10^{-9} \text{ GeV}^{-4}}\right)^{-\frac{1}{6}} , \tag{4.2}$$

and the ST2 cosmology ($\beta = 0$),

$$T^{\rm ST2}_{\rm max} = T^{\rm Std}_{\rm max} = 145 \text{ MeV } \epsilon^{-\frac{1}{3}} \left(\frac{m_s}{\rm keV}\right)^{\frac{1}{3}} \left(\frac{B}{10.88 \times 10^{-9} \text{ GeV}^{-4}}\right)^{-\frac{1}{6}} . \tag{4.3}$$

The $T_{\rm max}$ for ST2 and the standard cosmology coincide, because $\beta = 0$ for both.

4.1.2 Momentum distribution functions of non-resonantly produced sterile neutrinos

For the parametrization of H in Eq. (2.2) the momentum distribution function, as function of $\epsilon = p/T$, is given by

$$\begin{aligned} f_{\nu_s}(\epsilon) \ &= 3.46 \times 10^{-6}\, \eta^{-1} \epsilon^{\frac{\beta}{3}} (3+\beta)(2.63 \times 10^{-2})^{\beta} \sec\left(\frac{\beta\pi}{6}\right) \left(\frac{\sin^2(2\theta)}{10^{-10}}\right) \\ &\times \left(\frac{m_s}{\rm keV}\right)^{1-\frac{\beta}{3}} \left(\frac{T_{\rm tr}}{5 \text{ MeV}}\right)^{\beta} \left(\frac{g_*}{30}\right)^{-\frac{1}{2}} \left(\frac{d_\alpha}{1.27}\right) \\ &\times \left(\frac{B}{10.88 \times 10^{-9} \text{ GeV}^{-4}}\right)^{-\frac{1}{2}+\frac{\beta}{6}} f_{\nu_\alpha}(\epsilon) . \end{aligned} \tag{4.4}$$

In the K cosmology $\eta = 1$, $\beta = 1$, thus

$$\begin{aligned} f^{\rm K}_{\nu_s}(\epsilon) \ &= 4.2 \times 10^{-7} \epsilon^{\frac{1}{3}} \left(\frac{\sin^2(2\theta)}{10^{-10}}\right) \left(\frac{m_s}{\rm keV}\right)^{\frac{2}{3}} \left(\frac{T_{\rm tr}}{5 \text{ MeV}}\right) \left(\frac{g_*}{30}\right)^{-\frac{1}{2}} \\ &\times \left(\frac{d_\alpha}{1.27}\right) \left(\frac{B}{10.88 \times 10^{-9} \text{ GeV}^{-4}}\right)^{-\frac{1}{3}} f_{\nu_\alpha}(\epsilon) \end{aligned} \tag{4.5}$$

and in the ST2 cosmology, $\eta = 0.03$ and $\beta = 0$, instead

$$\begin{aligned} f^{\rm ST2}_{\nu_s}(\epsilon) \ &= 3.25 \times 10^{-4} \left(\frac{\sin^2(2\theta)}{10^{-10}}\right) \left(\frac{m_s}{\rm keV}\right) \left(\frac{g_*}{30}\right)^{-\frac{1}{2}} \\ &\times \left(\frac{d_\alpha}{1.27}\right) \left(\frac{B}{10.88 \times 10^{-9} \text{ GeV}^{-4}}\right)^{-\frac{1}{2}} f_{\nu_\alpha}(\epsilon) . \end{aligned} \tag{4.6}$$

The distribution function of sterile neutrinos for low reheating temperature (LRT) cosmologies is given in Eq. (1) of Ref. [2], for $T_{\rm RH} = T_{\rm tr}$. In these models sterile neutrinos are dominantly produced during the radiation-dominated period, i.e. for $T < T_{\rm RH}$. We reproduce it here for completeness,

$$f_{\nu_s}^{\rm LRT} = 3.6 \times 10^{-10}\, \epsilon \left(\frac{\sin^2(2\theta)}{10^{-10}}\right) \left(\frac{T_{\rm tr}}{5\ {\rm MeV}}\right)^3 \left(\frac{d_\alpha}{1.13}\right) f_{\nu_\alpha}(\epsilon)\ . \tag{4.7}$$

For consistency of notation, here use $T_{\rm tr}$ for the reheating temperature.

4.1.3 Relic number density of non-resonantly produced sterile neutrinos

The ratio of the number density of non-resonantly produced sterile neutrinos and of active neutrinos at the same temperature T is easily related to the ratio of their momentum distributions,

$$\frac{n_{\nu_s}(T)}{n_{\nu_a}(T)} = \epsilon^{-\frac{\beta}{3}} \frac{F_{2+\frac{\beta}{3}}(0)}{F_2(0)} \frac{f_{\nu_s}(\epsilon)}{f_{\nu_\alpha}(\epsilon)}. \tag{4.8}$$

where we have used the η and β parametrization of H and the number density of active neutrinos (and antineutrinos) here is $n_{\nu_\alpha} = (3\zeta(3)/2\pi^2)\, T^3$. For each cosmology, this ratio is

$$\frac{n_{\nu_s}(T)}{n_{\nu_\alpha}(T)} = \frac{f_{\nu_s}(\epsilon)}{f_{\nu_\alpha}(\epsilon)} \times \begin{cases} 1 & , \quad \text{Std, ST2} \\ 1.42\ \epsilon^{-0.33}, & \quad \text{K} \\ 0.77\ \epsilon^{\ 0.27} & , \quad \text{ST1} \\ 3.15\ \epsilon^{-1} & , \quad \text{LRH} \end{cases} \tag{4.9}$$

The present number density of non-resonantly produced sterile neutrinos as a function of the η and β parameters of H in Eq. (2.2) is

$$\begin{aligned} n_{\nu_s} = {} & 8.78 \times 10^{-3} {\rm cm}^{-3} \eta^{-1} \left(2.63 \times 10^{-2}\right)^\beta \left(1 - 2^{-2-\frac{\beta}{3}}\right) \zeta\left(3 + \frac{\beta}{3}\right) \Gamma\left(3 + \frac{\beta}{3}\right) \\ & \times \left(\frac{3+\beta}{36\pi}\right) \sec\left(\frac{\beta\pi}{6}\right) \left(\frac{\sin^2(2\theta)}{10^{-10}}\right) \left(\frac{m_s}{\rm keV}\right)^{1-\frac{\beta}{3}} \left(\frac{T_{\rm tr}}{5\ {\rm MeV}}\right)^\beta \left(\frac{T_{\nu,0}}{1.95\ {\rm K}}\right)^3 \\ & \times \left(\frac{g_*}{30}\right)^{-\frac{3}{2}} \left(\frac{d_\alpha}{1.27}\right) \left(\frac{B}{10.88 \times 10^{-9}\ {\rm GeV}^{-4}}\right)^{-\frac{1}{2}+\frac{\beta}{6}} . \end{aligned} \tag{4.10}$$

Here g_* is the number of relativistic degrees of freedom when sterile neutrinos are produced, which we take to be $g_*(T_{\rm max})$ thus at present the ratio of temperatures of the sterile and active neutrinos is $(T_{\nu_s,0}/T_{\nu,0}) = (g_*/10.75)^{1/3}$. $T_{\nu,0} = 1.95$ K is the present temperature of the relic active neutrino bath.

For K ($\eta = 1$, $\beta = 1$) the sterile neutrino number density is

$$n_{\nu_s}^{\rm K}(T_{\nu_s}) \ = 5.95 \times 10^{-7} \left(\frac{\sin^2(2\theta)}{10^{-10}}\right) \left(\frac{m_s}{\rm keV}\right)^{\frac{2}{3}} \left(\frac{T_{\rm tr}}{5 \ {\rm MeV}}\right) \left(\frac{T_{\nu_s}}{T_{\nu_\alpha}}\right)^3 \left(\frac{g_*}{30}\right)^{-\frac{1}{2}} \times \left(\frac{d_\alpha}{1.27}\right) \left(\frac{B}{10.88 \times 10^{-9} \ {\rm GeV}^{-4}}\right)^{-\frac{1}{3}} n_{\nu_\alpha}(T_{\nu_\alpha}) \ , \tag{4.11}$$

and the present number density is

$$n_{\nu_s}^{\rm K} = 2.41 \times 10^{-5} {\rm cm}^{-3} \left(\frac{\sin^2(2\theta)}{10^{-10}}\right) \left(\frac{m_s}{\rm keV}\right)^{\frac{2}{3}} \left(\frac{T_{\rm tr}}{5 \ {\rm MeV}}\right) \left(\frac{T_{\nu,0}}{1.95 \ {\rm K}}\right)^3 \times \left(\frac{g_*}{30}\right)^{-\frac{3}{2}} \left(\frac{d_\alpha}{1.27}\right) \left(\frac{B}{10.88 \times 10^{-9} \ {\rm GeV}^{-4}}\right)^{-\frac{1}{3}} \ . \tag{4.12}$$

For ST2 ($\eta = 0.03$, $\beta = 0$) the number density it

$$n_{\nu_s}^{\rm ST2}(T_{\nu_s}) \ = 3.25 \times 10^{-4} \left(\frac{\sin^2(2\theta)}{10^{-10}}\right) \left(\frac{m_s}{\rm keV}\right) \left(\frac{T_{\nu_s}}{T_{\nu_\alpha}}\right)^3 \left(\frac{g_*}{30}\right)^{-\frac{1}{2}} \times \left(\frac{d_\alpha}{1.27}\right) \left(\frac{B}{10.88 \times 10^{-9} \ {\rm GeV}^{-4}}\right)^{-\frac{1}{2}} n_{\nu_\alpha}(T_{\nu_\alpha}) \ , \tag{4.13}$$

and the present number density is

$$n_{\nu_s}^{\rm ST2} = 1.31 \times 10^{-2} {\rm cm}^{-3} \left(\frac{\sin^2(2\theta)}{10^{-10}}\right) \left(\frac{m_s}{\rm keV}\right) \left(\frac{T_{\nu,0}}{1.95 \ {\rm K}}\right)^3 \times \left(\frac{g_*}{30}\right)^{-\frac{3}{2}} \left(\frac{d_\alpha}{1.27}\right) \left(\frac{B}{10.88 \times 10^{-9} \ {\rm GeV}^{-4}}\right)^{-\frac{1}{2}} \ . \tag{4.14}$$

In the LRT cosmology (see Eq. 2 of Ref. [2]) the number density is

$$n_{\nu_s}^{\rm LRT}(T_{\nu_s}) \ = \ 1.13 \times 10^{-9} \left(\frac{\sin^2(2\theta)}{10^{-10}}\right) \left(\frac{T_{\rm tr}}{5 \ {\rm MeV}}\right)^3 \left(\frac{d_\alpha}{1.13}\right) n_{\nu_\alpha}(T_{\nu_\alpha}) \ , \tag{4.15}$$

and the present number density is

$$n_{\nu_s}^{\rm LRT} \ = \ 1.28 \times 10^{-7} {\rm cm}^{-3} \left(\frac{\sin^2(2\theta)}{10^{-10}}\right) \left(\frac{T_{\rm tr}}{5 \ {\rm MeV}}\right)^3 \left(\frac{T_{\nu,0}}{1.95 \ {\rm K}}\right)^3 \left(\frac{d_\alpha}{1.13}\right) \ . \tag{4.16}$$

4.1.4 Energy density of non-resonantly produced relativistic sterile neutrinos

The ratio of the energy density of non-resonantly produced relativistic sterile neutrinos and of relativistic active neutrinos at the same temperature T is easily related to their number density ratio, and momentum distribution ratios,

$$\frac{\rho_{\nu_s}(T)}{\rho_{\nu_a}(T)} = \frac{F_{3+\frac{\beta}{3}}(0)}{F_3(0)} \frac{F_2(0)}{F_{2+\frac{\beta}{3}}(0)} \frac{n_{\nu_s}(T)}{n_{\nu_\alpha}(T)} = \epsilon^{-\frac{\beta}{3}} \frac{F_{3+\frac{\beta}{3}}(0)}{F_3(0)} \frac{f_{\nu_s}(\epsilon)}{f_{\nu_\alpha}(\epsilon)}. \tag{4.17}$$

where the energy density of relativistic active neutrinos (and antineutrinos) is here $\rho_{\nu_\alpha} = (7\pi^2/120)\, T^4$. Hence,

$$\frac{\rho_{\nu_s}(T)}{\rho_{\nu_\alpha}(T)} = \frac{n_{\nu_s}(T)}{n_{\nu_\alpha}(T)} \times \begin{cases} 1, & \text{Std, ST2} \\ 1.10, & \text{K} \\ 0.92, & \text{ST1} \\ 1.30, & \text{LRH} \end{cases} \tag{4.18}$$

The energy density of relativistic sterile neutrinos at temperature T_{ν_s} produced non resonantly when the number of degrees of freedom were g^* (we take this to be the g_* at T_{max}), using the η and β parameterization of H, is

$$\begin{aligned}\rho_{\nu_s}(T_{\nu_s}) &= 4.95 \times 10^{26}\ \text{MeV/cm}^3\ \eta^{-1} \left(2.63 \times 10^{-2}\right)^{\beta} \left(1 - 2^{-3-\frac{\beta}{3}}\right) \zeta\left(4 + \frac{\beta}{3}\right) \Gamma\left(4 + \frac{\beta}{3}\right) \\ &\times \left(\frac{3+\beta}{36\pi}\right) \sec\left(\frac{\beta\pi}{6}\right) \left(\frac{\sin^2(2\theta)}{10^{-10}}\right) \left(\frac{m_s}{\text{keV}}\right)^{1-\frac{\beta}{3}} \left(\frac{T_{\text{tr}}}{5\ \text{MeV}}\right)^{\beta} \left(\frac{T_{\nu_s}}{\text{MeV}}\right)^4 \\ &\times \left(\frac{g_*}{30}\right)^{-\frac{11}{6}} \left(\frac{d_\alpha}{1.27}\right) \left(\frac{B}{10.88 \times 10^{-9}\ \text{GeV}^{-4}}\right)^{-\frac{1}{2}+\frac{\beta}{6}} ,\end{aligned} \tag{4.19}$$

which for K becomes

$$\begin{aligned}\rho^{\text{K}}_{\nu_s}(T_{\nu_s}) &= 6.55 \times 10^{-7} \left(\frac{\sin^2(2\theta)}{10^{-10}}\right) \left(\frac{m_s}{\text{keV}}\right)^{\frac{2}{3}} \left(\frac{T_{\text{tr}}}{5\ \text{MeV}}\right) \left(\frac{T_{\nu_s}}{T_{\nu_\alpha}}\right)^4 \left(\frac{g_*}{30}\right)^{-\frac{1}{2}} \\ &\times \left(\frac{d_\alpha}{1.27}\right) \left(\frac{B}{10.88 \times 10^{-9}\ \text{GeV}^{-4}}\right)^{-\frac{1}{3}} \rho_{\nu_\alpha}(T_{\nu_\alpha}) ,\end{aligned} \tag{4.20}$$

or,

$$\begin{aligned}\rho^{\text{K}}_{\nu_s}(T_{\nu_s}) &= 4.91 \times 10^{25}\ \text{MeV/cm}^3 \left(\frac{\sin^2(2\theta)}{10^{-10}}\right) \left(\frac{m_s}{\text{keV}}\right)^{\frac{2}{3}} \left(\frac{T_{\text{tr}}}{5\ \text{MeV}}\right) \left(\frac{T_{\nu_s}}{1\ \text{MeV}}\right)^4 \\ &\times \left(\frac{g_*}{30}\right)^{-\frac{1}{2}} \left(\frac{d_\alpha}{1.27}\right) \left(\frac{B}{10.88 \times 10^{-9}\ \text{GeV}^{-4}}\right)^{-\frac{1}{3}} ,\end{aligned} \tag{4.21}$$

and for ST2 is

$$\begin{aligned}\rho^{\text{ST2}}_{\nu_s}(T_{\nu_s}) &= 3.25 \times 10^{-4} \left(\frac{\sin^2(2\theta)}{10^{-10}}\right) \left(\frac{m_s}{\text{keV}}\right) \left(\frac{T_{\nu_s}}{T_{\nu_\alpha}}\right)^4 \left(\frac{g_*}{30}\right)^{-(1/2)} \\ &\times \left(\frac{d_\alpha}{1.27}\right) \left(\frac{B}{10.88 \times 10^{-9}\ \text{GeV}^{-4}}\right)^{-\frac{1}{2}} \rho_{\nu_\alpha}(T_{\nu_\alpha}) ,\end{aligned} \tag{4.22}$$

or,

$$\rho_{\nu_s}^{\rm ST2}(T_{\nu_s}) = 2.44\times 10^{28}\ {\rm MeV/cm^3}\left(\frac{\sin^2(2\theta)}{10^{-10}}\right)\left(\frac{m_s}{\rm keV}\right)\left(\frac{T_{\nu_s}}{1\ {\rm MeV}}\right)^4 \times\left(\frac{g_*}{30}\right)^{-(1/2)}\left(\frac{d_\alpha}{1.27}\right)\left(\frac{B}{10.88\times10^{-9}\ {\rm GeV^{-4}}}\right)^{-\frac{1}{2}} . \quad (4.23)$$

In the LRT model, production happens only during the standard phase (i.e. when $\eta = 1$ and $\beta = 0$), at temperatures smaller than the reheating temperature $T_{\rm RH}$, which we denote here $T_{\rm tr}$, and is dominated by the production close to $T_{\rm tr}$. For temperatures $m_s < T < T_{\rm tr}$ the relic energy density in the LRT model is

$$\begin{aligned}\rho_{\nu_s}^{\rm LRT}(T_{\nu_s}) &= 1.48\times10^{-9}\left(\frac{\sin^2(2\theta)}{10^{-10}}\right)\left(\frac{T_{\rm tr}}{5\ {\rm MeV}}\right)^3\left(\frac{T_{\nu_s}}{T_{\nu_\alpha}}\right)^4\left(\frac{d_\alpha}{1.13}\right)\rho_{\nu_\alpha}(T_{\nu_\alpha})\\ &= 1.11\times10^{23}\ {\rm MeV/cm^3}\left(\frac{\sin^2(2\theta)}{10^{-10}}\right)\left(\frac{T_{\rm tr}}{5\ {\rm MeV}}\right)^3\left(\frac{T_{\nu_s}}{1\ {\rm MeV}}\right)^4\left(\frac{d_\alpha}{1.13}\right) . \quad (4.24)\end{aligned}$$

4.1.5 Present fraction of the DM in non-resonantly produced sterile neutrinos

The present fraction of DM comprised of non-relativistic sterile neutrinos at present as function of the η and β parameters in Eq. (2.2) is

$$\begin{aligned} f_{s,\rm DM} &= \left(\frac{n_{\nu_s,0}\, m_s}{\rho_{\rm DM}}\right) = \\ &= 5.16\times10^{-5}\eta^{-1}\left(2.63\times10^{-2}\right)^\beta(3+\beta)\left(1-2^{-2-\frac{\beta}{3}}\right)\zeta\left(3+\frac{\beta}{3}\right)\\ &\times\Gamma\left(3+\frac{\beta}{3}\right)\sec\left(\frac{\beta\pi}{6}\right)\left(\frac{\sin^2(2\theta)}{10^{-10}}\right)\left(\frac{m_s}{\rm keV}\right)^{2-\frac{\beta}{3}}\left(\frac{T_{\rm tr}}{5\ {\rm MeV}}\right)^\beta\\ &\times\left(\frac{T_{\nu,0}}{1.95\ {\rm K}}\right)^3\left(\frac{g_*}{30}\right)^{-\frac{3}{2}}\left(\frac{d_\alpha}{1.27}\right)\left(\frac{\Omega_{\rm DM}h^2}{0.12}\right)\left(\frac{B}{10.88\times10^{-9}\ {\rm GeV^{-4}}}\right)^{-\frac{1}{2}+\frac{\beta}{6}} , \quad (4.25)\end{aligned}$$

where $n_{\nu_s,0}$ is the present number density, g_* is the number of entropy degrees of freedom when the sterile neutrinos were produced, $g_* = g_*(T_{max})$, and $T_{\nu,0}$ is the present active neutrino temperature. Unless stated otherwise we take $g_* = 30$ for our figures. For the K cosmology ($\eta = 1$, $\beta = 1$) the fraction is

$$
\begin{aligned}
f^{\mathrm{K}}_{s,\mathrm{DM}} = \left(\frac{n_{\nu_s,0}\, m_s}{\rho_{\mathrm{DM}}}\right)^{\mathrm{K}} &= \\
&= 1.60 \times 10^{-5} \left(\frac{\sin^2(2\theta)}{10^{-10}}\right) \left(\frac{m_s}{\mathrm{keV}}\right)^{\frac{5}{3}} \left(\frac{T_{\mathrm{tr}}}{5\ \mathrm{MeV}}\right) \left(\frac{T_{\nu,0}}{1.95\ \mathrm{K}}\right)^{3} \\
&\times \left(\frac{g_*}{30}\right)^{-\frac{3}{2}} \left(\frac{d_\alpha}{1.27}\right) \left(\frac{\Omega_{\mathrm{DM}} h^2}{0.12}\right) \left(\frac{B}{10.88 \times 10^{-9}\ \mathrm{GeV}^{-4}}\right)^{-\frac{1}{3}}
\end{aligned}
\tag{4.26}
$$

and for ST2 cosmology ($\eta = 0.03$, $\beta = 0$),

$$
\begin{aligned}
f^{\mathrm{ST2}}_{s,\mathrm{DM}} = \left(\frac{n_{\nu_s,0}\, m_s}{\rho_{\mathrm{DM}}}\right)^{\mathrm{ST2}} &= \\
&= 8.70 \times 10^{-3} \left(\frac{\sin^2(2\theta)}{10^{-10}}\right) \left(\frac{m_s}{\mathrm{keV}}\right)^{2} \left(\frac{T_{\nu,0}}{1.95\ \mathrm{K}}\right)^{3} \left(\frac{g_*}{30}\right)^{-\frac{3}{2}} \\
&\times \left(\frac{d_\alpha}{1.27}\right) \left(\frac{\Omega_{\mathrm{DM}} h^2}{0.12}\right) \left(\frac{B}{10.88 \times 10^{-9}\ \mathrm{GeV}^{-4}}\right)^{-\frac{1}{2}} .
\end{aligned}
\tag{4.27}
$$

In the LRT model with T_{tr} denoting the reheating temperature, the fraction is instead

$$
\begin{aligned}
f^{\mathrm{LRT}}_{s,\mathrm{DM}} = \left(\frac{n_{\nu_s,0}\, m_s}{\rho_{\mathrm{DM}}}\right)^{\mathrm{LRT}} &= \\
&= 1 \times 10^{-7} \left(\frac{\sin^2(2\theta)}{10^{-10}}\right) \left(\frac{m_s}{\mathrm{keV}}\right) \left(\frac{T_{\mathrm{tr}}}{5\mathrm{MeV}}\right)^{3} \left(\frac{T_{\nu,0}}{1.95\ \mathrm{K}}\right)^{3} \\
&\times \left(\frac{d_\alpha}{1.13}\right) \left(\frac{\Omega_{\mathrm{DM}} h^2}{0.12}\right) .
\end{aligned}
\tag{4.28}
$$

4.1.6 DM density limit

The limit on the sterile-active neutrino mixing angle from DM density, $f_{s,\mathrm{DM}} \leq 1$ translates into $\sin^2(2\theta) < \sin^2(2\theta)_{\mathrm{DW,lim}}$, as function of η and β in Eq. (2.2), where

$$
\begin{aligned}
\sin^2(2\theta)_{\mathrm{DW,lim}} &= 1.94 \times 10^{-6} \eta \left[\left(1 - 2^{-2-\frac{\beta}{3}}\right) \zeta\left(3 + \frac{\beta}{3}\right) \sec\left(\frac{\beta\pi}{6}\right) \Gamma\left(3 + \frac{\beta}{3}\right) (3+\beta)\right]^{-1} \\
&\times \left(2.63 \times 10^{-2}\right)^{-\beta} \left(\frac{m_s}{\mathrm{keV}}\right)^{-2+\frac{\beta}{3}} \left(\frac{T_{\mathrm{tr}}}{5\ \mathrm{MeV}}\right)^{-\beta} \left(\frac{T_{\nu,0}}{1.95\ \mathrm{K}}\right)^{-3} \left(\frac{g_*}{30}\right)^{\frac{3}{2}} \\
&\times \left(\frac{d_\alpha}{1.27}\right)^{-1} \left(\frac{\Omega_{\mathrm{DM}} h^2}{0.12}\right)^{-1} \left(\frac{B}{10.88 \times 10^{-9}\ \mathrm{GeV}^{-4}}\right)^{\frac{1}{2}-\frac{\beta}{6}} .
\end{aligned}
\tag{4.29}
$$

For the K model ($\eta = 1$, $\beta = 1$)

$$\begin{aligned}\sin^2(2\theta)^{\rm K}_{\rm DW,lim} &= 6.26\times10^{-6}\left(\frac{m_s}{\rm keV}\right)^{-\frac{5}{3}}\left(\frac{T_{\rm tr}}{5~\rm MeV}\right)^{-1}\left(\frac{T_{\nu,0}}{1.95~\rm K}\right)^{-3}\left(\frac{g_*}{30}\right)^{\frac{3}{2}}\\ &\times\left(\frac{d_\alpha}{1.27}\right)^{-1}\left(\frac{\Omega_{\rm DM}h^2}{0.12}\right)^{-1}\left(\frac{B}{10.88\times10^{-9}~\rm GeV^{-4}}\right)^{\frac{1}{3}}~.\end{aligned} \tag{4.30}$$

For ST2 ($\eta = 0.03$, $\beta = 0$) instead,

$$\begin{aligned}\sin^2(2\theta)^{\rm ST2}_{\rm DW,lim} &= 1.15\times10^{-8}\left(\frac{m_s}{\rm keV}\right)^{-2}\left(\frac{T_{\nu,0}}{1.95~\rm K}\right)^{-3}\left(\frac{g_*}{30}\right)^{\frac{3}{2}}\left(\frac{d_\alpha}{1.27}\right)^{-1}\\ &\times\left(\frac{\Omega_{\rm DM}h^2}{0.12}\right)^{-1}\left(\frac{B}{10.88\times10^{-9}~\rm GeV^{-4}}\right)^{\frac{1}{2}}~.\end{aligned} \tag{4.31}$$

For the LRT model, with $T_{\rm tr} = T_{\rm RH}$,

$$\sin^2(2\theta)^{\rm LRT}_{\rm DW,lim} = 1\times10^{-3}\left(\frac{m_s}{\rm keV}\right)^{-1}\left(\frac{T_{\rm tr}}{5~\rm MeV}\right)^{-3}\left(\frac{T_{\nu,0}}{1.95~\rm K}\right)^{-3}\left(\frac{d_\alpha}{1.13}\right)^{-1}\left(\frac{\Omega_{\rm DM}h^2}{0.12}\right)^{-1}~. \tag{4.32}$$

4.2 Additional Formulas for Resonant Production

4.2.1 Temperature of maximum non-resonant production

We recomputed for the different cosmologies we considered the temperature $T_{\rm max}$ at which the non-resonant production rate integrated over momentum, denoted γ in the DW paper [135], over H

$$\frac{\gamma}{H} = \frac{d}{d\ln T}\left(\frac{n_{\nu_s}}{n_{\nu_\alpha}}\right)~, \tag{4.33}$$

is maximum, as done for the standard cosmology in Ref. [135] (see Eqs. (4) to (6) of Ref. [135] and also [179]). Note that in section 2.3, we refer to $T_{\rm max}$ as the maximum of $(\Gamma f_{\nu_\alpha}/HT)$, not integrated over momenta, which thus depends on ϵ. We recomputed $T_{\rm max}$ for each cosmologies by numerically plotting (γ/H) and changing the x factor in front of the integral in Eq. (6) of Ref. [135] to $x^{1-\beta/3}$. Our value for the standard cosmology differs from that of DW because we use $B = 10.88\times10^{-9}$ GeV^{-4}, which is the right value for the $\nu_e \leftrightarrow \nu_s$ transitions considered in our paper, while DW used $B \approx 3\times10^{-9}$ GeV^{-4}, as is appropriate for ν_μ or ν_τ to ν_s transitions at temperatures at which μ and τ charged leptons are not in equilibrium (see Eq.(2.84)). Our result for the standard cosmology coincides with the $T_{\rm max}$ given in Ref. [179],

$$T^{\rm Std}_{\rm max} = T^{\rm ST2}_{\rm max} \simeq 108 \text{ MeV} \left(\frac{m_s}{\rm keV}\right)^{\frac{1}{3}} \ . \tag{4.34}$$

For the standard and ST2 cosmologies, $\beta = 0$. For ST1 ($\beta = -0.8$),

$$T^{\rm ST1}_{\rm max} \simeq 118 \text{ MeV} \left(\frac{m_s}{\rm keV}\right)^{\frac{1}{3}} \ , \tag{4.35}$$

and for kination ($\beta = 1$)

$$T^{\rm K}_{\rm max} \simeq 94.5 \text{ MeV} \left(\frac{m_s}{\rm keV}\right)^{\frac{1}{3}} \ . \tag{4.36}$$

4.2.2 Combined resonant and non-resonant production

In Section 2.6.3, we derived a lower limit on the sterile neutrino mass for non-resonant production to happen after resonant production. In the K cosmology ($\eta = 1$, $\beta = 1$) this is

$$m_s > m^{\rm K}_{\rm non\text{-}res} = 1.61 \times 10^4 \text{ keV } \epsilon_{\rm res}^{\frac{3}{2}} \mathcal{L}^{\frac{3}{2}} \ , \tag{4.37}$$

and for ST2 ($\eta = 0.03$, $\beta = 0$)

$$m_s > m^{\rm ST2}_{\rm non\text{-}res} = 3.59 \times 10^4 \text{ keV } \epsilon_{\rm res}^{\frac{3}{2}} \mathcal{L}^{\frac{3}{2}} \ . \tag{4.38}$$

4.2.3 Coherence

The coherence condition in Eq. (2.99), $\Gamma_\alpha^{-1} > l_{\rm res}$, given as a function of the η and β parameters in Eq. (2.2) is

$$\sin^2(2\theta) < 2.19 \times 10^{-6} \ (3.76)^{2\beta} \ \eta^2 \epsilon^{-\frac{1}{2}-\frac{\beta}{2}} \left(\frac{m_s}{\rm keV}\right)^{-3+\beta} \mathcal{L}^{\frac{3}{2}-\frac{\beta}{2}} \left(\frac{T_{\rm tr}}{5 \text{ MeV}}\right)^{-2\beta} \left(\frac{g_*}{10.75}\right) \ . \tag{4.39}$$

For the K cosmology ($\eta = 1$, $\beta = 1$), this is

$$\sin^2(2\theta)^{\rm K} < 3.10 \times 10^{-5} \epsilon^{-1} \left(\frac{m_s}{\rm keV}\right)^{-2} \mathcal{L} \left(\frac{T_{\rm tr}}{5 \text{ MeV}}\right)^{-2} \left(\frac{g_*}{10.75}\right) \ , \tag{4.40}$$

while for the ST2 cosmology ($\eta = 0.03$, $\beta = 0$) this is

$$\sin^2(2\theta)^{\rm ST2} < 2.24 \times 10^{-9} \epsilon^{-\frac{1}{2}} \left(\frac{m_s}{\rm keV}\right)^{-3} \mathcal{L}^{\frac{3}{2}} \left(\frac{g_*}{10.75}\right) \ . \tag{4.41}$$

4.2.4 Adiabaticity

The adiabaticity condition $\gamma > \gamma_{\rm lim} \geq 1$ of Eq. (2.103) in terms of the η and β parametrs of H in Eq. (2.2) is

$$\sin^2(2\theta) > 2.34 \times 10^{-11} (3.76)^\beta \ \eta \ \gamma_{\rm lim} \ \epsilon^{\frac{1}{4}-\frac{\beta}{4}} \left(\frac{m_s}{\rm keV}\right)^{\frac{\beta}{2}-\frac{1}{2}} \mathcal{L}^{-\frac{3}{4}-\frac{\beta}{4}} \left(\frac{T_{\rm tr}}{5 \ {\rm MeV}}\right)^{-\beta} \left(\frac{g_*}{10.75}\right)^{\frac{1}{2}} . \tag{4.42}$$

For K cosmology ($\eta = 1$, $\beta = 1$) this becomes

$$\sin^2(2\theta)^{\rm K} > 8.80 \times 10^{-11} \gamma_{\rm lim} \ \mathcal{L}^{-1} \left(\frac{T_{\rm tr}}{5 \ {\rm MeV}}\right)^{-1} \left(\frac{g_*}{10.75}\right)^{\frac{1}{2}} , \tag{4.43}$$

and for ST2 ($\eta = 0.03$, $\beta = 0$) cosmology it is

$$\sin^2(2\theta)^{\rm ST2} > 7.48 \times 10^{-13} \gamma_{\rm lim} \ \epsilon^{\frac{1}{4}} \left(\frac{m_s}{\rm keV}\right)^{-\frac{1}{2}} \mathcal{L}^{-\frac{3}{4}} \left(\frac{g_*}{10.75}\right)^{\frac{1}{2}} . \tag{4.44}$$

4.2.5 Thermalization

The thermalization limit given as a function of the η and β parameters in Eq. (2.2) rejects

$$\sin^2(2\theta) > 119 \frac{(1-x)^2}{x^{\frac{3-\beta}{4}}} (0.09)^\beta \eta \left(\frac{\epsilon}{3.15}\right)^{\frac{3-\beta}{4}} \left(\frac{m_s}{\rm eV}\right)^{-\frac{3-\beta}{2}} \mathcal{L}^{\frac{3-\beta}{4}} \left(\frac{g}{10.75}\right)^{\frac{1}{2}} , \tag{4.45}$$

For the K cosmology ($\eta = 1$,$\beta = 1$), the limit rejects

$$\sin^2(2\theta) > 10.5 \frac{(1-x)^2}{x^{\frac{1}{2}}} \left(\frac{\epsilon}{3.15}\right)^{\frac{1}{2}} \left(\frac{m_s}{\rm eV}\right)^{-1} \mathcal{L}^{\frac{1}{2}} \left(\frac{g}{10.75}\right)^{\frac{1}{2}} , \tag{4.46}$$

while for the ST2 cosmology ($\eta = 0.03$, $\beta = 0$) this is

$$\sin^2(2\theta) > 3.56 \frac{(1-x)^2}{x^{\frac{3}{4}}} \left(\frac{\epsilon}{3.15}\right)^{\frac{3}{4}} \left(\frac{m_s}{\rm eV}\right)^{-\frac{3}{2}} \mathcal{L}^{\frac{3}{4}} \left(\frac{g}{10.75}\right)^{\frac{1}{2}} , \tag{4.47}$$

4.3 Gas systems with bulk relative velocity

A gas system with a bulk relative velocity v_b with respect to the galactic frame can be treated as follows. Without loss of generality, consider the frame in which the bulk velocity is rotated to the z direction. Then, the one dimensional Maxwellian velocity distributions are

$$\begin{cases} f_x(v_x) = f_y(v_y) = \frac{1}{\sqrt{2\pi}\sigma_v} e^{-\frac{v_x^2}{2\sigma_v^2}} \\ \\ f_z(v_z) = \frac{1}{\sqrt{2\pi}\sigma_v} e^{-\frac{(v_z - v_b)^2}{2\sigma_v^2}} \end{cases} \tag{4.48}$$

Imposing the constraint $v^2 = \sqrt{v_x^2 + v_y^2 + v_z^2}$, the relative velocity distribution is given by the integral

$$\begin{aligned} f(v) &= \frac{1}{(2\pi)^{\frac{3}{2}}\sigma_v^3} \int_{-\infty}^{\infty} dv_x \int_{-\infty}^{\infty} dv_y \int_{-\infty}^{\infty} dv_z \delta(v^2 - v_x^2 - v_y^2 - v_z^2) e^{-\frac{v_x^2 + v_y^2 + (v_z - v_b)^2}{2\sigma_v^2}} \\ &= \frac{e^{-\frac{v^2 + v_b^2}{2\sigma^2}}}{(2\pi)^{\frac{3}{2}}\sigma_v^3} \int_{-v}^{v} dv_x \int_{-\sqrt{v^2 - v_x^2}}^{\sqrt{v^2 - v_x^2}} dv_y \frac{v}{\sqrt{v^2 - v_x^2 - v_y^2}} \left[e^{-\frac{v_b\sqrt{v^2 - v_x^2 - v_y^2}}{\sigma_v^2}} + e^{-\frac{v_b\sqrt{v^2 - v_x^2 - v_y^2}}{\sigma_v^2}} \right] . \end{aligned} \tag{4.49}$$

Switching to polar velocity coordinates and simplifying,

$$\begin{aligned} f(v) &= \frac{2\pi v}{(2\pi)^{\frac{3}{2}}\sigma_v^3} e^{-\frac{v^2 + v_b^2}{2\sigma_v^2}} \int_0^v dv_r \frac{v_r}{\sqrt{v^2 - v_r^2}} \left[e^{-\frac{v_b\sqrt{v^2 - v_r^2}}{\sigma_v^2}} + e^{\frac{v_b\sqrt{v^2 - v_r^2}}{\sigma_v^2}} \right] \\ &= \frac{v}{\sqrt{2\pi}\sigma v_b} \left[e^{-\frac{(v - v_b)^2}{2\sigma^2}} - e^{-\frac{(v + v_b)^2}{2\sigma^2}} \right] . \end{aligned} \tag{4.50}$$

In the limit $v_b \to 0$, Eq. (4.50) reproduces the standard Maxwellian distribution Eq. (3.7).

4.4 ADAF temperature considerations

For ADAF, the electron temperature θ_e is determined by balancing the heating and radiation processes [279]. At low $\dot{m}$, direct viscous electron heating δq_+ is dominant, and is superseded by ion-electron collisional heating q_{ie} at high accretion rates. This results in different temperature considerations for each of the ADAF sub-regimes.

The heating contributions are given by

$$\begin{aligned} \delta q_+ &= 9.39 \times 10^{38} \ \frac{\text{erg}}{\text{s}} \ \delta \left(\frac{1 - \beta}{f} \right) c_3 m \dot{m} r_{\text{min}}^{-1} \\ q_{ie} &= 1.2 \times 10^{38} \ \frac{\text{erg}}{\text{s}} \ g(\theta_e) \alpha^{-2} c_1^{-2} c_3 \beta m \dot{m}^2 r_{\text{min}}^{-1} \ , \end{aligned} \tag{4.51}$$

where f is the fraction of energy advected, which is ~ 1 for ADAF flows, and $g(\theta_e)$ is an $\mathcal{O}(1)$ function

$$g(\theta_e) = \frac{1}{K_2(1/\theta_e)}\left(2 + 2\theta_e + \frac{1}{\theta_e}\right) e^{-\frac{1}{\theta_e}} \tag{4.52}$$

that takes on the values of $4.5 - 0.63$ in the temperature range $2 \times 10^9 \leq T_e \leq 10^{10}$. For computational simplicity, we use the approximation $g(\theta_e) \simeq 1.19\ \theta_e^{-1.15}$, which has a maximum error of $\sim 20\%$ [279] over our temperature range of interest. When the two electron heating processes are equal, $\delta q_+ = q_{ie}$, the accretion rate is

$$\dot{m}_{\rm eq} = 2.0 \times 10^{-3}\left(\frac{\alpha}{0.1}\right)^2 \left(\frac{\delta}{0.1}\right)\left(\frac{1-\beta}{\beta}\right)\left(\frac{c_1}{0.5}\right)^2 \left(\frac{f}{1.0}\right)^{-1} g(\theta_e)^{-1}\ . \tag{4.53}$$

This is similar to our condition $\dot{M}_{\rm ADAF} = 10^{-3}(\alpha/0.1)^2$ of Sec. 3.3.1.2. Thus, in the "eADAF" and "ADAF" regimes, we use δq_+ heating and q_{ie} heating for "LHAF".

For $\dot{m} < \dot{M}_{\rm ADAF}$, direct viscous heating balances the synchrotron and IC emission, which are of comparable magnitude. The temperature can be estimated as [279]

$$\theta_e \simeq 0.2 A_c^{-\frac{1}{7}} \delta^{\frac{1}{7}} \alpha^{\frac{3}{14}} (1-\beta)^{-\frac{1}{14}} r_{\rm min}^{\frac{3}{28}} \left(\frac{M}{M_\odot}\right)^{\frac{1}{14}} \dot{m}^{-\frac{5}{28}}\ . \tag{4.54}$$

Here $A_c^{1/7}$ is determined by the relative contributions of synchrotron and IC cooling, ranging from 0.95 to 1.4. As $\dot{m}$ increases, the accretion flow radiates more efficiently through IC scattering, cooling the electron plasma. We approximate $A_c^{\frac{1}{7}} = 1.1$ for $\dot{m} < \dot{M}_{\rm eADAF}$, and $A_c^{\frac{1}{7}} = 1.3$ for $\dot{M}_{\rm eADAF} < \dot{m} < \dot{M}_{\rm ADAF}$.

In the LHAF regime, the dominant IC emission is highly sensitive to temperature variations and balanced against ion electron q_{ie} heating. We use an iterative scheme modified from that of Ref. [279] to self-consistently determine the resulting temperature[1]. Starting with an initial guess of $\alpha_c = 0.75$, Eq. (3.20) can be solved for the temperature,

$$\theta_e = \frac{\sqrt{4\tau_{es}^{-1/\alpha_c} - 3} - 1}{8}\ . \tag{4.55}$$

[1]Eq. (45) in Ref. [279] is used in lieu of Eq. (46) (which contains a sign error), the approximations for x_M and $g(\theta_e)$ are used in Eq. (47), and the new and old values of the temperature are averaged to improve convergence.

This result is then used to solve iteratively for a new α_c as

$$\alpha_{c,\mathrm{new}} = 1 - \frac{\ln\left[(1-\alpha_{c,\mathrm{old}})\dfrac{q_{ie}}{\nu_p L_{\nu_p}} + 1\right]}{\ln C_f} \ , \tag{4.56}$$

where

$$\begin{aligned}
\frac{q_{ie}}{\nu_p L_{\nu_p}} &= 1.78 \times 10^{-5} \theta_e^{-8.15} \alpha^{-\frac{1}{2}} \beta (1-\beta)^{-\frac{3}{2}} r_{\mathrm{min}}^{\frac{3}{4}} \left(\frac{M}{M_\odot}\right)^{\frac{1}{2}} \dot{m}^{-\frac{1}{4}} \ , \\
C_f &= 20.2 \alpha^{\frac{1}{2}} (1-\beta)^{-\frac{1}{2}} r_{\mathrm{min}}^{\frac{5}{4}} \theta_e^{-1} \left(\frac{M}{M_\odot}\right)^{\frac{1}{2}} \dot{m}^{-\frac{3}{4}} \ .
\end{aligned} \tag{4.57}$$

After each iteration, the new and old values of the temperature is averaged to speed up convergence.

REFERENCES

[1] Bernard Carr, Kazunori Kohri, Yuuiti Sendouda, and Jun'ichi Yokoyama. Constraints on Primordial Black Holes. 2 2020.

[2] Graciela Gelmini, Sergio Palomares-Ruiz, and Silvia Pascoli. Low reheating temperature and the visible sterile neutrino. *Phys. Rev. Lett.*, 93:081302, 2004.

[3] K. Kainulainen, J. Maalampi, and J. T. Peltoniemi. Inert neutrinos in supernovae. *Nucl. Phys.*, B358:435–446, 1991.

[4] Esra Bulbul, Maxim Markevitch, Adam Foster, Randall K. Smith, Michael Loewenstein, and Scott W. Randall. Detection of An Unidentified Emission Line in the Stacked X-ray spectrum of Galaxy Clusters. *Astrophys. J.*, 789:13, 2014.

[5] Alexey Boyarsky, Oleg Ruchayskiy, Dmytro Iakubovskyi, and Jeroen Franse. Unidentified Line in X-Ray Spectra of the Andromeda Galaxy and Perseus Galaxy Cluster. *Phys. Rev. Lett.*, 113:251301, 2014.

[6] Feng Peng An et al. Improved Search for a Light Sterile Neutrino with the Full Configuration of the Daya Bay Experiment. *Phys. Rev. Lett.*, 117(15):151802, 2016.

[7] Y. Declais et al. Search for neutrino oscillations at 15-meters, 40-meters, and 95-meters from a nuclear power reactor at Bugey. *Nucl. Phys.*, B434:503–534, 1995.

[8] J. Ashenfelter et al. First search for short-baseline neutrino oscillations at HFIR with PROSPECT. *Phys. Rev. Lett.*, 121(25):251802, 2018.

[9] M. Tanabashi et al. Review of Particle Physics. *Phys. Rev. D*, 98(3):030001, 2018.

[10] Julien Baur, Nathalie Palanque-Delabrouille, Christophe Yeche, Alexey Boyarsky, Oleg Ruchayskiy, Eric Armengaud, and Julien Lesgourgues. Constraints from Ly-α forests on non-thermal dark matter including resonantly-produced sterile neutrinos. *JCAP*, 1712(12):013, 2017.

[11] Kenny C. Y. Ng, Brandon M. Roach, Kerstin Perez, John F. Beacom, Shunsaku Horiuchi, Roman Krivonos, and Daniel R. Wik. New Constraints on Sterile Neutrino Dark Matter from $NuSTAR$ M31 Observations. *Phys. Rev.*, D99:083005, 2019.

[12] Kerstin Perez, Kenny C. Y. Ng, John F. Beacom, Cora Hersh, Shunsaku Horiuchi, and Roman Krivonos. Almost closing the νMSM sterile neutrino dark matter window with NuSTAR. *Phys. Rev.*, D95(12):123002, 2017.

[13] A. Neronov, Denys Malyshev, and Dominique Eckert. Decaying dark matter search with NuSTAR deep sky observations. *Phys. Rev.*, D94(12):123504, 2016.

[14] Alexey Boyarsky, A. Neronov, Oleg Ruchayskiy, and M. Shaposhnikov. Constraints on sterile neutrino as a dark matter candidate from the diffuse x-ray background. *Mon. Not. Roy. Astron. Soc.*, 370:213–218, 2006.

[15] A. Gando et al. Search for Majorana Neutrinos near the Inverted Mass Hierarchy Region with KamLAND-Zen. *Phys. Rev. Lett.*, 117(8):082503, 2016. [Addendum: Phys. Rev. Lett.117,no.10,109903(2016)].

[16] D. J. Fixsen, E. S. Cheng, J. M. Gales, John C. Mather, R. A. Shafer, and E. L. Wright. The Cosmic Microwave Background spectrum from the full COBE FIRAS data set. *Astrophys. J.*, 473:576, 1996.

[17] Susanne Mertens et al. A novel detector system for KATRIN to search for keV-scale sterile neutrinos. *J. Phys.*, G46(6):065203, 2019.

[18] Fotios Megas. eV-scale Sterile Neutrino Investigation with the First Tritium KATRIN Data. *Master's Thesis*.

[19] Peter F Smith. Proposed experiments to detect keV range sterile neutrinos using energy-momentum reconstruction of beta decay or K-capture events. *New J. Phys.*, 21(5):053022, 2019.

[20] A. A. Aguilar-Arevalo et al. Significant Excess of ElectronLike Events in the MiniBooNE Short-Baseline Neutrino Experiment. *Phys. Rev. Lett.*, 121(22):221801, 2018.

[21] I Alekseev et al. Search for sterile neutrinos at the DANSS experiment. *Phys. Lett.*, B787:56–63, 2018.

[22] Y. J. Ko et al. Sterile Neutrino Search at the NEOS Experiment. *Phys. Rev. Lett.*, 118(12):121802, 2017.

[23] S. Gariazzo, C. Giunti, M. Laveder, and Y. F. Li. Model-independent $\bar{\nu}_e$ short-baseline oscillations from reactor spectral ratios. *Phys. Lett.*, B782:13–21, 2018.

[24] M. G. Betti et al. Neutrino physics with the PTOLEMY project: active neutrino properties and the light sterile case. *JCAP*, 1907:047, 2019.

[25] A. Gando, Y. Gando, T. Hachiya, A. Hayashi, S. Hayashida, H. Ikeda, K. Inoue, K. Ishidoshiro, Y. Karino, M. Koga, S. Matsuda, T. Mitsui, K. Nakamura, S. Obara, T. Oura, H. Ozaki, I. Shimizu, Y. Shirahata, J. Shirai, A. Suzuki, T. Takai, K. Tamae, Y. Teraoka, K. Ueshima, H. Watanabe, A. Kozlov, Y. Takemoto, S. Yoshida, K. Fushimi, T. I. Banks, B. E. Berger, B. K. Fujikawa, T. O'Donnell, L. A. Winslow, Y. Efremenko, H. J. Karwowski, D. M. Markoff, W. Tornow, J. A. Detwiler, S. Enomoto, and M. P. Decowski. Search for majorana neutrinos near the inverted mass hierarchy region with kamland-zen. *Phys. Rev. Lett.*, 117:082503, Aug 2016.

[26] Masamune Oguri, Jose M. Diego, Nick Kaiser, Patrick L. Kelly, and Tom Broadhurst. Understanding caustic crossings in giant arcs: Characteristic scales, event rates, and constraints on compact dark matter. *Physical Review D*, 97(2):023518, January 2018.

[27] Yacine Ali-Haïmoud and Marc Kamionkowski. Cosmic microwave background limits on accreting primordial black holes. *Phys. Rev.*, D95(4):043534, 2017.

[28] Yoshiyuki Inoue and Alexander Kusenko. New X-ray bound on density of primordial black holes. *JCAP*, 1710(10):034, 2017.

[29] B. J. Carr and M. Sakellariadou. Dynamical constraints on dark matter in compact objects. *The Astrophysical Journal*, 516(1):195–220, may 1999.

[30] Riccardo Murgia, Giulio Scelfo, Matteo Viel, and Alvise Raccanelli. Lyman-alpha Forest Constraints on Primordial Black Holes as Dark Matter. *Physical Review Letters*, 123(7):071102, August 2019.

[31] Timothy D. Brandt. Constraints on MACHO Dark Matter from Compact Stellar Systems in Ultra-faint Dwarf Galaxies. *Astrophysical Journal Letters*, 824(2):L31, June 2016.

[32] Savvas M. Koushiappas and Abraham Loeb. Dynamics of Dwarf Galaxies Disfavor Stellar-Mass Black Holes as Dark Matter. *Physical Review Letters*, 119(4):041102, July 2017.

[33] Miguel A. Monroy-Rodríguez and Christine Allen. The End of the MACHO Era, Revisited: New Limits on MACHO Masses from Halo Wide Binaries. *Astrophys. J.*, 790(2):159, August 2014.

[34] Bernard Carr and Joseph Silk. Primordial Black Holes as Generators of Cosmic Structures. *Mon. Not. Roy. Astron. Soc.*, 478(3):3756–3775, 2018.

[35] Massimo Ricotti, Jeremiah P. Ostriker, and Katherine J. Mack. Effect of Primordial Black Holes on the Cosmic Microwave Background and Cosmological Parameter Estimates. *Astrophys. J.*, 680:829, 2008.

[36] Mathieu Boudaud and Marco Cirelli. Voyager 1 $e^{\pm}$ Further Constrain Primordial Black Holes as Dark Matter. *Phys. Rev. Lett.*, 122(4):041104, 2019.

[37] Steven Clark, Bhaskar Dutta, Yu Gao, Louis E. Strigari, and Scott Watson. Planck Constraint on Relic Primordial Black Holes. *Phys. Rev. D*, 95(8):083006, 2017.

[38] B. J. Carr, Kazunori Kohri, Yuuiti Sendouda, and Jun'ichi Yokoyama. New cosmological constraints on primordial black holes. *Phys. Rev.*, D81:104019, 2010.

[39] Guillermo Ballesteros, Javier Coronado-Blázquez, and Daniele Gaggero. X-ray and gamma-ray limits on the primordial black hole abundance from Hawking radiation. *Phys. Lett. B*, 808:135624, 2020.

[40] William DeRocco and Peter W. Graham. Constraining Primordial Black Hole Abundance with the Galactic 511 keV Line. *Phys. Rev. Lett.*, 123(25):251102, 2019.

[41] Ranjan Laha. Primordial black holes as a dark matter candidate are severely constrained by the Galactic Center 511 keV gamma-ray line. *Phys. Rev. Lett.*, 123(25):251101, 2019.

[42] Basudeb Dasgupta, Ranjan Laha, and Anupam Ray. Neutrino and positron constraints on spinning primordial black hole dark matter. *Phys. Rev. Lett.*, 125(10):101101, 2020.

[43] Ranjan Laha, Julian B. Muñoz, and Tracy R. Slatyer. INTEGRAL constraints on primordial black holes and particle dark matter. *Phys. Rev. D*, 101(12):123514, 2020.

[44] Vera C. Rubin and Jr. Ford, W. Kent. Rotation of the Andromeda Nebula from a Spectroscopic Survey of Emission Regions. *Astrophysical Journal*, 159:379, February 1970.

[45] Douglas Clowe, Maruša Bradač, Anthony H. Gonzalez, Maxim Markevitch, Scott W. Randall, Christine Jones, and Dennis Zaritsky. A Direct Empirical Proof of the Existence of Dark Matter. *Astrophysical Journal Letters*, 648(2):L109–L113, September 2006.

[46] N. Aghanim et al. Planck 2018 results. VI. Cosmological parameters. 2018.

[47] Adam G. Riess, Alexei V. Filippenko, Peter Challis, Alejandro Clocchiatti, Alan Diercks, Peter M. Garnavich, Ron L. Gilliland, Craig J. Hogan, Saurabh Jha, Robert P. Kirshner, B. Leibundgut, M. M. Phillips, David Reiss, Brian P. Schmidt, Robert A. Schommer, R. Chris Smith, J. Spyromilio, Christopher Stubbs, Nicholas B. Suntzeff, and John Tonry. Observational Evidence from Supernovae for an Accelerating Universe and a Cosmological Constant. *Astronomical Journal*, 116(3):1009–1038, September 1998.

[48] S. Perlmutter, G. Aldering, G. Goldhaber, R. A. Knop, P. Nugent, P. G. Castro, S. Deustua, S. Fabbro, A. Goobar, D. E. Groom, I. M. Hook, A. G. Kim, M. Y. Kim, J. C. Lee, N. J. Nunes, R. Pain, C. R. Pennypacker, R. Quimby, C. Lidman, R. S. Ellis, M. Irwin, R. G. McMahon, P. Ruiz-Lapuente, N. Walton, B. Schaefer, B. J. Boyle, A. V. Filippenko, T. Matheson, A. S. Fruchter, N. Panagia, H. J. M. Newberg, W. J. Couch, and The Supernova Cosmology Project. Measurements of Ω and Λ from 42 High-Redshift Supernovae. *Astrophysical Journal*, 517(2):565–586, June 1999.

[49] Vardan Khachatryan et al. Search for dark matter, extra dimensions, and unparticles in monojet events in proton–proton collisions at $\sqrt{s} = 8$ TeV. *Eur. Phys. J. C*, 75(5):235, 2015.

[50] Albert M Sirunyan et al. Search for dark matter particles produced in association with a Higgs boson in proton-proton collisions at $\sqrt{\mathrm{s}} = 13$ TeV. *JHEP*, 03:025, 2020.

[51] Marc Schumann. Direct Detection of WIMP Dark Matter: Concepts and Status. *J. Phys. G*, 46(10):103003, 2019.

[52] Rouven Essig, Jeremy Mardon, and Tomer Volansky. Direct Detection of Sub-GeV Dark Matter. *Phys. Rev. D*, 85:076007, 2012.

[53] R Acciarri, M Antonello, B Baibussinov, P Benetti, F Calaprice, E Calligarich, M Cambiaghi, N Canci, C Cao, F Carbonara, F Cavanna, S Centro, M B Ceolin, A Chavarria, A Cocco, F Di Pompeo, G Fiorillo, C Galbiati, L Grandi, B Loer, G Mangano,

A Menegolli, G Meng, C Montanari, O Palamara, L Pandola, F Pietropaolo, G L Raselli, M Roncadelli, M Rossella, C Rubbia, R Saldanha, E Segreto, A M Szelc, S Ventura, and C Vignoli. The WArP experiment. *Journal of Physics: Conference Series*, 203:012006, jan 2010.

[54] E. Aprile et al. The XENON100 Dark Matter Experiment. *Astropart. Phys.*, 35:573–590, 2012.

[55] A. Badertscher et al. ArDM: first results from underground commissioning. *JINST*, 8:C09005, 2013.

[56] E. Daw, J. R. Fox, J. L. Gauvreau, C. Ghag, L. J. Harmon, M. Gold, E. Lee, D. Loomba, E. Miller, A. StJ. Murphy, S. M. Paling, J. M. Landers, M. Pipe, K. Pushkin, M. Robinson, D. P. Snowden-Ifft, N. J. C. Spooner, and D. Walker. Spin-Dependent Limits from the DRIFT-IId Directional Dark Matter Detector. *arXiv e-prints*, page arXiv:1010.3027, October 2010.

[57] Kims Collaboration, H. S. Lee, H. Bhang, J. H. Choi, I. S. Hahn, D. He, M. J. Hwang, H. J. Kim, S. C. Kim, S. K. Kim, S. Y. Kim, T. Y. Kim, Y. D. Kim, J. W. Kwak, Y. J. Kwon, J. Lee, J. H. Lee, J. I. Lee, M. J. Lee, J. Li, S. S. Myung, H. Park, H. Y. Yang, and J. J. Zhu. First limit on WIMP cross section with low background CsI($T\ell$) crystal detector. *Physics Letters B*, 633(2-3):201–208, February 2006.

[58] G. Angloher, M. Bauer, I. Bavykina, A. Bento, C. Bucci, C. Ciemniak, G. Deuter, F. von Feilitzsch, D. Hauff, P. Huff, C. Isaila, J. Jochum, M. Kiefer, M. Kimmerle, J. C. Lanfranchi, F. Petricca, S. Pfister, W. Potzel, F. Pröbst, F. Reindl, S. Roth, K. Rottler, C. Sailer, K. Schäffner, J. Schmaler, S. Scholl, W. Seidel, M. v. Sivers, L. Stodolsky, C. Strandhagen, R. Strauß, A. Tanzke, I. Usherov, S. Wawoczny, M. Willers, and A. Zöller. Results from 730 kg days of the CRESST-II Dark Matter search. *European Physical Journal C*, 72:1971, April 2012.

[59] Nataliya Skrobova. New results from the DANSS experiment. *Int. J. Mod. Phys. A*, 35(34n35):2044015, 2020.

[60] Z. Atif et al. Search for sterile neutrino oscillation using RENO and NEOS data. 11 2020.

[61] R. Acciarri et al. Design and Construction of the MicroBooNE Detector. *JINST*, 12(02):P02017, 2017.

[62] R. Acciarri et al. Long-Baseline Neutrino Facility (LBNF) and Deep Underground Neutrino Experiment (DUNE): Conceptual Design Report, Volume 1: The LBNF and DUNE Projects. 1 2016.

[63] Junji Hisano, Shigeki. Matsumoto, Mihoko M. Nojiri, and Osamu Saito. Non-perturbative effect on dark matter annihilation and gamma ray signature from galactic center. *Phys. Rev. D*, 71:063528, 2005.

[64] M. Ackermann et al. Constraining Dark Matter Models from a Combined Analysis of Milky Way Satellites with the Fermi Large Area Telescope. *Phys. Rev. Lett.*, 107:241302, 2011.

[65] Graciela B. Gelmini, Philip Lu, and Volodymyr Takhistov. Cosmological Dependence of Resonantly Produced Sterile Neutrinos. *JCAP*, 06:008, 2020.

[66] Graciela B. Gelmini, Philip Lu, and Volodymyr Takhistov. Visible Sterile Neutrinos as the Earliest Relic Probes of Cosmology. *Phys. Lett. B*, 800:135113, 2020.

[67] Graciela B. Gelmini, Philip Lu, and Volodymyr Takhistov. Cosmological Dependence of Non-resonantly Produced Sterile Neutrinos. *JCAP*, 12:047, 2019.

[68] Graciela B. Gelmini, Philip Lu, and Volodymyr Takhistov. Addendum: Cosmological dependence of non-resonantly produced sterile neutrinos. 6 2020. [Addendum: JCAP 10, A01 (2020)].

[69] Philip Lu, Volodymyr Takhistov, Graciela B. Gelmini, Kohei Hayashi, Yoshiyuki Inoue, and Alexander Kusenko. Constraining Primordial Black Holes with Dwarf Galaxy Heating. 7 2020.

[70] Y. Fukuda et al. Evidence for oscillation of atmospheric neutrinos. *Phys. Rev. Lett.*, 81:1562–1567, 1998.

[71] P. F. de Salas, M. Lattanzi, G. Mangano, G. Miele, S. Pastor, and O. Pisanti. Bounds on very low reheating scenarios after Planck. *Phys. Rev.*, D92(12):123534, 2015.

[72] Takuya Hasegawa, Nagisa Hiroshima, Kazunori Kohri, Rasmus S.L. Hansen, Thomas Tram, and Steen Hannestad. MeV-scale reheating temperature and thermalization of oscillating neutrinos by radiative and hadronic decays of massive particles. *JCAP*, 12:012, 2019.

[73] Francesco De Bernardis, Luca Pagano, and Alessandro Melchiorri. New constraints on the reheating temperature of the universe after WMAP-5. *Astropart. Phys.*, 30:192–195, 2008.

[74] Steen Hannestad. What is the lowest possible reheating temperature? *Phys. Rev.*, D70:043506, 2004.

[75] M. Kawasaki, Kazunori Kohri, and Naoshi Sugiyama. MeV scale reheating temperature and thermalization of neutrino background. *Phys. Rev.*, D62:023506, 2000.

[76] M. Kawasaki, Kazunori Kohri, and Naoshi Sugiyama. Cosmological constraints on late time entropy production. *Phys. Rev. Lett.*, 82:4168, 1999.

[77] Y. B. Zel'dovich and I. D. Novikov. The Hypothesis of Cores Retarded during Expansion and the Hot Cosmological Model. *Sov. Astron.*, 10:602, February 1967.

[78] Stephen Hawking. Gravitationally collapsed objects of very low mass. *Mon. Not. Roy. Astron. Soc.*, 152:75, 1971.

[79] Bernard J. Carr and S. W. Hawking. Black holes in the early Universe. *Mon. Not. Roy. Astron. Soc.*, 168:399–415, 1974.

[80] Juan Garcia-Bellido, Andrei D. Linde, and David Wands. Density perturbations and black hole formation in hybrid inflation. *Phys. Rev.*, D54:6040–6058, 1996.

[81] M. Yu. Khlopov. Primordial Black Holes. *Res. Astron. Astrophys.*, 10:495–528, 2010.

[82] Paul H. Frampton, Masahiro Kawasaki, Fuminobu Takahashi, and Tsutomu T. Yanagida. Primordial Black Holes as All Dark Matter. *JCAP*, 1004:023, 2010.

[83] Masahiro Kawasaki, Alexander Kusenko, Yuichiro Tada, and Tsutomu T. Yanagida. Primordial black holes as dark matter in supergravity inflation models. *Phys. Rev.*, D94(8):083523, 2016.

[84] Bernard Carr, Florian Kuhnel, and Marit Sandstad. Primordial Black Holes as Dark Matter. *Phys. Rev.*, D94(8):083504, 2016.

[85] Keisuke Inomata, Masahiro Kawasaki, Kyohei Mukaida, Yuichiro Tada, and Tsutomu T. Yanagida. Inflationary primordial black holes for the LIGO gravitational wave events and pulsar timing array experiments. *Phys. Rev. D*, 95(12):123510, 2017.

[86] Shi Pi, Ying-li Zhang, Qing-Guo Huang, and Misao Sasaki. Scalaron from R^2-gravity as a heavy field. *JCAP*, 1805(05):042, 2018.

[87] Keisuke Inomata, Masahiro Kawasaki, Kyohei Mukaida, Yuichiro Tada, and Tsutomu T. Yanagida. Inflationary Primordial Black Holes as All Dark Matter. *Phys. Rev. D*, 96(4):043504, 2017.

[88] Juan Garcia-Bellido, Marco Peloso, and Caner Unal. Gravitational Wave signatures of inflationary models from Primordial Black Hole Dark Matter. *JCAP*, 1709(09):013, 2017.

[89] Julian Georg and Scott Watson. A Preferred Mass Range for Primordial Black Hole Formation and Black Holes as Dark Matter Revisited. *JHEP*, 09:138, 2017.

[90] Keisuke Inomata, Masahiro Kawasaki, Kyohei Mukaida, and Tsutomu T. Yanagida. Double Inflation as a single origin of PBHs for all dark matter and LIGO. 2017.

[91] Bence Kocsis, Teruaki Suyama, Takahiro Tanaka, and Shuichiro Yokoyama. Hidden universality in the merger rate distribution in the primordial black hole scenario. *Astrophys. J.*, 854(1):41, 2018.

[92] Kenta Ando, Keisuke Inomata, Masahiro Kawasaki, Kyohei Mukaida, and Tsutomu T. Yanagida. Primordial black holes for the LIGO events in the axionlike curvaton model. *Phys. Rev. D*, 97(12):123512, 2018.

[93] Eric Cotner and Alexander Kusenko. Primordial black holes from supersymmetry in the early universe. *Phys. Rev. Lett.*, 119(3):031103, 2017.

[94] Eric Cotner and Alexander Kusenko. Primordial black holes from scalar field evolution in the early universe. *Phys. Rev.*, D96(10):103002, 2017.

[95] Eric Cotner, Alexander Kusenko, and Volodymyr Takhistov. Primordial Black Holes from Inflaton Fragmentation into Oscillons. *Phys. Rev.*, D98(8):083513, 2018.

[96] Misao Sasaki, Teruaki Suyama, Takahiro Tanaka, and Shuichiro Yokoyama. Primordial black holes—perspectives in gravitational wave astronomy. *Class. Quant. Grav.*, 35(6):063001, 2018.

[97] Uddipan Banik, Frank C. van den Bosch, Michael Tremmel, Anupreeta More, Giulia Despali, Surhud More, Simona Vegetti, and John P. McKean. Constraining the mass density of free-floating black holes using razor-thin lensing arcs. *Mon. Not. Roy. Astron. Soc.*, 483(2):1558–1573, 2019.

[98] F. Hoyle and R. A. Lyttleton. The effect of interstellar matter on climatic variation. *Proceedings of the Cambridge Philosophical Society*, 35(3):405, January 1939.

[99] Eric Cotner, Alexander Kusenko, Misao Sasaki, and Volodymyr Takhistov. Analytic Description of Primordial Black Hole Formation from Scalar Field Fragmentation. *JCAP*, 1910(10):077, 2019.

[100] Alexander Kusenko, Misao Sasaki, Sunao Sugiyama, Masahiro Takada, Volodymyr Takhistov, and Edoardo Vitagliano. Exploring Primordial Black Holes from Multiverse with Optical Telescopes. 1 2020.

[101] Rachel Bean and Joao Magueijo. Could supermassive black holes be quintessential primordial black holes? *Phys. Rev.*, D66:063505, 2002.

[102] Masahiro Kawasaki, Alexander Kusenko, and Tsutomu T. Yanagida. Primordial seeds of supermassive black holes. *Phys. Lett.*, B711:1–5, 2012.

[103] Sebastien Clesse and Juan Garcia-Bellido. Massive Primordial Black Holes from Hybrid Inflation as Dark Matter and the seeds of Galaxies. *Phys. Rev.*, D92(2):023524, 2015.

[104] S.W. Hawking. Particle Creation by Black Holes. *Commun. Math. Phys.*, 43:199–220, 1975. [Erratum: Commun.Math.Phys. 46, 206 (1976)].

[105] B. T. Cleveland, Timothy Daily, Raymond Davis, Jr., James R. Distel, Kenneth Lande, C. K. Lee, Paul S. Wildenhain, and Jack Ullman. Measurement of the solar electron neutrino flux with the Homestake chlorine detector. *Astrophys. J.*, 496:505–526, 1998.

[106] J. N. Abdurashitov et al. Measurement of the solar neutrino capture rate with gallium metal. III: Results for the 2002–2007 data-taking period. *Phys. Rev.*, C80:015807, 2009.

[107] M. Altmann et al. Complete results for five years of GNO solar neutrino observations. *Phys. Lett.*, B616:174–190, 2005.

[108] W. Hampel et al. GALLEX solar neutrino observations: Results for GALLEX IV. *Phys. Lett.*, B447:127–133, 1999.

[109] B. Aharmim et al. Electron energy spectra, fluxes, and day-night asymmetries of B-8 solar neutrinos from measurements with NaCl dissolved in the heavy-water detector at the Sudbury Neutrino Observatory. *Phys. Rev.*, C72:055502, 2005.

[110] K. Abe et al. Solar Neutrino Measurements in Super-Kamiokande-IV. *Phys. Rev.*, D94(5):052010, 2016.

[111] T. Araki et al. Measurement of neutrino oscillation with KamLAND: Evidence of spectral distortion. *Phys. Rev. Lett.*, 94:081801, 2005.

[112] F. P. An et al. Observation of electron-antineutrino disappearance at Daya Bay. *Phys. Rev. Lett.*, 108:171803, 2012.

[113] Y. Abe et al. First Measurement of θ_{13} from Delayed Neutron Capture on Hydrogen in the Double Chooz Experiment. *Phys. Lett.*, B723:66–70, 2013.

[114] J. K. Ahn et al. Observation of Reactor Electron Antineutrino Disappearance in the RENO Experiment. *Phys. Rev. Lett.*, 108:191802, 2012.

[115] M. H. Ahn et al. Measurement of Neutrino Oscillation by the K2K Experiment. *Phys. Rev.*, D74:072003, 2006.

[116] P. Adamson et al. Measurement of Neutrino and Antineutrino Oscillations Using Beam and Atmospheric Data in MINOS. *Phys. Rev. Lett.*, 110(25):251801, 2013.

[117] K. Abe et al. Precise Measurement of the Neutrino Mixing Parameter θ_{23} from Muon Neutrino Disappearance in an Off-Axis Beam. *Phys. Rev. Lett.*, 112(18):181801, 2014.

[118] N. Agafonova et al. Evidence for $\nu_\mu \to \nu_\tau$ appearance in the CNGS neutrino beam with the OPERA experiment. *Phys. Rev.*, D89(5):051102, 2014.

[119] P. Adamson et al. First measurement of muon-neutrino disappearance in NOvA. *Phys. Rev.*, D93(5):051104, 2016.

[120] M. G. Aartsen et al. Determining neutrino oscillation parameters from atmospheric muon neutrino disappearance with three years of IceCube DeepCore data. *Phys. Rev.*, D91(7):072004, 2015.

[121] A. Aguilar-Arevalo et al. Evidence for neutrino oscillations from the observation of anti-neutrino(electron) appearance in a anti-neutrino(muon) beam. *Phys. Rev.*, D64:112007, 2001.

[122] A. A. Aguilar-Arevalo et al. Improved Search for $\bar{\nu}_\mu \to \bar{\nu}_e$ Oscillations in the MiniBooNE Experiment. *Phys. Rev. Lett.*, 110:161801, 2013.

[123] Joel Kostensalo, Jouni Suhonen, Carlo Giunti, and Praveen C. Srivastava. The gallium anomaly revisited. *Phys. Lett.*, B795:542–547, 2019.

[124] John N. Bahcall, P. I. Krastev, and E. Lisi. Limits on electron-neutrino oscillations from the GALLEX Cr-51 source experiment. *Phys. Lett.*, B348:121–123, 1995.

[125] J. N. Abdurashitov et al. Measurement of the response of a Ga solar neutrino experiment to neutrinos from an Ar-37 source. *Phys. Rev.*, C73:045805, 2006.

[126] F. P. An et al. Evolution of the Reactor Antineutrino Flux and Spectrum at Daya Bay. *Phys. Rev. Lett.*, 118(25):251801, 2017.

[127] Patrick Huber. NEOS Data and the Origin of the 5 MeV Bump in the Reactor Antineutrino Spectrum. *Phys. Rev. Lett.*, 118(4):042502, 2017.

[128] G. Mention, M. Fechner, Th. Lasserre, Th. A. Mueller, D. Lhuillier, M. Cribier, and A. Letourneau. The Reactor Antineutrino Anomaly. *Phys. Rev.*, D83:073006, 2011.

[129] Mona Dentler, Alvaro Hernandez-Cabezudo, Joachim Kopp, Pedro A. N. Machado, Michele Maltoni, Ivan Martinez-Soler, and Thomas Schwetz. Updated Global Analysis of Neutrino Oscillations in the Presence of eV-Scale Sterile Neutrinos. *JHEP*, 08:010, 2018.

[130] Jiajun Liao, Danny Marfatia, and Kerry Whisnant. MiniBooNE, MINOS+ and IceCube data imply a baroque neutrino sector. *Phys. Rev.*, D99(1):015016, 2019.

[131] A. Boyarsky, M. Drewes, T. Lasserre, S. Mertens, and O. Ruchayskiy. Sterile Neutrino Dark Matter. *Prog. Part. Nucl. Phys.*, 104:1–45, 2019.

[132] Alexey Boyarsky, Oleg Ruchayskiy, and Dmytro Iakubovskyi. A Lower bound on the mass of Dark Matter particles. *JCAP*, 0903:005, 2009.

[133] A. Palazzo, D. Cumberbatch, A. Slosar, and J. Silk. Sterile neutrinos as subdominant warm dark matter. *Phys. Rev.*, D76:103511, 2007.

[134] George M. Fuller, Alexander Kusenko, Irina Mocioiu, and Silvia Pascoli. Pulsar kicks from a dark-matter sterile neutrino. *Phys. Rev.*, D68:103002, 2003.

[135] Scott Dodelson and Lawrence M. Widrow. Sterile-neutrinos as dark matter. *Phys. Rev. Lett.*, 72:17–20, 1994.

[136] Xiang-Dong Shi and George M. Fuller. A New dark matter candidate: Nonthermal sterile neutrinos. *Phys. Rev. Lett.*, 82:2832–2835, 1999.

[137] Kevork Abazajian, George M. Fuller, and Mitesh Patel. Sterile neutrino hot, warm, and cold dark matter. *Phys. Rev.*, D64:023501, 2001.

[138] Kevork Abazajian, Nicole F. Bell, George M. Fuller, and Yvonne Y. Y. Wong. Cosmological lepton asymmetry, primordial nucleosynthesis, and sterile neutrinos. *Phys. Rev.*, D72:063004, 2005.

[139] Kalliopi Petraki and Alexander Kusenko. Dark-matter sterile neutrinos in models with a gauge singlet in the Higgs sector. *Phys. Rev.*, D77:065014, 2008.

[140] Thomas Rehagen and Graciela B. Gelmini. Effects of kination and scalar-tensor cosmologies on sterile neutrinos. *JCAP*, 1406:044, 2014.

[141] Kevork N. Abazajian. Sterile neutrinos in cosmology. *Phys. Rept.*, 711-712:1–28, 2017.

[142] Edward W. Kolb and Michael S. Turner. The Early Universe. *Front. Phys.*, 69:1–547, 1990.

[143] Lars Husdal. On Effective Degrees of Freedom in the Early Universe. *Galaxies*, 4(4):78, 2016.

[144] Sz. Borsanyi et al. Calculation of the axion mass based on high-temperature lattice quantum chromodynamics. *Nature*, 539(7627):69–71, 2016.

[145] Manuel Drees, Fazlollah Hajkarim, and Ernany Rossi Schmitz. The Effects of QCD Equation of State on the Relic Density of WIMP Dark Matter. *JCAP*, 1506(06):025, 2015.

[146] R. Catena, N. Fornengo, M. Pato, L. Pieri, and A. Masiero. Thermal Relics in Modified Cosmologies: Bounds on Evolution Histories of the Early Universe and Cosmological Boosts for PAMELA. *Phys. Rev.*, D81:123522, 2010.

[147] Graciela Gelmini and Paolo Gondolo. DM Production Mechanisms. pages 121–141, 2010.

[148] Marc Kamionkowski and Michael S. Turner. THERMAL RELICS: DO WE KNOW THEIR ABUNDANCES? *Phys. Rev.*, D42:3310–3320, 1990.

[149] Pierre Salati. Quintessence and the relic density of neutralinos. *Phys. Lett.*, B571:121–131, 2003.

[150] G. Lambiase, S. Mohanty, and An. Stabile. PeV IceCube signals and Dark Matter relic abundance in modified cosmologies. *Eur. Phys. J.*, C78(4):350, 2018.

[151] Francesco D'Eramo, Nicolas Fernandez, and Stefano Profumo. When the Universe Expands Too Fast: Relentless Dark Matter. *JCAP*, 1705(05):012, 2017.

[152] Justin Khoury, Burt A. Ovrut, Paul J. Steinhardt, and Neil Turok. The Ekpyrotic universe: Colliding branes and the origin of the hot big bang. *Phys. Rev.*, D64:123522, 2001.

[153] Lisa Randall and Raman Sundrum. An Alternative to compactification. *Phys. Rev. Lett.*, 83:4690–4693, 1999.

[154] Mia Schelke, Riccardo Catena, Nicolao Fornengo, Antonio Masiero, and Massimo Pietroni. Constraining pre Big-Bang-Nucleosynthesis Expansion using Cosmic Antiprotons. *Phys. Rev.*, D74:083505, 2006.

[155] Boris Spokoiny. Deflationary universe scenario. *Phys. Lett.*, B315:40–45, 1993.

[156] Michael Joyce. Electroweak Baryogenesis and the Expansion Rate of the Universe. *Phys. Rev.*, D55:1875–1878, 1997.

[157] Stefano Profumo and Piero Ullio. SUSY dark matter and quintessence. *JCAP*, 0311:006, 2003.

[158] C. Pallis. Quintessential kination and cold dark matter abundance. *JCAP*, 0510:015, 2005.

[159] Riccardo Catena, N. Fornengo, A. Masiero, Massimo Pietroni, and Francesca Rosati. Dark matter relic abundance and scalar - tensor dark energy. *Phys. Rev.*, D70:063519, 2004.

[160] Alexei A. Starobinsky. A New Type of Isotropic Cosmological Models Without Singularity. *Phys. Lett.*, B91:99–102, 1980. [,771(1980)].

[161] S. Capozziello, V. Galluzzi, G. Lambiase, and L. Pizza. Cosmological evolution of thermal relic particles in $f(R)$ gravity. *Phys. Rev.*, D92(8):084006, 2015.

[162] David I. Santiago, Dimitri Kalligas, and Robert V. Wagoner. Scalar - tensor cosmologies and their late time evolution. *Phys. Rev.*, D58:124005, 1998.

[163] Tomi Koivisto, Danielle Wills, and Ivonne Zavala. Dark D-brane Cosmology. *JCAP*, 1406:036, 2014.

[164] Riccardo Catena, Nicolao Fornengo, Antonio Masiero, Massimo Pietroni, and Mia Schelke. Enlarging mSUGRA parameter space by decreasing pre-BBN Hubble rate in Scalar-Tensor Cosmologies. *JHEP*, 10:003, 2008.

[165] Jeremy Sakstein and Bhuvnesh Jain. Implications of the Neutron Star Merger GW170817 for Cosmological Scalar-Tensor Theories. *Phys. Rev. Lett.*, 119(25):251303, 2017.

[166] Graciela B. Gelmini and Paolo Gondolo. Neutralino with the right cold dark matter abundance in (almost) any supersymmetric model. *Phys. Rev.*, D74:023510, 2006.

[167] Graciela Gelmini, Paolo Gondolo, Adrian Soldatenko, and Carlos E. Yaguna. The Effect of a late decaying scalar on the neutralino relic density. *Phys. Rev.*, D74:083514, 2006.

[168] T. Moroi, Masahiro Yamaguchi, and T. Yanagida. On the solution to the Polonyi problem with 0 (10-TeV) gravitino mass in supergravity. *Phys. Lett.*, B342:105–110, 1995.

[169] M. Kawasaki, T. Moroi, and T. Yanagida. Constraint on the reheating temperature from the decay of the Polonyi field. *Phys. Lett.*, B370:52–58, 1996.

[170] Takeo Moroi and Lisa Randall. Wino cold dark matter from anomaly mediated SUSY breaking. *Nucl. Phys.*, B570:455–472, 2000.

[171] Mu-Chun Chen and Volodymyr Takhistov. Baryogenesis, Dark Matter, and Flavor Structure in Non-thermal Moduli Cosmology. *JHEP*, 05:101, 2019.

[172] Ryuichiro Kitano, Hitoshi Murayama, and Michael Ratz. Unified origin of baryons and dark matter. *Phys. Lett.*, B669:145–149, 2008.

[173] Manuel Drees and Fazlollah Hajkarim. Dark Matter Production in an Early Matter Dominated Era. *JCAP*, 1802(02):057, 2018.

[174] Masaaki Fujii and Koichi Hamaguchi. Nonthermal dark matter via Affleck-Dine baryogenesis and its detection possibility. *Phys. Rev.*, D66:083501, 2002.

[175] Carlos E. Yaguna. Sterile neutrino production in models with low reheating temperatures. *JHEP*, 06:002, 2007.

[176] Graciela Gelmini, Efunwande Osoba, Sergio Palomares-Ruiz, and Silvia Pascoli. MeV sterile neutrinos in low reheating temperature cosmological scenarios. *JCAP*, 0810:029, 2008.

[177] A. D. Dolgov. Neutrinos in cosmology. *Phys. Rept.*, 370:333–535, 2002.

[178] Riccardo Barbieri and A. Dolgov. Bounds on Sterile-neutrinos from Nucleosynthesis. *Phys. Lett.*, B237:440–445, 1990.

[179] Kimmo Kainulainen. Light Singlet Neutrinos and the Primordial Nucleosynthesis. *Phys. Lett.*, B244:191–195, 1990.

[180] Takuya Hasegawa, Nagisa Hiroshima, Kazunori Kohri, Rasmus S.L. Hansen, Thomas Tram, and Steen Hannestad. MeV-scale reheating temperature and cosmological production of light sterile neutrinos. 3 2020.

[181] Steen Hannestad, Irene Tamborra, and Thomas Tram. Thermalisation of light sterile neutrinos in the early universe. *JCAP*, 07:025, 2012.

[182] Matteo Viel, Julien Lesgourgues, Martin G. Haehnelt, Sabino Matarrese, and Antonio Riotto. Constraining warm dark matter candidates including sterile neutrinos and light gravitinos with WMAP and the Lyman-alpha forest. *Phys. Rev.*, D71:063534, 2005.

[183] Gianpiero Mangano, Gennaro Miele, Sergio Pastor, Teguayco Pinto, Ofelia Pisanti, and Pasquale D. Serpico. Relic neutrino decoupling including flavor oscillations. *Nucl. Phys.*, B729:221–234, 2005.

[184] Pablo F. de Salas and Sergio Pastor. Relic neutrino decoupling with flavour oscillations revisited. *JCAP*, 1607(07):051, 2016.

[185] Graciela B. Gelmini, Alexander Kusenko, and Volodymyr Takhistov. Hints of Sterile Neutrinos in Recent Measurements of the Hubble Parameter. 2019.

[186] Planck Collaboration, P. A. R. Ade, N. Aghanim, et al. Planck 2015 results. XIII. Cosmological parameters. *Astron. Astrophys.*, 594:A13, September 2016.

[187] John R. Ellis, G. B. Gelmini, Jorge L. Lopez, Dimitri V. Nanopoulos, and Subir Sarkar. Astrophysical constraints on massive unstable neutral relic particles. *Nucl. Phys.*, B373:399–437, 1992.

[188] W. Hu and J. Silk. Thermalization constraints and spectral distortions for massive unstable relic particles. *Phys. Rev. Lett.*, 70:2661–2664, 1993.

[189] Georg G. Raffelt and Shun Zhou. Supernova bound on keV-mass sterile neutrinos reexamined. *Phys. Rev.*, D83:093014, 2011.

[190] Carlos A. Arguelles, Vedran Brdar, and Joachim Kopp. Production of keV Sterile Neutrinos in Supernovae: New Constraints and Gamma Ray Observables. *Phys. Rev.*, D99(4):043012, 2019.

[191] R. Shrock. Decay $L^0 \to \nu_l \gamma$ in gauge theories of weak and electromagnetic interactions. *Phys. Rev.*, D9:743–748, 1974.

[192] Palash B. Pal and Lincoln Wolfenstein. Radiative Decays of Massive Neutrinos. *Phys. Rev.*, D25:766, 1982.

[193] Christopher Dessert, Nicholas L. Rodd, and Benjamin R. Safdi. Evidence against the decaying dark matter interpretation of the 3.5 keV line from blank sky observations. 2018.

[194] A. Boyarsky, D. Iakubovskyi, O. Ruchayskiy, and D. Savchenko. Surface brightness profile of the 3.5 keV line in the Milky Way halo. 2018.

[195] M. G. Aartsen et al. Searches for Sterile Neutrinos with the IceCube Detector. *Phys. Rev. Lett.*, 117(7):071801, 2016.

[196] P. Adamson et al. Search for sterile neutrinos in MINOS and MINOS+ using a two-detector fit. *Phys. Rev. Lett.*, 122(9):091803, 2019.

[197] J. Wolf. The KATRIN Neutrino Mass Experiment. *Nucl. Instrum. Meth.*, A623:442–444, 2010.

[198] Susanne Mertens. Status of the KATRIN Experiment and Prospects to Search for keV-mass Sterile Neutrinos in Tritium β-decay. *Phys. Procedia*, 61:267–273, 2015.

[199] Asmaa Abada, Alvaro Hernandez-Cabezudo, and Xabier Marcano. Beta and Neutrinoless Double Beta Decays with KeV Sterile Fermions. *JHEP*, 01:041, 2019.

[200] Chad T. Kishimoto and George M. Fuller. Lepton Number-Driven Sterile Neutrino Production in the Early Universe. *Phys. Rev.*, D78:023524, 2008.

[201] Gianpiero Mangano, Gennaro Miele, Sergio Pastor, Ofelia Pisanti, and Srdjan Sarikas. Updated BBN bounds on the cosmological lepton asymmetry for non-zero θ_{13}. *Phys. Lett.*, B708:1–5, 2012.

[202] Gabriela Barenboim, William H. Kinney, and Wan-Il Park. Resurrection of large lepton number asymmetries from neutrino flavor oscillations. *Phys. Rev.*, D95(4):043506, 2017.

[203] Alexey Boyarsky, Julien Lesgourgues, Oleg Ruchayskiy, and Matteo Viel. Realistic sterile neutrino dark matter with keV mass does not contradict cosmological bounds. *Phys. Rev. Lett.*, 102:201304, 2009.

[204] Chad T. Kishimoto, George M. Fuller, and Christel J. Smith. Coherent Active-Sterile Neutrino Flavor Transformation in the Early Universe. *Phys. Rev. Lett.*, 97:141301, 2006.

[205] M. Laine and M. Shaposhnikov. Sterile neutrino dark matter as a consequence of nuMSM-induced lepton asymmetry. *JCAP*, 0806:031, 2008.

[206] S. P. Mikheyev and A. Yu. Smirnov. Resonance Amplification of Oscillations in Matter and Spectroscopy of Solar Neutrinos. *Sov. J. Nucl. Phys.*, 42:913–917, 1985. [,305(1986)].

[207] L. Wolfenstein. Neutrino Oscillations in Matter. *Phys. Rev.*, D17:2369–2374, 1978. [,294(1977)].

[208] Kevork N. Abazajian. Resonantly Produced 7 keV Sterile Neutrino Dark Matter Models and the Properties of Milky Way Satellites. *Phys. Rev. Lett.*, 112(16):161303, 2014.

[209] Ninetta Saviano, Alessandro Mirizzi, Ofelia Pisanti, Pasquale Dario Serpico, Gianpiero Mangano, and Gennaro Miele. Multi-momentum and multi-flavour active-sterile neutrino oscillations in the early universe: role of neutrino asymmetries and effects on nucleosynthesis. *Phys. Rev.*, D87:073006, 2013.

[210] Shouvik Roy Choudhury and Sandhya Choubey. Constraining light sterile neutrino mass with the BICEP2/Keck Array 2014 B-mode polarization data. *Eur. Phys. J.*, C79(7):557, 2019.

[211] Cristina Benso, Vedran Brdar, Manfred Lindner, and Werner Rodejohann. Prospects for Finding Sterile Neutrino Dark Matter at KATRIN. 2019.

[212] F. Bezrukov, A. Chudaykin, and D. Gorbunov. Hiding an elephant: heavy sterile neutrino with large mixing angle does not contradict cosmology. *JCAP*, 1706(06):051, 2017.

[213] Yasaman Farzan. Ultra-light scalar saving the 3+1 neutrino scheme from the cosmological bounds. *Phys. Lett.*, B797:134911, 2019.

[214] James M. Cline. Viable secret neutrino interactions with ultralight dark matter. 2019.

[215] Julien Lesgourgues and Sergio Pastor. Massive neutrinos and cosmology. *Phys. Rept.*, 429:307–379, 2006.

[216] K. N. Abazajian et al. Neutrino Physics from the Cosmic Microwave Background and Large Scale Structure. *Astropart. Phys.*, 63:66–80, 2015.

[217] Kevork N. Abazajian et al. CMB-S4 Science Book, First Edition. 2016.

[218] Andrey Katz, Joachim Kopp, Sergey Sibiryakov, and Wei Xue. Femtolensing by Dark Matter Revisited. *JCAP*, 12:005, 2018.

[219] Nolan Smyth, Stefano Profumo, Samuel English, Tesla Jeltema, Kevin McKinnon, and Puragra Guhathakurta. Updated Constraints on Asteroid-Mass Primordial Black Holes as Dark Matter. *Phys. Rev. D*, 101(6):063005, 2020.

[220] Paulo Montero-Camacho, Xiao Fang, Gabriel Vasquez, Makana Silva, and Christopher M. Hirata. Revisiting constraints on asteroid-mass primordial black holes as dark matter candidates. *JCAP*, 1908:031, 2019.

[221] George M. Fuller, Alexander Kusenko, and Volodymyr Takhistov. Primordial Black Holes and r-Process Nucleosynthesis. *Phys. Rev. Lett.*, 119(6):061101, 2017.

[222] Volodymyr Takhistov. Positrons from Primordial Black Hole Microquasars and Gamma-ray Bursts. *Phys. Lett.*, B789:538–544, 2019.

[223] Volodymyr Takhistov. Transmuted Gravity Wave Signals from Primordial Black Holes. *Phys. Lett.*, B782:77–82, 2018.

[224] B. P. Abbott et al. Observation of Gravitational Waves from a Binary Black Hole Merger. *Phys. Rev. Lett.*, 116(6):061102, 2016.

[225] B. P. Abbott et al. GW151226: Observation of Gravitational Waves from a 22-Solar-Mass Binary Black Hole Coalescence. *Phys. Rev. Lett.*, 116(24):241103, 2016.

[226] Benjamin P. Abbott et al. GW170104: Observation of a 50-Solar-Mass Binary Black Hole Coalescence at Redshift 0.2. *Phys. Rev. Lett.*, 118(22):221101, 2017.

[227] Takashi Nakamura, Misao Sasaki, Takahiro Tanaka, and Kip S. Thorne. Gravitational waves from coalescing black hole MACHO binaries. *Astrophys. J. Lett.*, 487:L139–L142, 1997.

[228] Simeon Bird, Ilias Cholis, Julian B. Muñoz, Yacine Ali-Haïmoud, Marc Kamionkowski, Ely D. Kovetz, Alvise Raccanelli, and Adam G. Riess. Did LIGO detect dark matter? *Phys. Rev. Lett.*, 116(20):201301, 2016.

[229] Martti Raidal, Ville Vaskonen, and Hardi Veermäe. Gravitational Waves from Primordial Black Hole Mergers. *JCAP*, 09:037, 2017.

[230] Yu N. Eroshenko. Gravitational waves from primordial black holes collisions in binary systems. *J. Phys. Conf. Ser.*, 1051(1):012010, 2018.

[231] Misao Sasaki, Teruaki Suyama, Takahiro Tanaka, and Shuichiro Yokoyama. Primordial Black Hole Scenario for the Gravitational-Wave Event GW150914. *Phys. Rev. Lett.*, 117(6):061101, 2016.

[232] Sebastien Clesse and Juan García-Bellido. Detecting the gravitational wave background from primordial black hole dark matter. *Phys. Dark Univ.*, 18:105–114, 2017.

[233] B. J. Carr and M. Sakellariadou. Dynamical Constraints on Dark Matter in Compact Objects. *Astrophys. J.*, 516(1):195–220, May 1999.

[234] C. G. Lacey and J. P. Ostriker. Massive black holes in galactic halos ? *Astrophys. J.*, 299:633–652, December 1985.

[235] Tomonori Totani. Size Evolution of Early-Type Galaxies and Massive Compact Objects as Dark Matter. *PASJ*, 62:L1, February 2010.

[236] Daniele Gaggero, Gianfranco Bertone, Francesca Calore, Riley M. T. Connors, Mark Lovell, Sera Markoff, and Emma Storm. Searching for Primordial Black Holes in the radio and X-ray sky. *Phys. Rev. Lett.*, 118(24):241101, 2017.

[237] Amit Bhoonah, Joseph Bramante, Fatemeh Elahi, and Sarah Schon. Calorimetric Dark Matter Detection With Galactic Center Gas Clouds. *Phys. Rev. Lett.*, 121(13):131101, 2018.

[238] Glennys R. Farrar, Felix J. Lockman, N.M. McClure-Griffiths, and Digvijay Wadekar. Comment on the paper "Calorimetric Dark Matter Detection with Galactic Center Gas Clouds". *Phys. Rev. Lett.*, 124(2):029001, 2020.

[239] Digvijay Wadekar and Glennys R. Farrar. First direct astrophysical constraints on dark matter interactions with ordinary matter at very low velocities. 2019.

[240] Don N. Page. Particle Emission Rates from a Black Hole: Massless Particles from an Uncharged, Nonrotating Hole. *Phys. Rev. D*, 13:198–206, 1976.

[241] Don N. Page. Particle Emission Rates from a Black Hole. 3. Charged Leptons from a Nonrotating Hole. *Phys. Rev. D*, 16:2402–2411, 1977.

[242] Alexandre Arbey, Jérémy Auffinger, and Joseph Silk. Constraining primordial black hole masses with the isotropic gamma ray background. *Phys. Rev. D*, 101(2):023010, 2020.

[243] Patrick Stöcker, Michael Krämer, Julien Lesgourgues, and Vivian Poulin. Exotic energy injection with ExoCLASS: Application to the Higgs portal model and evaporating black holes. *JCAP*, 03:018, 2018.

[244] Harry Poulter, Yacine Ali-Haïmoud, Jan Hamann, Martin White, and Anthony G. Williams. CMB constraints on ultra-light primordial black holes with extended mass distributions. 7 2019.

[245] Sandeep Kumar Acharya and Rishi Khatri. CMB and BBN constraints on evaporating primordial black holes revisited. *JCAP*, 06:018, 2020.

[246] P.N. Okele and M.J. Rees. Observational consequences of positron production by evaporating black holes. *Astron. Astrophys.*, 81:263–264, 1980.

[247] PN Okeke. The primary source and the fates of galactic positrons. *Astrophysics and Space Science*, 71(2):371–375, 1980.

[248] Jane H. MacGibbon and Bernard J. Carr. Cosmic rays from primordial black holes. *Astrophys. J.*, 371:447–469, 1991.

[249] Cosimo Bambi, Alexander D. Dolgov, and Alexey A. Petrov. Primordial black holes and the observed Galactic 511-keV line. *Phys. Lett. B*, 670:174–178, 2008. [Erratum: Phys.Lett.B 681, 504–504 (2009)].

[250] Takeshi Chiba and Shuichiro Yokoyama. Spin Distribution of Primordial Black Holes. *PTEP*, 2017(8):083E01, 2017.

[251] V. De Luca, V. Desjacques, G. Franciolini, A. Malhotra, and A. Riotto. The initial spin probability distribution of primordial black holes. *JCAP*, 05:018, 2019.

[252] Mehrdad Mirbabayi, Andrei Gruzinov, and Jorge Noreña. Spin of Primordial Black Holes. *JCAP*, 03:017, 2020.

[253] V. De Luca, G. Franciolini, P. Pani, and A. Riotto. The evolution of primordial black holes and their final observable spins. *JCAP*, 04:052, 2020.

[254] Tomohiro Harada, Chul-Moon Yoo, Kazunori Kohri, Ken-ichi Nakao, and Sanjay Jhingan. Primordial black hole formation in the matter-dominated phase of the Universe. *Astrophys. J.*, 833(1):61, 2016.

[255] Takafumi Kokubu, Koutarou Kyutoku, Kazunori Kohri, and Tomohiro Harada. Effect of Inhomogeneity on Primordial Black Hole Formation in the Matter Dominated Era. *Phys. Rev. D*, 98(12):123024, 2018.

[256] Eric Cotner and Alexander Kusenko. Astrophysical constraints on dark-matter Q-balls in the presence of baryon-violating operators. *Phys. Rev.*, D94(12):123006, 2016.

[257] Don N. Page. Particle Emission Rates from a Black Hole. 2. Massless Particles from a Rotating Hole. *Phys. Rev. D*, 14:3260–3273, 1976.

[258] Brett E. Taylor, Chris M. Chambers, and William A. Hiscock. Evaporation of a Kerr black hole by emission of scalar and higher spin particles. *Phys. Rev. D*, 58:044012, 1998.

[259] Ruifeng Dong, William H Kinney, and Dejan Stojkovic. Gravitational wave production by Hawking radiation from rotating primordial black holes. *JCAP*, 10:034, 2016.

[260] Alexandre Arbey, Jérémy Auffinger, and Joseph Silk. Evolution of primordial black hole spin due to Hawking radiation. *Mon. Not. Roy. Astron. Soc.*, 494(1):1257–1262, 2020.

[261] Florian Kuhnel. Enhanced Detectability of Spinning Primordial Black Holes. *Eur. Phys. J. C*, 80(3):243, 2020.

[262] Yang Bai and Nicholas Orlofsky. Primordial Extremal Black Holes as Dark Matter. *Phys. Rev. D*, 101(5):055006, 2020.

[263] Hyungjin Kim. A constraint on light primordial black holes from the interstellar medium temperature. 7 2020.

[264] Eric Agol and Marc Kamionkowski. X-rays from isolated black holes in the Milky Way. *Mon. Not. Roy. Astron. Soc.*, 334:553, 2002.

[265] H. Bondi and F. Hoyle. On the mechanism of accretion by stars. *Mon. Not. Roy. Astron. Soc.*, 104:273, January 1944.

[266] H. Bondi. On spherically symmetrical accretion. *Mon. Not. Roy. Astron. Soc.*, 112:195, January 1952.

[267] Minghao Guo, Kohei Inayoshi, Tomonari Michiyama, and Luis C. Ho. Hunting for wandering massive black holes. 6 2020.

[268] S. Kato, J. Fukue, and S. Mineshige. *Black-Hole Accretion Disks — Towards a New Paradigm —*. 2008.

[269] N. I. Shakura and R. A. Sunyaev. Reprint of 1973A&A....24..337S. Black holes in binary systems. Observational appearance. *Astronomy and Astrophysics*, 500:33–51, June 1973.

[270] S. L. Shapiro and A. P. Lightman. Black holes in X-ray binaries: marginal existence and rotation reversals of accretion disks. *Astrophys. J.*, 204:555–560, March 1976.

[271] Ramesh Narayan and In-su Yi. Advection dominated accretion: A Selfsimilar solution. *Astrophys. J. Lett.*, 428:L13, 1994.

[272] Feng Yuan and Ramesh Narayan. Hot Accretion Flows Around Black Holes. *Annual Review of Astronomy and Astrophysics*, 52:529–588, August 2014.

[273] Jian-Min Wang, Ewa Szuszkiewicz, Fang-Jun Lu, and You-Yuan Zhou. Emergent Spectra from Slim Accretion Disks in Active Galactic Nuclei. *Astrophys. J.*, 522(2):839–845, September 1999.

[274] H. A. Bethe and E. E. Salpeter. *Quantum Mechanics of One- and Two-Electron Systems*, pages 88–436. Springer Berlin Heidelberg, Berlin, Heidelberg, 1957.

[275] I. M. Band, M. B. Trzhaskovskaia, D. A. Verner, and D. G. Iakovlev. K-shell photoionization cross sections - Calculations and simple fitting formulae. *Astron. Astrophys.*, 237(1):267–269, October 1990.

[276] K.A. Olive. Review of particle physics. *Chinese Physics C*, 38(9):090001, aug 2014.

[277] J. E. Pringle. Accretion discs in astrophysics. *Annual Review of Astronomy and Astrophysics*, 19:137–162, January 1981.

[278] Feng Yuan, Eliot Quataert, and Ramesh Narayan. Nonthermal Electrons in Radiatively Inefficient Accretion Flow Models of Sagittarius A*. *Astrophys. J.*, 598(1):301–312, November 2003.

[279] Rohan Mahadevan. Scaling laws for advection dominated flows: Applications to low luminosity galactic nuclei. *Astrophys. J.*, 477:585, 1997.

[280] Ramesh Narayan and Insu Yi. Advection-dominated Accretion: Underfed Black Holes and Neutron Stars. *Astrophys. J.*, 452:710, October 1995.

[281] James Binney and Scott Tremaine. *Galactic Dynamics: Second Edition.* 2008.

[282] Eve C. Ostriker. Dynamical Friction in a Gaseous Medium. *Astrophys. J.*, 513(1):252–258, March 1999.

[283] Roger D. Blandford and Mitchell C. Begelman. On the fate of gas accreting at a low rate on to a black hole. *Monthly Notices of the Royal Astronomical Society*, 303(1):L1–L5, February 1999.

[284] Tomonori Totani. A RIAF Interpretation for the Past Higher Activity of the Galactic Center Black Hole and the 511 keV Annihilation Emission. *Publications of the Astronomical Society of Japan*, 58:965–977, December 2006.

[285] Feng Yuan, Defu Bu, and Maochun Wu. Numerical Simulation of Hot Accretion Flows. II. Nature, Origin, and Properties of Outflows and their Possible Observational Applications. *Astrophys. J.*, 761(2):130, December 2012.

[286] Fu-Guo Xie and Feng Yuan. The Radiative Efficiency of Hot Accretion Flows. *Mon. Not. Roy. Astron. Soc.*, 427:1580, 2012.

[287] Bijia Pang, Ue-Li Pen, Christopher D. Matzner, Stephen R. Green, and Matthias Liebendörfer. Numerical parameter survey of non-radiative black hole accretion: flow structure and variability of the rotation measure. *Mon. Not. Roy. Astron. Soc.*, 415(2):1228–1239, August 2011.

[288] Jason Li, Jeremiah Ostriker, and Rashid Sunyaev. Rotating Accretion Flows: From Infinity to the Black Hole. *Astrophys. J.*, 767(2):105, April 2013.

[289] Feng Yuan, Defu Bu, and Maochun Wu. Outflow from Hot Accretion Flows. In C. M. Zhang, T. Belloni, M. Méndez, and S. N. Zhang, editors, *Feeding Compact Objects: Accretion on All Scales*, volume 290 of *IAU Symposium*, pages 86–89, February 2013.

[290] J. J. Bailey, I. B. Abdurakhmanov, A. S. Kadyrov, I. Bray, and A. M. Mukhamedzhanov. Proton-beam stopping in hydrogen. *Physical Review A*, 99(4):042701, April 2019.

[291] Kunihito Ioka, Tatsuya Matsumoto, Yuto Teraki, Kazumi Kashiyama, and Kohta Murase. GW 150914-like black holes as Galactic high-energy sources. *Mon. Not. Roy. Astron. Soc.*, 470(3):3332–3345, September 2017.

[292] Britton D. Smith et al. Grackle: a Chemistry and Cooling Library for Astrophysics. *Mon. Not. Roy. Astron. Soc.*, 466(2):2217–2234, 2017.

[293] Y. Pidopryhora, Felix J. Lockman, J. M. Dickey, and M. P. Rupen. High-resolution Images of Diffuse Neutral Clouds in the Milky Way. I. Observations, Imaging, and Basic Cloud Properties. *The Astrophysical Journal Supplement Series*, 219(2):16, August 2015.

[294] Jo Bovy. galpy: A python Library for Galactic Dynamics. *The Astrophysical Journal Supplement Series*, 216(2):29, February 2015.

[295] M. Hoeft, J. P. Mücket, and S. Gottlöber. Velocity Dispersion Profiles in Dark Matter Halos. *Astrophys. J.*, 602(1):162–169, February 2004.

[296] Felix J. Lockman. Discovery of a Population of H I Clouds in the Galactic Halo. *Astrophysical Journal Letters*, 580(1):L47–L50, November 2002.

[297] H. Alyson Ford, Felix J. Lockman, and N. M. McClure-Griffiths. Milky Way Disk-Halo Transition in H I: Properties of the Cloud Population. *Astrophys. J.*, 722(1):367–379, October 2010.

[298] Philipp Richter, Kenneth R. Sembach, Bart P. Wakker, Blair D. Savage, Todd M. Tripp, Edward M. Murphy, Peter M. W. Kalberla, and Edward B. Jenkins. The Diversity of High- and Intermediate-Velocity Clouds: Complex C versus IV Arch. *Astrophys. J.*, 559(1):318–325, September 2001.

[299] Yakov Faerman, Amiel Sternberg, and Christopher F. McKee. Ultra-compact High Velocity Clouds as Minihalos and Dwarf Galaxies. *Astrophys. J.*, 777(2):119, November 2013.

[300] Emma V. Ryan-Weber, Ayesha Begum, Tom Oosterloo, Sabyasachi Pal, Michael J. Irwin, Vasily Belokurov, N. Wyn Evans, and Daniel B. Zucker. The Local Group dwarf Leo T: HI on the brink of star formation. *Mon. Not. Roy. Astron. Soc.*, 384(2):535–540, February 2008.

[301] Evan N. Kirby, Joshua D. Simon, Marla Geha, Puragra Guhathakurta, and Anna Frebel. Uncovering Extremely Metal-Poor Stars in the Milky Way's Ultrafaint Dwarf Spheroidal Satellite Galaxies. *Astrophys. J. Lett.*, 685(1):L43, September 2008.

[302] G.W. Gibbons. Vacuum Polarization and the Spontaneous Loss of Charge by Black Holes. *Commun. Math. Phys.*, 44:245–264, 1975.

[303] W.T. Zaumen. Spontaneous Discharge of Kerr-Newman Black Holes. In *Marcel Grossmann Meeting on the Recent Progress of the Fundamentals of General Relativity*, pages 537–538, 1 1975.

[304] Jane H. MacGibbon and B. R. Webber. Quark- and gluon-jet emission from primordial black holes: The instantaneous spectra. *Phys. Rev. D*, 41:3052–3079, May 1990.

[305] Jane H. MacGibbon. Quark- and gluon-jet emission from primordial black holes. ii. the emission over the black-hole lifetime. *Phys. Rev. D*, 44:376–392, Jul 1991.

[306] Jane H. MacGibbon, Bernard J. Carr, and Don N. Page. Do Evaporating Black Holes Form Photospheres? *Phys. Rev. D*, 78:064043, 2008.

[307] J.H. MacGibbon and B.R. Webber. Quark and gluon jet emission from primordial black holes: The instantaneous spectra. *Phys. Rev. D*, 41:3052–3079, 1990.

[308] Alexandre Arbey and Jérémy Auffinger. BlackHawk: A public code for calculating the Hawking evaporation spectra of any black hole distribution. *Eur. Phys. J. C*, 79(8):693, 2019.

[309] J. M. Shull and M. E. van Steenberg. X-ray secondary heating and ionization in quasar emission-line clouds. *Astrophysical Journal*, 298:268–274, November 1985.

[310] Massimo Ricotti, Nickolay Y. Gnedin, and J.Michael Shull. The fate of the first galaxies. I. self-consistent cosmological simulations with radiative transfer. *Astrophys. J.*, 575:33, 2002.

[311] Steven Furlanetto and Samuel Johnson Stoever. Secondary ionization and heating by fast electrons. *Mon. Not. Roy. Astron. Soc.*, 404:1869, 2010.

[312] M.J. Berger, J.S. Coursey, M.A. Zucker, and J. Chang. Computer programs for calculating stopping-power and range tables for electrons, protons, and helium ions (version 1.2.3), 2017.

[313] Fiona H. Panther. Positron Transport and Annihilation in the Galactic Bulge. *Galaxies*, 6(2):39, 2018.

[314] Adam Coogan, Logan Morrison, and Stefano Profumo. Direct Detection of Hawking Radiation from Asteroid-Mass Primordial Black Holes. 10 2020.